# Studies on Degradation Behavior of Ni–based Cermet Anode for Solid Oxide Fuel Cells

**Yi-Hsuan Lee**

**Department of Energy and Hydrocarbon Chemistry**

**Graduate School of Engineering**

**Kyoto University**

**Kyoto, Japan**

**2013**

## Contents

# General Introduction

## Background of the work

### 1. Fundamental concept of solid oxide fuel cells

Various global problems such as global warming and acid rain etc. were caused by an increase in the usage of fossil fuel for energy production in human activity. It is important to use the fossil fuel more efficiently and cleanly. Fuel cells are electrochemical devices converting chemical energy into electrical energy directly, and thus attain high energy conversion efficiency than conventional internal-combustion engines. Therefore, there have been intensive interests in fuel cells.

Fuel cells are divided into five categories according to the type of electrolytes: polymer electrolyte membrane fuel cells (PEMFCs), alkaline fuel cells (AFCs), phosphoric acid fuel cell (PAFCs), molten carbonate fuel cells (MCFCs), and solid oxide fuel cells (SOFCs) [1, 2]. Among them, SOFCs are one of the most attractive power generation systems due to the high efficiency and excellent fuel flexibility at high temperatures. The characteristic of SOFCs is the high operating temperature of 600–1000 ºC. Thus, the electrical efficiency as high as 45–50 % can be attained without employing precious metals as the anode [3-8].

The primary components of a SOFC include ion conducting electrolyte, cathode, anode, and interconnect. For the conventional SOFC with oxide ion conducting electrolyte, oxygen is electrochemically reduced at the cathode to produce oxide ions and consume electrons. The generated oxide ions, after migrating across the electrolyte, will react with the hydrogen at the anode and release electrons as shown in Fig.1 [7, 8]. The electrochemical reactions can be written as follows:

| | | |
|---|---|---|
| Cathode | $1/2O_2 + 2e^- \rightarrow O^{2-}$ | (1) |
| Anode | $H_2 + O^{2-} \rightarrow H_2O + 2e^-$ | (2) |
| Overall reaction | $1/2O_2 + H_2 \rightarrow H_2O$ | (3) |

According to reaction (2), the anode is requested not only to transport electrons and oxide ions, but also to be porous to allow $H_2$ to diffuse towards the electrolyte. The most common material of anode is the metallic nickel/yttria–stabilized zirconia (YSZ) cermet. YSZ prevents the sintering of the Ni particles and provides a close thermal expansion coefficient to YSZ–electrolyte. Ni and YSZ serve as the electron and oxide ion conductors, respectively. It is well known that the electrochemical reaction only proceeds at the triple-phase boundary (TPB), where oxide ion conductor, electron conductor, and gas phase meet together as shown in Fig. 2 [9, 10]. By mixing Ni and YSZ, the TPB length can be extended significantly, leading to the improvement of cell performance. Moreover, it is suggested that most of the electrochemical reaction occur near the region of anode/electrolyte interface [11, 12]. Additionally, other Ni-based cermet anodes such as Ni-scandia-stabilized zirconia (ScSZ) [13], and Ni-samaria-doped ceria (SDC) [14], *etc*., have also been employed for SOFCs.

## 2. Power generation with $CH_4$ as fuel

Although $H_2$ can provide high mass energy density and only water in emission, problems of hydrogen generation and storage should be overcome. Therefore, external reformer is necessary for the low temperature fuel cells to produced $H_2$ from hydrocarbon [15]. Because of the high operation temperature of SOFCs, hydrocarbon fuels such as methane can be directly introduced without external reforming processes. [16-18].

With supply of dry $CH_4$ as a fuel to cell at 800 ºC, Onuma *et al*. analyzed the composition of anode outlet gas during discharge [19, 20]. It was suggested that reaction (2) was the main electrochemical process during power generation with dry $CH_4$. Based on this fact, the mechanism was interpreted as follows. Methane cannot react with $O^{2-}$ directly. Instead, it decomposes into carbon and $H_2$ (shown as reaction (4)), and then $H_2$ is oxidized electrochemically under current loading:

$$CH_4 \rightarrow C + 2H_2 \quad (4)$$

## 3. Degradation of anode performance due to carbon deposition

Carbon formed by cracking reaction (4) will be deposited on the Ni-cermet anode, leading to the deterioration of anode performance [21-26]. Koh *et al*. reported that the deposited carbon encapsulated the Ni particle, and thus increased the polarization resistance of Ni–YSZ anode after exposure to flowing dry $CH_4$ for 3 h at 750 ºC [27]. Moreover, Lin *et al.* observed that carbon deposition during the long-term discharge operation of cell induced the Ni–YSZ anode failure because of the micro-cracking between YSZ and Ni [28]. On the other hand, the anode performance and durability are related with crystallinity of deposited carbon. Some researchers have studied the crystallinity of deposited carbon with Raman spectroscopy to elucidate its effect on the anode performance [29-32]. In the Raman spectra, two peaks are usually observed at 1585 $cm^{-1}$ and 1350 $cm^{-1}$, which correspond to the crystalline graphite and amorphous carbon, respectively. The intensity-ratios of the two peaks, $I_{1585}/I_{1350}$ can be used to evaluate the crystallinity of deposited carbon [32].

## 4. Carbon deposition region in C–H–O diagram

The C–H–O diagram in the temperature range of 400–1200 ºC at 1 atm is shown in Fig. 3 [33, 34]. According to the thermodynamic calculation above 900 ºC, carbon deposits in the C-rich region from the $H_2$–CO line. The carbon deposition region expands as the temperature decreases as far as the equilibrium is achieved. It is noted that $CH_4$ is more stable at temperatures lower than 700 ºC, inducing bending of the boundary line around the H corner. The carbon deposition resulting from reaction (4) could be suppressed by methane reforming reaction as described in reactions (5) and (6) [35, 36]:

$$CH_4 + H_2O \rightarrow CO + 3H_2 \quad (5)$$

$$CH_4 + CO_2 \rightarrow 2CO + 2H_2 \quad (6)$$

For example, $H_2O/CH_4$ = 1 and $CO_2/CH_4$ = 1 are located on carbon deposition boundary at 900 ºC–1200 ºC as indicated in Fig. 3. Therefore, in the steam and carbon dioxide reforming process of methane, the gas composition can be controlled along the blue and green lines, respectively. Theoretically, the generation of carbon will be avoided. However, the supply of a large amount of $H_2O$ or $CO_2$ significantly increases the oxygen partial pressure ($P(O_2)$) in the anode, resulting in the reduction of open circuit voltage (OCV) and the energy conversion efficiency. In practical operation, the Steam/Carbon ratio over 3 is needed to suppress carbon deposition. In addition, the size of Ni particles grows during long-term operation on methane steam reforming [37, 38]. Ni particles agglomerate significantly with increasing temperature and humidity, resulting in performance degradation. Therefore, it is desired to maintain energy conversion efficiency without performance deterioration by feeding a fuel with relative low ratio of $H_2O/CH_4$ or $CO_2/CH_4$.

## 5. Solutions to carbon deposition

Many studies have been devoted to deal with carbon deposition on the Ni-cermet anode. Ni–ScSZ has superior resistance of carbon deposition to Ni–YSZ [25]. Yamaji *et al.* reported that the cell performance maintained stable at 550 ºC without severe carbon deposition over a week operation by using Ni–ScSZ [39]. In addition, ceria can promote hydrocarbon gas conversion over Ni catalyst, and thus inhibit carbon deposition [40]. Iida et al. have demonstrated that the cell performance for Ni–SDC anode could be maintained stably during the galvanostatic operation with 0.3 A $cm^{-2}$ by feeding the humidified propane with S/C of 0.8 [21]. It was also reported that adding alkaline earth oxides such as CaO or SrO in the Ni–YSZ anode was effective to suppress carbon deposition [41]. Kan *et al.* claimed that the cell with Sn-doped Ni–YSZ cermet anode exhibited more stable performance than that with Ni–YSZ cermet anode [42]. Although carbon deposition can be inhibited, it is difficult to avoid carbon deposition completely. Therefore, carbon removal from the anode is taken into account for SOFCs.

In the field of catalytic processing of hydrocarbon gases, the deposited carbon can be removed from the surface of Ni–based catalyst by different gaseous species such as $H_2O$, $CO_2$, *etc.*, to recover the catalytic performance, which is called as the regeneration treatment [43-45]. Nikooyeh *et al*. deposited carbon on the Ni–YSZ pellet by supplying 32% $CH_4$–3% $H_2O$–65% He at 800 ºC for 3 h. Subsequently, the deposited carbon was totally removed by temperature programmed hydrogenation (TPH) with 80% $H_2$–20% He [46]. However, the surface morphology after carbon disappearance contained cracks on the Ni–YSZ pellet. On the other hand, the deposited carbon on the anode can also be removed by current passage [28].

**Outline of the work**

Ni–YSZ is the most common anode material for SOFC systems. However, the electrochemical behavior of Ni–YSZ anode with the supply of methane has not been clarified sufficiently. This thesis consists of five chapters.

The thickness of anode is one of the key factors to affect the internal reforming of methane. In chapter 1, Ni–YSZ and Ni–SDC anodes with different thicknesses were examined during long-term operation of SOFCs with humidified methane at high temperature. The electrochemical behavior of anodes was investigated systematically. Moreover, the crystallinity of deposited carbon after power generation was analyzed by Raman spectroscopy.

In chapter 2, based on the fact that carbon dioxide reforming of methane (reaction 8) was effective to suppress carbon deposition, the performance and durability for Ni–YSZ anode were compared between internal steam reforming and $CO_2$ reforming of methane in the carbon deposition condition. The same experiment was also conducted with Ni–ScSZ anode. In addition, the relation between the performance and the crystallinity/morphology of deposited carbon was investigated.

As shown in reactions (5) and (6), CO is generated via the internal reforming of methane. In chapter 3, the performance degradation by carbon deposition was evaluated in comparison with the CO disproportion (reaction (7)) at low temperature and methane cracking (reaction (4)) at high temperature. Electrolyte- and anode-supported cells were used to evaluate the effect of anode thickness on carbon deposition at low and high temperature.

$$2CO \rightarrow C + CO_2 \quad (7)$$

Carbon removal from the anode is important to recover the anode performance. In

chapter 4, we focused on the change in the performance of Ni–YSZ anode after carbon removal by gas-feed and current passage.

Carbon deposition can be suppressed by supply of a large amount of $H_2O$ with $CH_4$. However, under long-term operation, the sintering of Ni particles appeared to be promoted strongly with increasing temperature and humidity. Therefore, in chapter 5, the relationship between the microstructural change in Ni–YSZ anode cermet and performance deterioration under different temperature and humidification conditions was studied.

**References**


[1] J. Larminie and A. Dicks, Fuel Cell Systems Explained (2nd Edition), Wiley, 2003.

[2] A. B. Stambouli and E. Traversa, *Renewable and Sustainable Energy Reviews*, **6** 433 (2002).

[3] S. P. S. Badwal, *Solid State Ionics*, **143**, 39 (2001).

[4] R.J. Gorte and J. M. Vohs, *J. Catal.*, **216**, 477 (2003).

[5] S. P. Jiang and S. H. Chan, *J. Mater. Sci.*, **39**, 4405 (2004).

[6] T. Horita, K. Yamaji, T.Kato, N. Sasaki, and H. Yokokawa, *J. Power sources*, **131**, 299 (2004).

[7] S. M. Haile, *Acta Materialia*, **51**, 5981 (2003)

[8] T. Horita, H. Kishimoto, K. Yamaji, Y. Xiong, N. Sasaki, M. E. Brito and H. Yokokawa, *Solid State Ionics*, **177**, 1941 (2006).

[9] S. Mclntosh and R. Gorte, *Chem. Rev.*, **104**, 4845 (2004).

[10] J. Mizusaki, H. Tagawa, T. Saito, T. Yamamura, *Solid State Ionics*, **70-71**, 52 (1994).

[11] M. Brown, S. Primdahi, and M. Mogenson, *J. Electrochem. Soc.*, **147** (2) (2000).

[12] X. Wang, N. Nakagawa, and K. Kato, *J. Electrochem. Soc.*, **148**, A565 (2001).

[13] T. Matsui, T. Iida, R. Kikuchi, M. Kawano, T. Inagaki, and K. Eguchi, *J. Electrochem. Soc.*, **155**, B1136 (2008).

[14] T. Misono, K. Murata, T. Fukui, *J.* Chaichanawong, K. Sato, H. Abe, and M. Naito, *J. Power Sources*, **157**, 754 (2004).

[15] B. C. H. Steele and A. Heinzel, *Nature*, **414**, 345 (2001).

[16] Z. Zhan and S. A. Barnett, *Science*, **308**, 844 (2005).

[17] E. P. Murray, T. Tsai, and S. A. Barnett, *Nature*, **400**, 649 (1999).

[18] S. Park, R.J. Gorte, J.M. Vohs, *Nature*, **404**, 265 (2000).

[19] S. Onuma, A. Kaimai, K. Kawamura, Y. Nigara, T. Kawada, J. Mizusaki, H. Inaba, and H. Tagawa, *J. Electrochem. Soc.*, **145**, 3117 (1998).

[20] S. Onuma, A. Kaimai, K. Kawamura, Y. Nigara, T. Kawada, J. Mizusaki, H. Inaba, H. Tagawa, *J. Electrochem. Soc.*, **145**, 920 (1998).

[21] T. Iida, M. Kawano, T. Matsui, R. Kikuchi, and K. Eguchi, *J. Electrochem. Soc.*, **154**, B234 (2007).

[22] A. Weber, B. Sauer, A. C. Mu¨ller, D. Herbstritt, and E. Ivers-Tiffe´e, *Solid State Ionics*, **152-153**, 543 (2002).

[23] T. Kim, G. Liu, M. Boaro, S.-I. Lee, J.M. Vohs, R.J. Gorte, O. H. Al-Madhi, B. O. Dabbousi, *J. Power Sources*, **155**, 231 (2006).

[24] C. M Finnerty, N. J. Coe, R. H. Cunningham, and R. M. Ormerod, *Catal. Today*, **46**, 137 (1998).

[25] H. Sumi, K. Ukai, Y. Mizutani, H. Mori, C.-J. Wen, H. Takahashi, and O. Yamamoto, *Solid State Ionics*, **174**, 151 (2004).

[26] T. Takeguchi, R. Kikuchi, T. Yano, K. Eguchi, K. Murata, *Catal. Today*, **84**, 217 (2003).

[27] J. –H. Koh, Y. –S. Yoo, J. –W. Park, H. C. Lim, *Solid State Ionics*, **149**, 157 (2002).

[28] Y. Lin, Z. Zhan, J. Liu, and S. A. Barnett, *Solid State Ionics*, **176**, 1827 (2005).

[29] M. B. Pomfret, J. Marda, G. S. Jackson, B. W. Eichhorn, A. M. Dean, and R. A. Walker, *J. Phys. Chem. C.*, **112**, 5232 (2008).

[30] K. Yamaji, H. Kishimoto, Y. Xiong, T. Horita, N. Sasaki, M. E. Brito, and H. Yokokawa, *Solid State Ionics*, **179**, 1596 (2008).

[31] K. Yashiro, M. Takase, K. Sato, T. Kawada, and J. Mizusaki, *ECS Trans.*, **16**, 213 (2008).

[32] H. Sumi, P. Puenginda, H. Muroyama, T. Matsui, and K. Eguchi, *J. Power Sources*, **196**, 6048 (2011).

[33] T. Takeguchi, Y. Kani, T. Yano, R. Kikuchi, K. Eguchi, K. Tsujimoto, Y. Uchida, A. Ueno, K. Omoshiki and M. Aizawa, *J. Power Sources*, **112**, 588 (2002).

[34] K. Eguchi, H. Kojo, T. Takeguchi, R. Kikuchi, and K. Sasaki, *Solid State Ionics*, **152-153**, 411 (2002).

[35] Y. Shiratori, T. Oshima, and K. Sasaki, *Int. J. Hydrogen Energy*, **33**, 6316 (2008).

[36] R. Peters, E. Riensche, and P. Cremer, *J. Power Sources*, **86**, 432 (2000).

[37] J. Sehested, *Catal. Today.*, **111**, 103 (2006).

[38] D. L. King, J. J. Strohm, X. Wang, H.-S. Roh, C. Wang, Y.-H. Chin, Y. Wang, Y. Lin, R. Rozmiarek, and P. Singh, *J. Catalysis*, **258**, 356 (2008).

[39] K. Yamaji, H. Kishimoto, Y. Xiong, T. Horita, N. Sakai, M. E. Brito, H. Yokokawa, *J. Power Sources*, **159**, 885 (2006).

[40] K. Otsuka, Y. Wang, E. Sunada, and I. Yamanaka, *J. Catalysis*, **175**, 152 (1998).

[41] T. Takeguchi, Y. Kani, T. Yano, R. Kikuchi, K. Eguchi, K. Tsujimoto, Y. Uchida, A. Ueno, K. Omoshiki and M. Aizawa, *J. Power Sources*, **112**, 588 (2002).

[42] H. Kan and H. Lee, *Appl. Catal. B Env.*, **97**, 108 (2010).

[43] J. L. Figueiredo and D. L. Trimm, *J. Catal.*, **40**, 154 (1975).

[44] R. Aiello, J. E. Fiscus, H. Loye, and M. D. Amiridis, *Appl. Catal. A General*, **192**, 227 (2000).

[45] S. Takenaka, Y. Tomikubo, E. Kato, K. Otuka, *Fuel*, **83**, 47 (2004) .

[46] K. Nikooyeh, R. Clemmer, V. Alzate-Restrepo, and J. M. Hill, *Appl. Catal. A General*, **347**, 106 (2008).

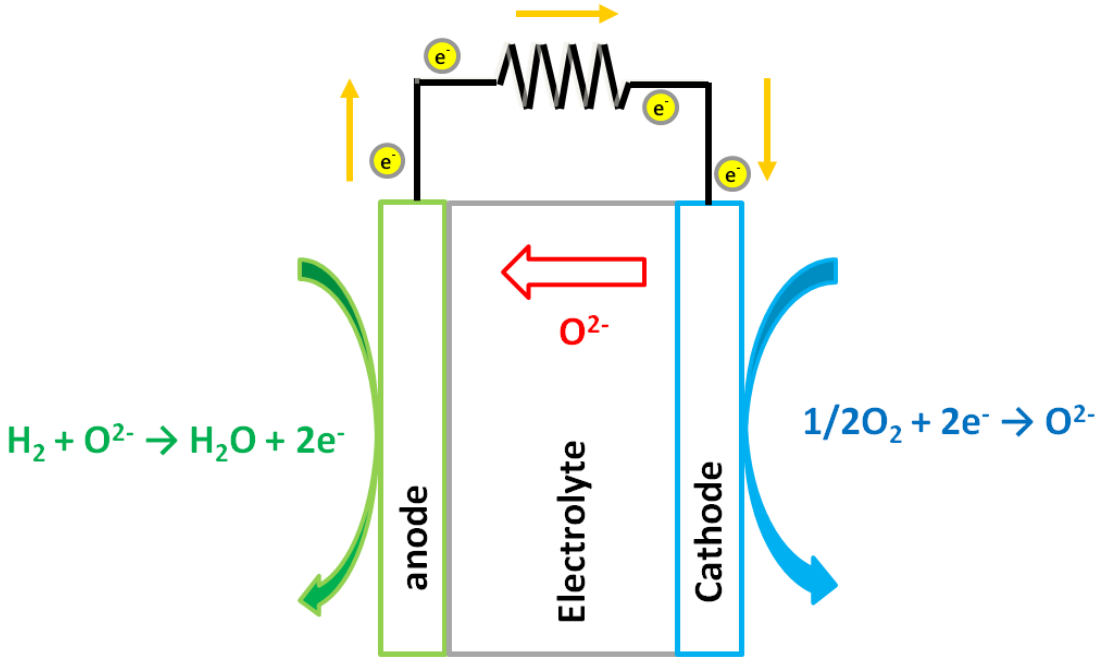


**Figure 1 Schematic of basic concept of a solid oxide fuel cell.**

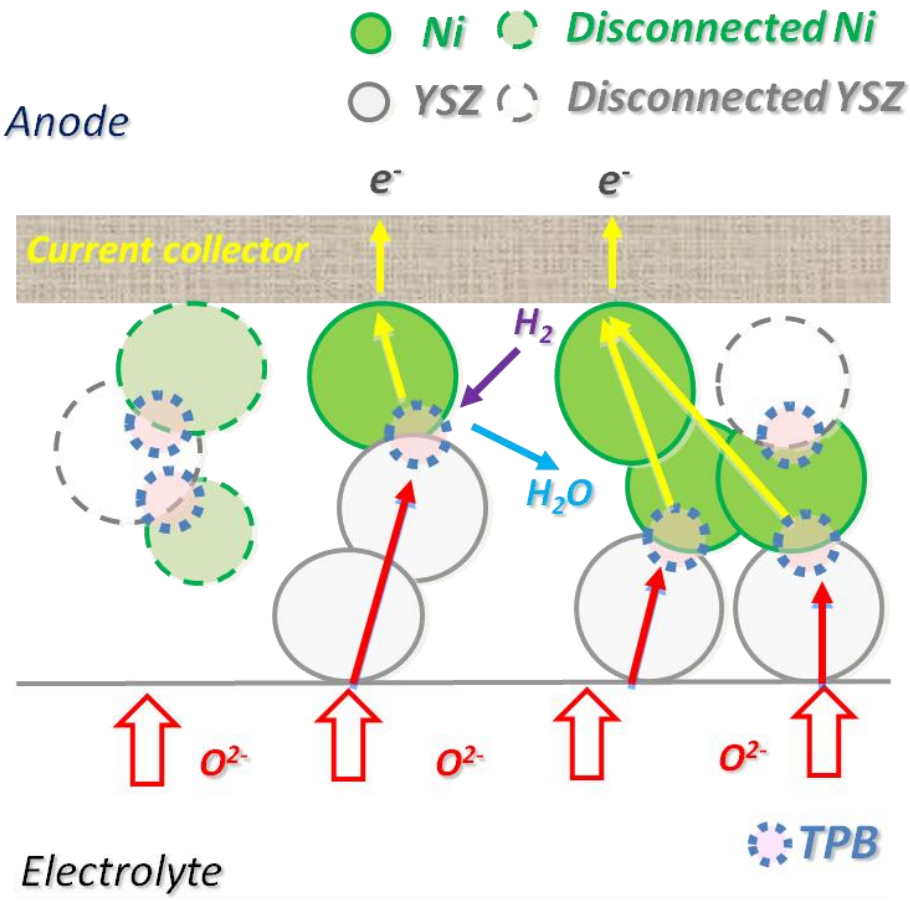


**Figure 2 Schematic of Ni–YSZ anode three-phase boundary.**

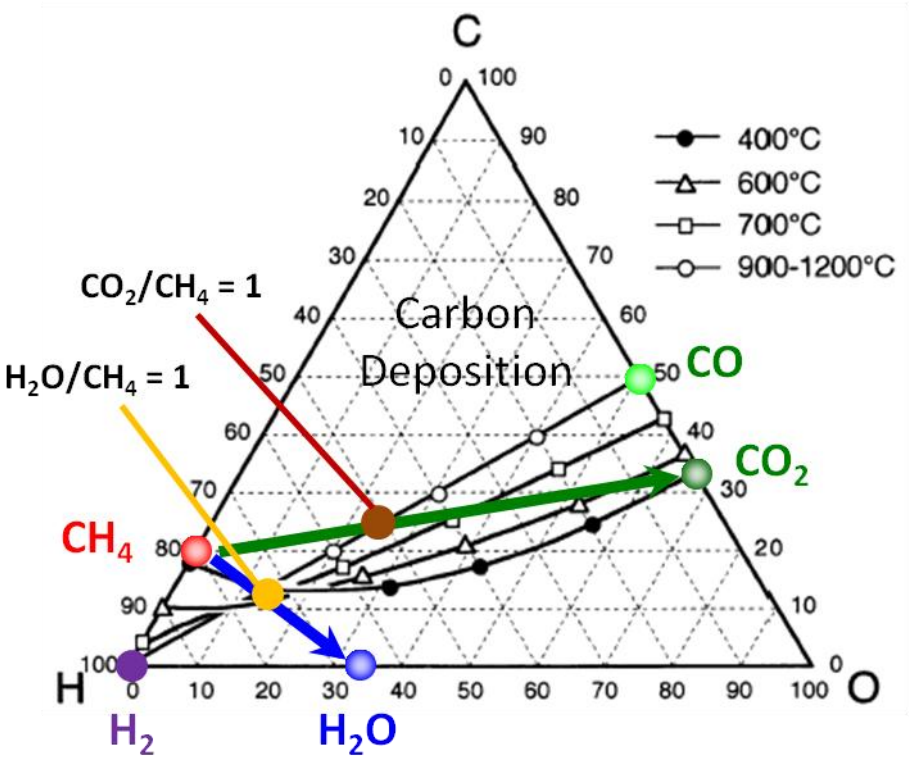


**Figure 3 The boundary of carbon deposition region in the C–H–O phase diagram at 1 atm. Carbon deposition is expected in the carbon-rich composition beyond the boundary at respective temperatures [34].**

# Chapter 1

# Influence of Ni–oxide Anode Thickness on Performance Stability in Internal Steam Reforming of Methane for Solid Oxide Fuel Cells

## 1.1 Introduction

Solid oxide fuel cells (SOFCs) are one of the promising power generation devices due to their high energy conversion efficiency and low emissions. High fuel flexibility of SOFCs has also attracted much attention for a simplified system; hydrocarbons such as methane and propane are directly introduced as fuels into SOFCs without external reforming processes. In this system, the conventional Ni–yttria–stabilized zirconia (Ni–YSZ) cermet serves as a reforming catalyst of hydrocarbons as well as a fuel electrode. In the internal reforming operation, the performance deterioration induced by carbon deposition over the Ni catalyst is well-known as a serious problem [1-5]. Although the supply of a large amount of steam with hydrocarbon suppresses the carbon deposition, the concomitant increase in the oxygen partial pressure at the anode results in the reduction of open circuit voltage (OCV) and the energy conversion efficiency. High content of steam in a fuel also gives rise to the change in the surface of Ni particles and the decrease in triple-phase boundary (TPB) length, leading to the performance deterioration [6]. Thus, it is desired to accomplish stable power generation by feeding a fuel with low steam to carbon (S/C) ratio; the carbon deposition boundary is theoretically located in the S/C ratio of 1.0 in the temperature range of 900–1200 ºC [7].

Many studies have been devoted to achieve this target upon the internal reforming operation. Abudula *et al.* studied the effect of anode thickness on cell performance with

Ni–YSZ cermets at 1000 ºC by supplying dry methane [8]. The performance was improved with an increase in the anode thickness up to 70 μm. Eguchi *et al.* also reported that the internal reforming reaction of methane was insufficient for the Ni–YSZ anode with *ca.* 100 μm-thick [9]. Thus, the cell configuration such as an anode thickness is one of the key factors to determine the performance. The operating condition also affects the stability. Lin *et al.* have demonstrated the stable power generation at 800 ºC with passing a high current of 1.8 A $cm^{-2}$ even in 3% $H_2O$–97% $CH_4$ [10]. They concluded that the steam generated via the electrochemical reaction removed deposited carbon effectively, resulting in the suppression of carbon deposition. The application of other constituent materials is an alternative approach to avoid the carbon deposition. It has been reported that ceria serves as a promoter with Ni catalyst for hydrocarbon gas conversion [11-12]. Furthermore, carbon deposition scarcely occurred over the ceria-supported catalysts. Thus, it can be expected that Ni–ceria-based cermet is the promising anode for direct feeding of hydrocarbon fuels. Actually, some researchers have focused on the ceria materials for the internal reforming operation of SOFCs. Putna *et al.* studied the effect of samaria-doped ceria (SDC) on cell performance by supplying 20% $CH_4$–80% $N_2$ at 800 ºC. An increase of SDC amount in the anode significantly improved the cell performance [13]. Lee *et al.* showed that no obvious performance degradation with the Ni–gadolinia-doped ceria anode in liquid hydrocarbon as fuel at 550 ºC for 500 h [14]. In previous study, the influence of oxide species in the cermet on the carbon deposition behavior has been investigated at 1000 ºC under open-circuit and discharged states [1]. The cell with Ni–SDC anode was stably operated initially in a short period, less than 6 h, during the galvanostatic operation with 0.3 A $cm^{-2}$ by feeding the humidified propane with S/C of 0.8, whereas the terminal

voltage for Ni–YSZ anode was degraded by *ca.* 30%. Note that, however, the amount of deposited carbon over Ni–SDC cermet was larger than that over Ni–YSZ under the open-circuit state. Such a peculiar behavior observed in Ni–SDC is related to the partial pressure of oxygen ($P(O_2)$) in the exposed atmosphere. The thermodynamic calculation has proved that the oxygen potential for carbon deposition is $P(O_2) = 10^{-19}$–$10^{-20}$ atm at 1000 ºC. This $P(O_2)$ range is close to that of phase transition boundary of ceria [15-16]. The fluorite $CeO_2$ phase is converted into the $Ce_3O_5$ phase with the rare-earth type-C structure at $P(O_2) = 10^{-18}$–$10^{-19}$ atm at 1000 ºC. Therefore, this $P(O_2)$-dependent phase transition in ceria will have a significant impact on the difference in the carbon deposition behavior under open-circuit and discharge conditions. As described above, many factors have to be considered to design the anodes with high tolerance to carbon deposition for use in internal reforming operation.

It is commonly recognized that the degradation over anodes induced by carbon deposition is a time-dependent phenomenon; *i.e.*, the microstructural change of nickel particles and blocking of open pore. However, there is no report dealing with the degradation phenomena from the aspect of time scale. Most of reports in this field have evaluated only the transient performance and the presence or absence of carbon deposition in a short time. In chapter 1, the author focuses on the influence of the materials and cell configuration, especially the anode thickness, on the performance stability during the long-term operation with hydrocarbon fuels. Two cermet anodes of Ni–YSZ and Ni–SDC with different thickness were applied.

## 1.2 Experimental

Two cermets of Ni–YSZ and Ni–SDC were applied as fuel electrodes. The commercially available NiO–YSZ powder (AGC seimi chemical company) was used for the slurry preparation. Samaria-doped ceria with a composition of $Ce_{0.8}Sm_{0.9}O_{1.9}$ (SDC) was prepared by the oxalates precipitation procedure [1]. The volumetric ratios of Ni to YSZ and Ni to SDC in the cermets were fixed to be 47 to 53 and 50 to 50, respectively. A perovskite type oxide of $(La_{0.8}Sr_{0.2})_{0.97}MnO_3$ (LSM) was applied as an air electrode.

The cells were prepared by applying each paste of the electrode powder onto a YSZ disk (Tosoh, thickness: 500 μm, diameter: 24 mm). The powder of electrode materials was mixed with polyethylene glycol (Wako Pure Chemical Industries) to form slurry. The thickness of anode was controlled to be *ca*. 10, 20, and 30 μm throughout this study. The NiO–YSZ slurry was screen-printed on one face of the YSZ disk at the central part with 6 mm diameter, followed by the calcination at 1400 ºC for 5 h. In the case of NiO–SDC, the slurry was screen-printed in the same manner as NiO–YSZ, and then the disk was fired at 1280 ºC for 3 h to avoid the chemical reaction between YSZ and SDC [17-18]. The air electrode slurry was coated with the same way on the other face of the disk, and subsequently heated at 1150 ºC for 5 h. The fabricated cell was sandwiched by alumina tubes with a Pyrex glass seal, as shown in Fig. 1.1.

Power generation characteristics of fuel cells were evaluated at 1000 ºC. After heating the sample up to the desired temperature, diluted and pure hydrogen were supplied to the fuel electrode for the reduction of NiO. A gaseous mixture of 3% $H_2O$–97% $H_2$ or 30% $CH_4$–3% $H_2O$–67% $N_2$ (S/C = 0.1) was fed to the anode with a flow rate of 100 ml $min^{-1}$. Note that the carbon deposition occurs spontaneously in

$CH_4$–$H_2O$–$N_2$ with an S/C ratio of 0.1 at 1000 ºC. Oxygen was supplied to the cathode as an oxidant with a flow rate of 100 ml $min^{-1}$. Electrochemical measurements were conducted by the CellTest system (Solartron Analytical, potentiostat/galvanostat 1470E and frequency response analyzer 1455A). The series of experiments in this study was performed several times and consistent results were obtained.

After power generation, the cross-section of anodes were analyzed by a scanning electron microscope (SEM, NVision 40, Carl Zeiss) equipped with an energy-dispersive X-ray spectrometer (EDX, Oxford). The state of deposited carbon was studied by Raman spectroscopy (Horiba Jobin Yvon, LabRAM HR–800). Raman spectra were recorded by irradiating $Ar^+$ laser (514.5 nm) focused to a 1-μm-size spot.

### 1.3 Results and discussion

The performance of the cells employing Ni–YSZ anodes of three different thicknesses was examined at 1000 ºC by supplying 3% $H_2O$–97% $H_2$ and $CH_4$–$H_2O$–$N_2$ mixture (S/C = 0.1) as fuels. The current–voltage (*I*–*V*) curves are shown in Fig. 1.2. In the case of humidified hydrogen fuel, OCVs of all cells were identical to the theoretical values derived from the Nernst equation, and *I*–*V* characteristics were independent of the anode thickness. In contrast, in a humidified methane (S/C = 0.1) fuel, OCV and cell performance depended on the anode thickness. The cell with a 30-μm thick anode showed the highest OCV of 1.22 V, and OCV decreased with a reduction in the anode thickness. This suggested that the reforming reaction of methane were strongly related with an anode thickness. A lack of exposed nickel surface area would be attributable to the low OCV for 10 μm sample in the Ni–YSZ anode. Although such a difference was prominent at low current density, the performances of three different cells converged

into the same level at high current density of *ca.* 0.6 A $cm^{-2}$. This is because the steam generated by the discharge operation promoted the reforming reaction even in thin anode layer.

The same experiments were conducted for the cells employing Ni–SDC anodes, and results were depicted in Fig. 1.3. The cells of different anode thickness showed a comparable performance and theoretical OCV in humidified hydrogen, though the current density achieved at 0.5 V was about half of that obtained for Ni–YSZ anode. This low performance is mainly due to the low firing temperature of Ni–SDC on the electrolyte, which is related to the weak adhesion between each oxide component. Note that in a humidified methane fuel, a distinct difference was observed between Ni–SDC and Ni–YSZ: The cell performance and OCV were independent of the thickness of Ni–SDC anode. $P(O_2)$ in the anode compartment can be estimated to be ca. $10^{-22}$ atm from the obtained OCV of 1.35 V, which is within the carbon deposition region in the C–H–O ternary diagram [9]. Thus, the thermal cracking of methane occurs spontaneously. Considering that Ni–SDC provided the higher OCV as compared with Ni–YSZ, SDC should promote the cracking reaction. This result is consistent with that reported by Iida *et al.* [1]; carbon tends to deposit over Ni–SDC anodes than over Ni–YSZ anode at the open-circuit state.

Time course of terminal voltage measured at a constant current density of 0.2 A $cm^{-2}$ with a supply of $CH_4$–$H_2O$–$N_2$ mixture (S/C = 0.1) for Ni–YSZ is shown in Fig. 1.4 (a). Corresponding changes in ohmic resistance between anode and reference electrode and the anode overpotential during discharge are also depicted in Figs. 1.4 (b) and (c), respectively. The initial performance was enhanced with increasing anode thickness. The cells with 20- and 30-μm thick anodes exhibited stable performance for

20 h. In response to this behavior, no changes in the ohmic resistance and the overpotential were confirmed. Moreover, in the case of cell with 30-μm thick anode, the terminal voltage was only slightly reduced for 106 h due to an increase in overpotential. On the other hand, the gradual decrease and subsequent oscillation in the terminal voltage were observed for 10-μm thick anode. Since the test condition in the present study was set within the carbon deposition region expected from the thermodynamic equilibrium, the performance deterioration observed in the 10-μm thick anode will be caused by the carbon deposition. The ohmic resistance of the 10-μm thick anode continuously increased with an elapse of time, while the anode overpotential kept stable within *ca.* 10 h. The carbon deposition generally proceeds from the surface of the anode to the electrode/electrolyte interface. It has been assumed that the coke buildup should induce the volume expansion of Ni particles and micro-cracking between YSZ and Ni, presumably leading to an interruption of anode current collection pathways [10]. Thus, the deposited carbon mainly damaged the electric conduction path in the upper layer of anode at the initial stage of degradation. With an elapse of time of 10-16 h, the slight oscillation in anodic overpotential was observed. Then, the overpotential steeply increased and oscillated with amplitude of *ca.* 0.6 V. Thus, it can be expected that the accumulated carbon disturbed the gas diffusion in the anode. As a result, the variation in hydrogen concentration at the triple-phase boundary (TPB) would give rise to this oscillatory behavior of the anode overpotential. Similar degradation for the thin anode layer could be observed reproducibly: the performance of cell with 7-μm thick anode was suddenly deteriorated in 5 h. The same series of measurements were conducted for the cells with Ni–SDC anodes, and results are summarized in Fig. 1.5. The cell performance was improved obviously during discharge at 0.2 A $cm^{-2}$ for 20 h regardless

of anode thickness. Concomitant reductions in ohmic resistance and overpotential were observed. These improvements upon discharge are related to the expansion of electrochemical active area as well as an increase in electronic conductivity of SDC, which is induced by partial reduction of $Ce^{4+}$ to $Ce^{3+}$ under reducing atmospheres [19-22]. In addition, catalytic $CH_4$ decomposition and reactions of reformed gases were examined on stripe-shaped Ni on the YSZ and yttria doped ceria (YDC) with secondary ion mass spectrometry (SIMS) by Horita *et al.* [23]. According to results of YDC substrate, it has been indicated that water vapor adsorbs on the Ni surface and dissociates into hydrogen (H). The resultant hydrogen (H) transfers to the Ni/YDC interface. Subsequently the charge transfer between H and $Ce^{4+}$ occurs, leading to the formation of proton in YDC. The protons can react with $O^{2-}$ to form $H_2O$, which evaporates from the surface of YDC. This series of reaction process may enhance the concentrations of water on the Ni surface. The similar phenomenon can be considered to occur in the Ni–SDC anode. Thus, the methane reforming reaction may promote in the Ni–SDC anode to improve cell performance.

Microstructural observation and Raman spectroscopy were conducted for the anodes operated in Figs. 1.4 and 1.5 to correlate the electrochemical behavior and the state of deposited carbon in the anode layer. The typical backscattered electron (BSE) images of the whole Ni–YSZ and Ni–SDC anodes are shown in Fig. 1.6. The light gray parts correspond to the Ni, YSZ, or SDC particles, whereas the dark gray parts were assigned to carbon by EDX analysis. For the 10 μm-thick Ni–YSZ anode, a large amount of carbon obstructed the pores in the whole anode layer. In contrast, carbon was observed only in the vicinity of surface for the 30-μm thick Ni–YSZ. As to the thick electrode, the author expected that the top surface could “buffer” the electrochemical

reaction sites at the interface from carbon deposition. Furthermore, because most of Ni particles remained uncovered, the methane reforming reaction and the removal of carbon by the generated $H_2O$ and $CO_2$ would readily proceed. In addition, after power generation for 106 h, carbon was observed obviously in the vicinity of surface and deposited scarcely near the electrolyte/anode interface. In the case of 30-μm thick Ni–SDC anode, formation of carbon was confirmed only in the vicinity of surface. Note that in the 10-μm thick anode, a small amount of carbon was observed. This high resistivity to the carbon deposition for Ni–SDC will result from the expansion of electrochemical active area as well as an increment in number of reaction sites. The former is related to the inherent chemical properties of ceria such as high solubility of proton, surface catalytic activity, and surface oxygen exchange etc., and the latter is ascribable to the partial reduction of ceria as mentioned above, which provides the additional electronic conduction path [22].

Figure 1.7 shows Raman spectra measured along the anode thickness direction, from the anode/electrolyte interface to the surface. The band at 1585 $cm^{-1}$ arises from the highly ordered graphite, which is generally labeled as “G”. The band at 1350 $cm^{-1}$, labeled as “D”, is attributed to disordered graphite carbon [24-26]. The spectra of 10-μm thick Ni–YSZ exhibited two broad peaks with low resolution, ascribable to G- and D-bands, regardless of position in the anode layer. Such a characteristic spectrum indicates the formation of amorphous carbon [27]. Note that this type of carbonaceous species has relatively low electric conductivity [27-29]; the electric conductivity of the graphite at room temperature is *ca.* 100-fold higher than that of amorphous carbon [30]. Therefore, the formation of low conductive carbon resulted in an increase in ohmic resistance between anode and reference electrode during galvanostatic operation as

observed in Fig. 1.4(b). On the other hand, considering the analogous spectra observed in the vicinity of surface for 30-μm thick anode, the low conductive carbon was formed only at the surface. Moreover, the deposited carbon was scarcely detected at the interface with the electrolyte as was observed in the BSE image (see Fig. 1.6(b)). Thus, the stable power generation was achieved without any changes in electrochemical parameters (see Fig. 1.4). The results for the 20 μm sample were analogous to those for the 30 μm sample from the microstructural observation and Raman analysis. In the case of Ni–SDC, spectrum shapes of deposited carbon were different from those in Ni–YSZ. This means that the chemical state of deposited carbon depends on the oxide component in the cermet. Sumi *et al*. also reported that the different characteristics of the carbon were observed in the Ni–YSZ and Ni–ScSZ anode by Raman spectroscopy [2]. Since the peaks of D- and G-bands were separated clearly, the deposited carbon in Ni–SDC leads to higher electric conductivity as compared with that in Ni–YSZ. This will contribute to reductions in ohmic resistance and overpotential, as well as the appearance of electronic conduction in SDC as observed in Fig. 1.5.

It is striking that in this study, the amorphous carbon with low conductivity was formed over Ni–YSZ anode. Such a characteristic carbon has not been observed over Ni–YSZ during discharge at 0.3 A $cm^{-2}$ for 20 h with feeding a methane fuel with S/C of 0.5 at 1000 ºC; Raman spectra were analogous to those for Ni–SDC. This indicates that the discharge conditions strongly affect the deposited amount, crystallinity and electric conductivity of carbon even over same electrode material. Because the negative effect induced by such carbonaceous species will be prominent upon the long-term operation, the operating conditions and constituent materials have to be considered carefully to avoid the carbon deposition.

## 1.4 Conclusions

The influence of the anode material thicknesses on the performance stability under a humidified methane (S/C = 0.1) at 1000 ºC was studied. The cell with Ni–SDC anode showed gradual improvement in performance during discharge regardless of anode thickness. The Ni–SDC anode will suppress the carbon deposition effectively and the performance was improved obviously during discharge. These improvements upon discharge were related to the expansion of electrochemical active area as well as an increase in electronic conductivity of SDC. The stable performance appeared in 30 μm-thick Ni–YSZ anodes because the top surface of Ni–YSZ anode served as the buffer layer to suppress the damage in reaction sites near the anode/electrolyte interface and support the effective removal of deposited carbon by the steam electrochemically-generated. However, the deterioration in performance was observed with 10 μm-thick Ni–YSZ anode within 18 h. For this anode, a large amount of amorphous carbon obstructed the pores in the whole anode layer. This carbonaceous species possess relatively low electric conductivity than that deposited in Ni–SDC. Accordingly, the cell performance was related to the deposited area and carbonaceous species, which was determined by the operating conditions and constituent materials. It is concluded from the present investigation that an appropriate combination of fuel electrode material, and cell configuration should be taken into consideration for stable operation in the internal reforming of SOFCs.

## References


1. T. Iida, M. Kawano, T. Matsui, R. Kikuchi, and K. Eguchi, *J. Electrochem. Soc*., **154**, B234 (2007).
2. H. Sumi, P. Puengjinda, H. Muroyama, T Matsui, and K. Eguchi, *J. Electrochem. Soc.*, **196**, 6048 (2011).
3. J. –H. Koh, Y. –S. Yoo, J. –W. Park, H. C. Lim, *Solid State Ionics,* **149**, 157 (2002).
4. A. Weber, B. Sauer, A. C. Mu¨ller, D. Herbstritt, and E. Ivers-Tiffe´e, *Solid State Ionics,* **152-153**, 543 (2002).
5. T. Kim, G. Liu, M. Boaro, S.-I. Lee, J.M. Vohs, R.J. Gorte, O. H. Al-Madhi, B. O. Dabbousi, *J. Power Sources*, **155**, 231 (2006).
6. T. Matsui, R. Kishida, J. Kim, H. Muroyama, and K. Eguchi, *J. Electrochem. Soc*., **157**, B776 (2010).
7. T. Takeguchi, Y. Kani, T. Yano, R. Kikuchi, K. Eguchi, K. Tsujimoto, Y. Uchida, A. Ueno, K. Omoshiki and M. Aizawa, *J. Power Sources*, **112**, 588 (2002).
8. A. Abudula, M. Ihara, H. Komiyama, K. Yamada, *Solid State Ionics*, **86-88**, 1203 (1996).
9. K. Eguchi, H. Kojo, T. Takeguchi, R. Kikuchi, and K. Sasaki, *Solid State Ionics*, **152-153**, 411 (2002).
10. Y. Lin, Z. Zhan, J. Liu, and S. A. Barnett, *Solid State Ionics*, **176**, 1827 (2005).
11. K. Otsuka, Y. Wang, E. Sunada, and I. Yamanaka, *J. Catalysis*, **175**, 152 (1998).
12. T. Zhu and M. Flytzani-Stephanopoulos, *Appl. Catal. A : General*, **208**, 403 (2001).
13. E. S. Putna, J. Stubenrauch, J. M. Vohs, and R. J. Gorte, *Langmuir*, **11**, 4832 (1995).
14. K. T. Lee, C. M. Gore and E. D. Wachsman, *J. Mater. Chem*., **22** 22405 (2012).
15. K. Kitayama, K.Nojiri, T. Sugihara, and T. Katsura, *J. Solid State Chem*., **56**, 1 (1985).
16. M. Zinkevich, D. Djurovic and F. Aldinger, *Solid State Ionics*, **177**, 989 (2006).
17. A. Tsoga, A. Gupta, A Naoumidis and P. Nikolopoulos, *Acta. Mater*, **48**, 4709 (2000).

18. X. –D. Zhou, B. Scarfino and H. U. Anderson, *Solid State Ionics*, **175**, 19 (2004).
19. H. L Tuller and A.S Nowick, *J. Electrochem. Soc.*, **122**, 255 (1975).
20. H. Yahiro, K. Eguchi, and H. Arai, *Solid State Ionics*, **36**, 71 (1989).
21. M. Godickemeier and L. J. Gaucker, *J. Electrochem. Soc*., **145**, 414 (1998).
22. H. Yokokawa, T. Horita, N. Sasaki, K. Yamaji, M. E. Brito, Y.-P. Xiong, H. Kishimoto, *Solid State Ionics*, **174**, 205 (2004).
23. T. Horita, K. Yamaji, T.Kato, N. Sasaki, and H. Yokokawa, *J. Power sources*, **131**, 299 (2004).
24. M. B. Pomfret, J. Marda, G. S. Jackson, B. W. Eichhorn, A. M. Dean, and R. A. Walker, *J. Phys. Chem. C.*, **112**, 5232 (2008).
25. K. Yamaji, H. Kishimoto, Y. Xiong, T. Horita, N. Sasaki, M. E. Brito, and H. Yokokawa, *Solid State Ionics*, **179**, 1596 (2008).
26. K. Yashiro, M. Takase, K. Sato, T. Kawada, and J. Mizusaki, *ECS Trans*., **16**, 213 (2008).
27. M. Koós, S.H.S. Moustafa, E. Szilágyi, and I. Pócsik, *Diam. Relat. Mater.*, **8**, 1919 (1999).
28. M. Weiler, S. Sattel, T. Giessen, K. Jung, H. Ehrhardt, V.S. Veerasamy, and J. Robertson, *Phys. Rev. B*, **53**, 1594 (1996).
29. E. G. Gerstner, P. B. Lukins, D. R. Mckenzie, and D. G. McCulloch, *Phys. Rev. B*, **54**, 14504 (1996).
30. S. Stankovich, D. A. Dikin, R. D. Piner, K. A. Kohlhaas, A. Kleinhammes, Y. Jia, Y. Wu, S. T. Nguyen, R. S. Ruoff, *Carbon*, **45**, 1558 (2007).

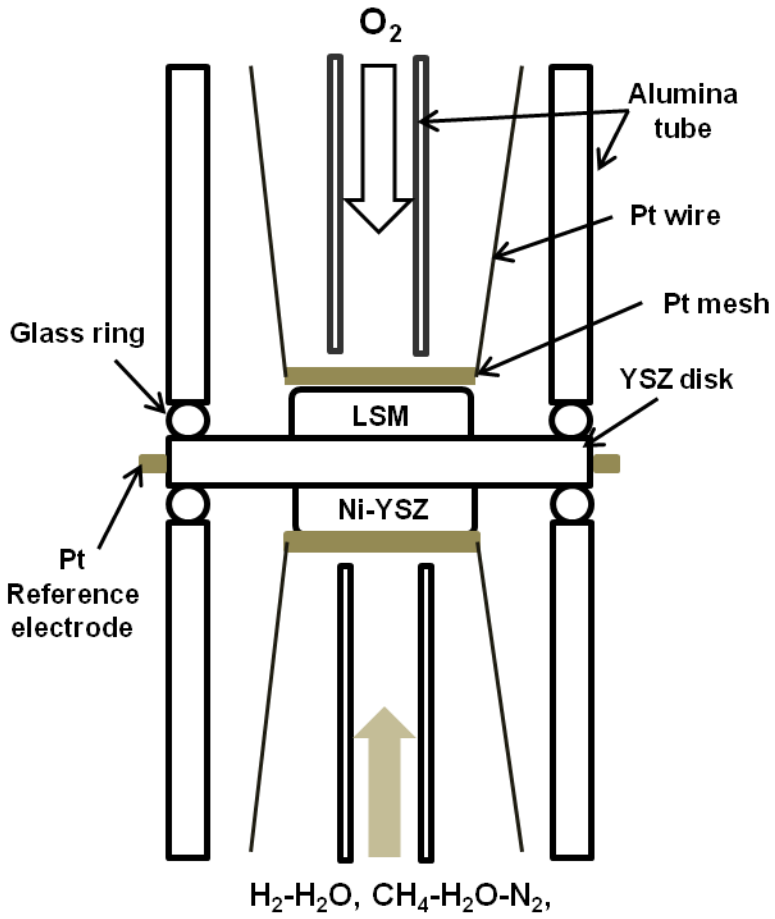


**Figure 1.1. Schematic drawing for the arrangement of testing system.**

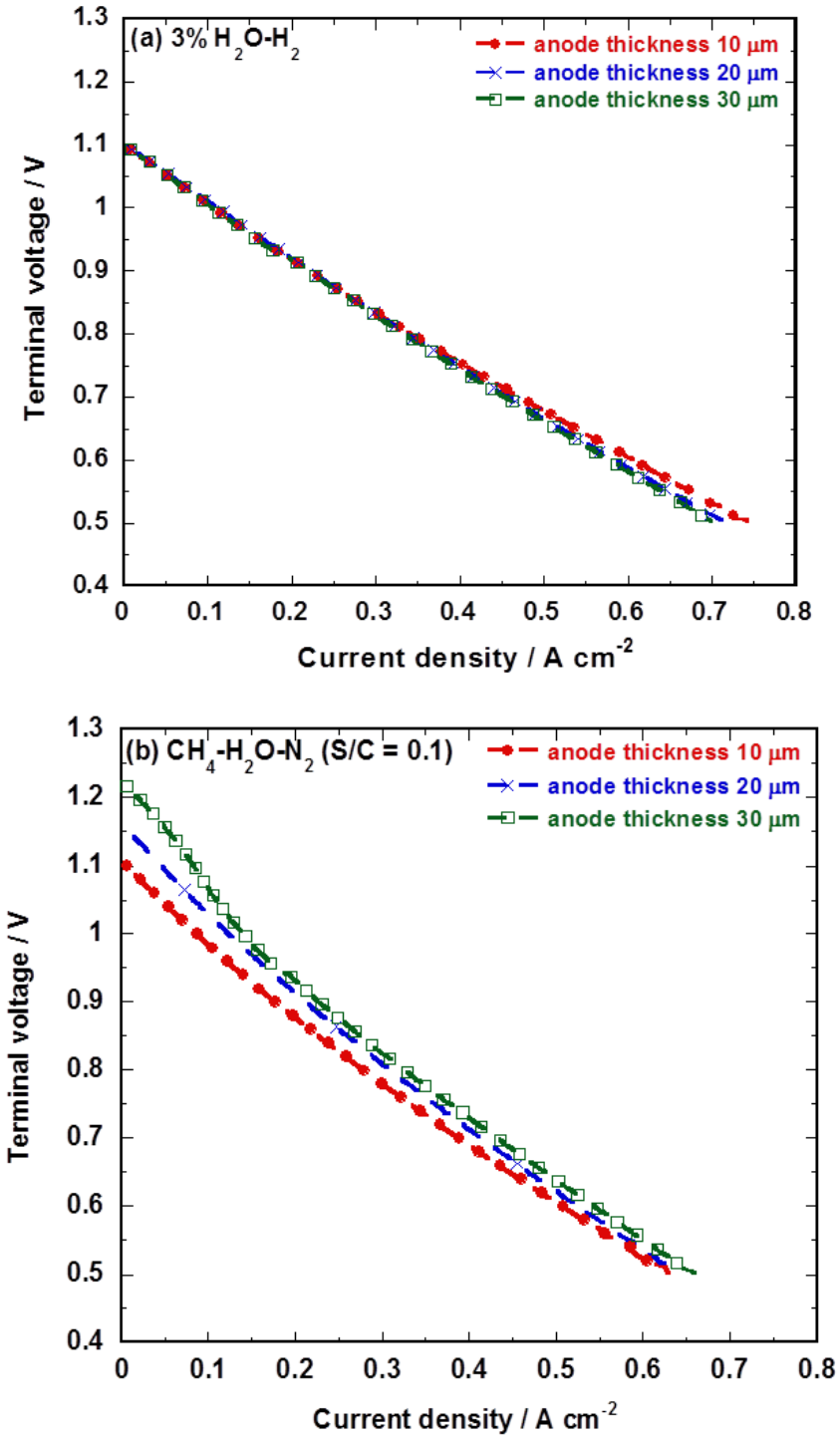


**Figure 1.2. *I-V* curves of single cells employing Ni–YSZ anodes with different thicknesses under supply of (a) 3% $H_2O$–97% $H_2$ and (b) $CH_4$–$H_2O$–$N_2$ mixture (S/C = 0.1) at 1000 ºC.**

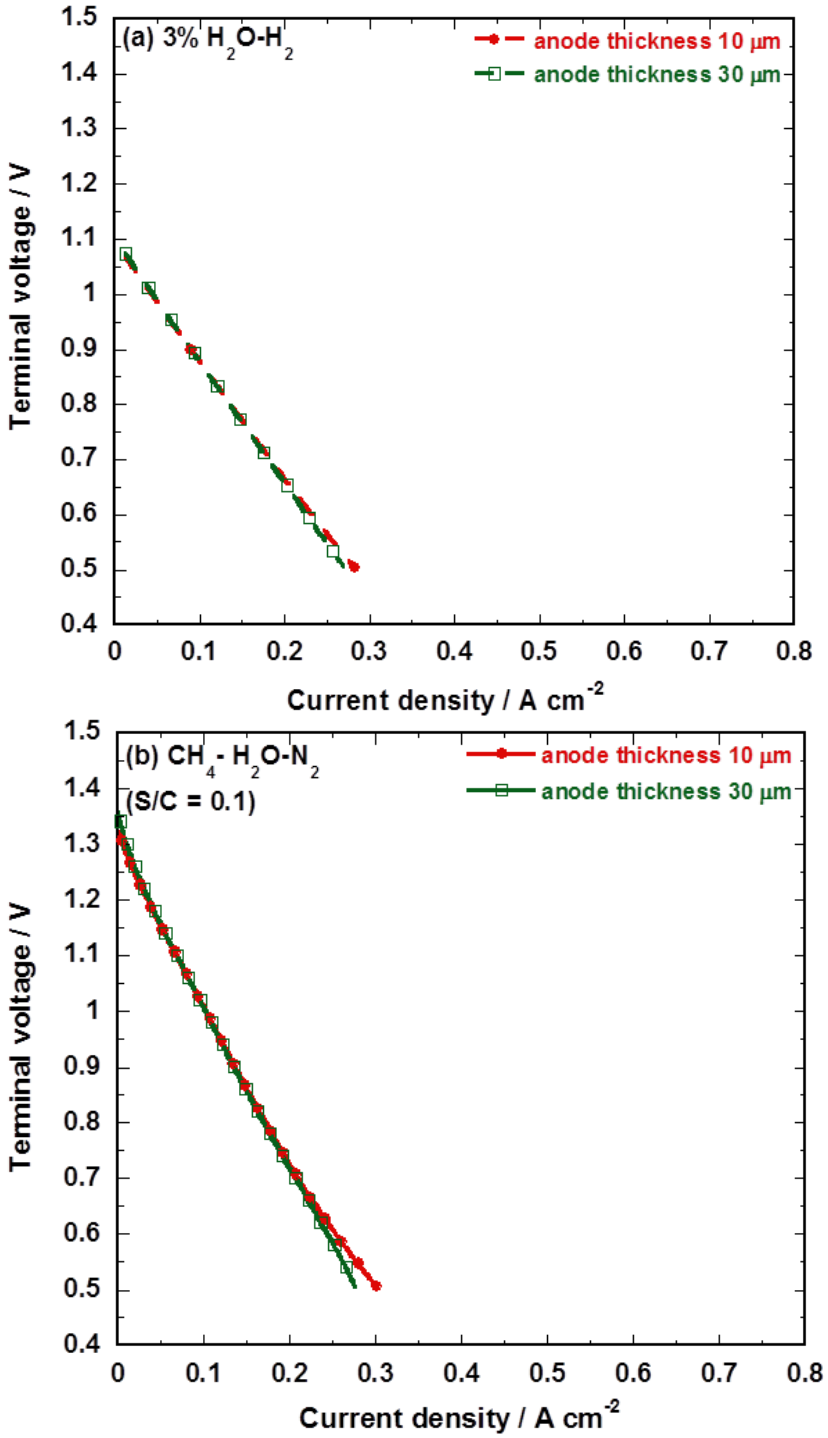


**Figure 1.3. *I-V* curves of single cells employing Ni–SDC anodes with different thicknesses under supply of (a) 3% $H_2O$–97% $H_2$ and (b) $CH_4$–$H_2O$–$N_2$ mixture (S/C = 0.1) at 1000 °C.**

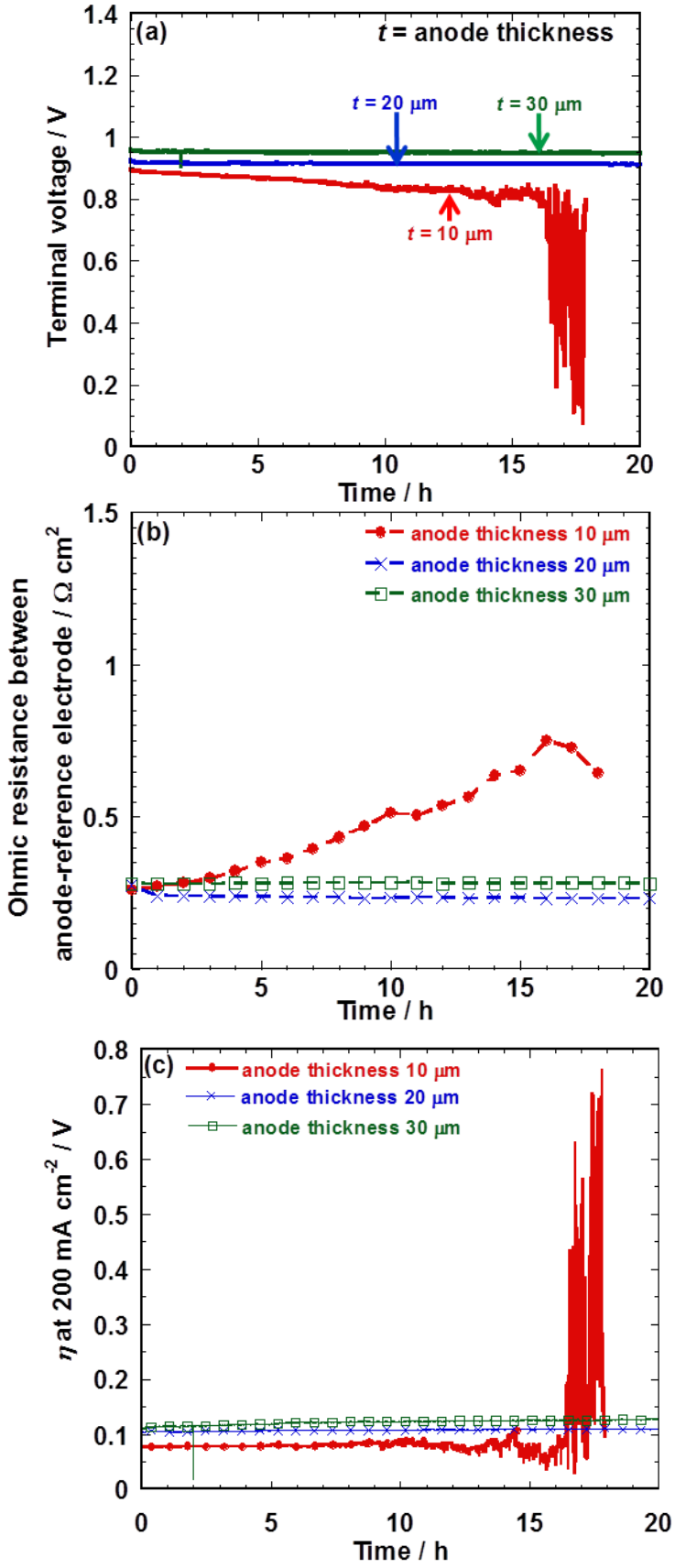


**Figure 1.4. Time courses of (a) terminal voltage, (b) ohmic resistance between anode and reference electrode, and (c) anodic overpotential with Ni–YSZ anodes at a constant current density of 0.2 A $cm^{-2}$ with a supply of $CH_4$–$H_2O$–$N_2$ mixture (S/C = 0.1) at 1000 ºC.**

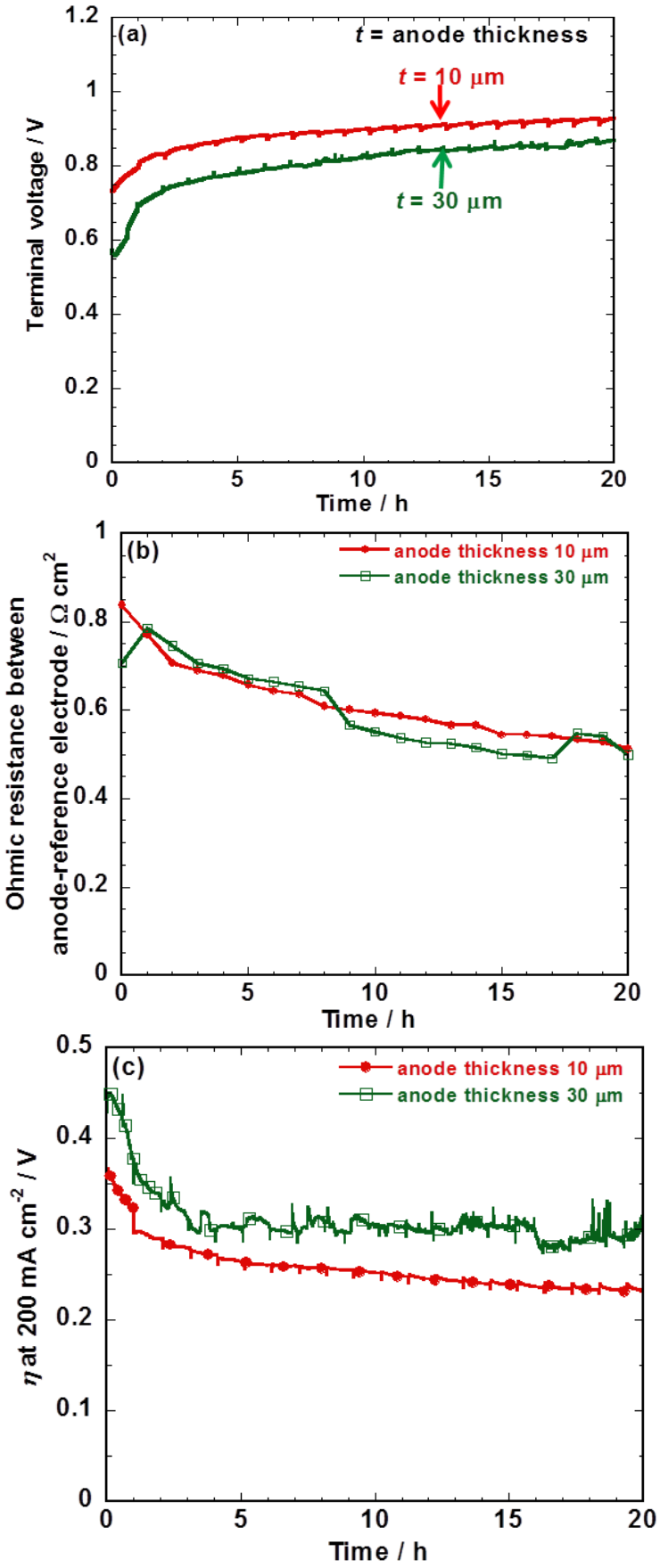


**Figure 1.5. Time courses of (a) terminal voltage, (b) ohmic resistance between anode and reference electrode, and (c) anodic overpotential with Ni–SDC anodes at a constant current density of 0.2 A $cm^{-2}$ with a supply of $CH_4$–$H_2O$–$N_2$ mixture (S/C = 0.1) at 1000 °C**

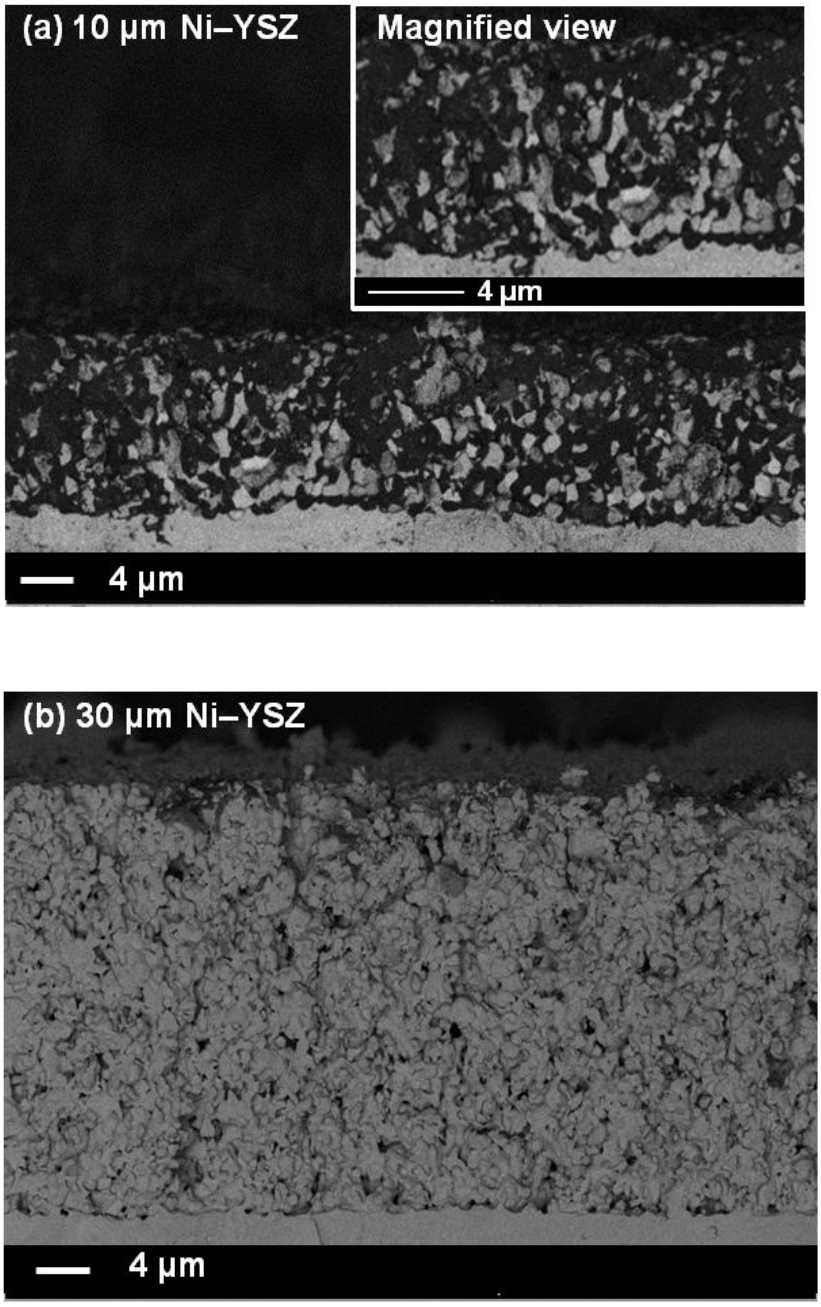


**Figure 1.6. Backscattered electron images of the whole Ni–YSZ and anode layer in (a) 10-μm and (b) 30-μm thicknesses after the discharge at 0.2 A $cm^{-2}$ with a supply of $CH_4$–$H_2O$–$N_2$ mixture (S/C = 0.1) at 1000 °C.**

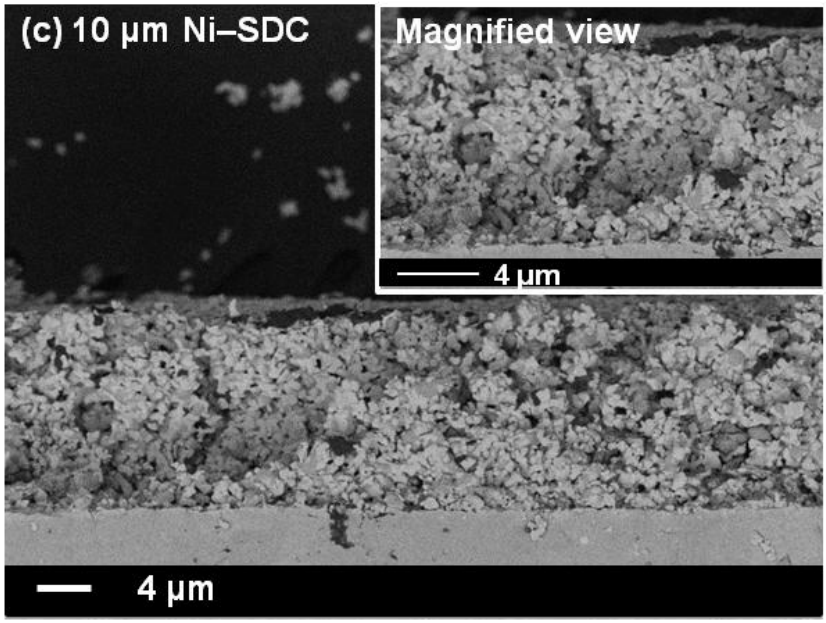


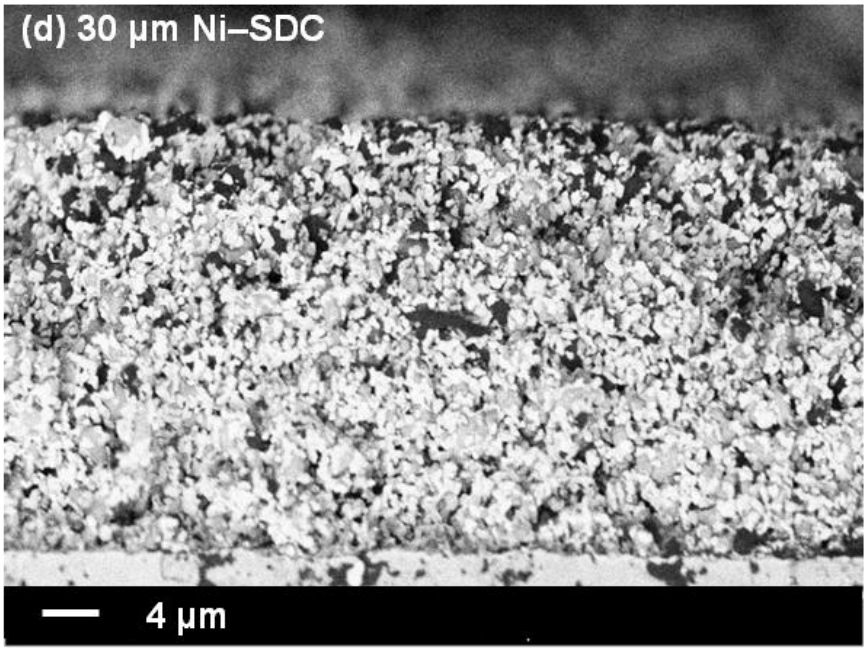


**Figure 1.6. Backscattered electron images of the whole (c, d) Ni–SDC anode layer in (c) 10-μm and (d) 30-μm thicknesses after the discharge at 0.2 A $cm^{-2}$ with a supply of $CH_4$–$H_2O$–$N_2$ mixture (S/C = 0.1) at 1000 ºC.**

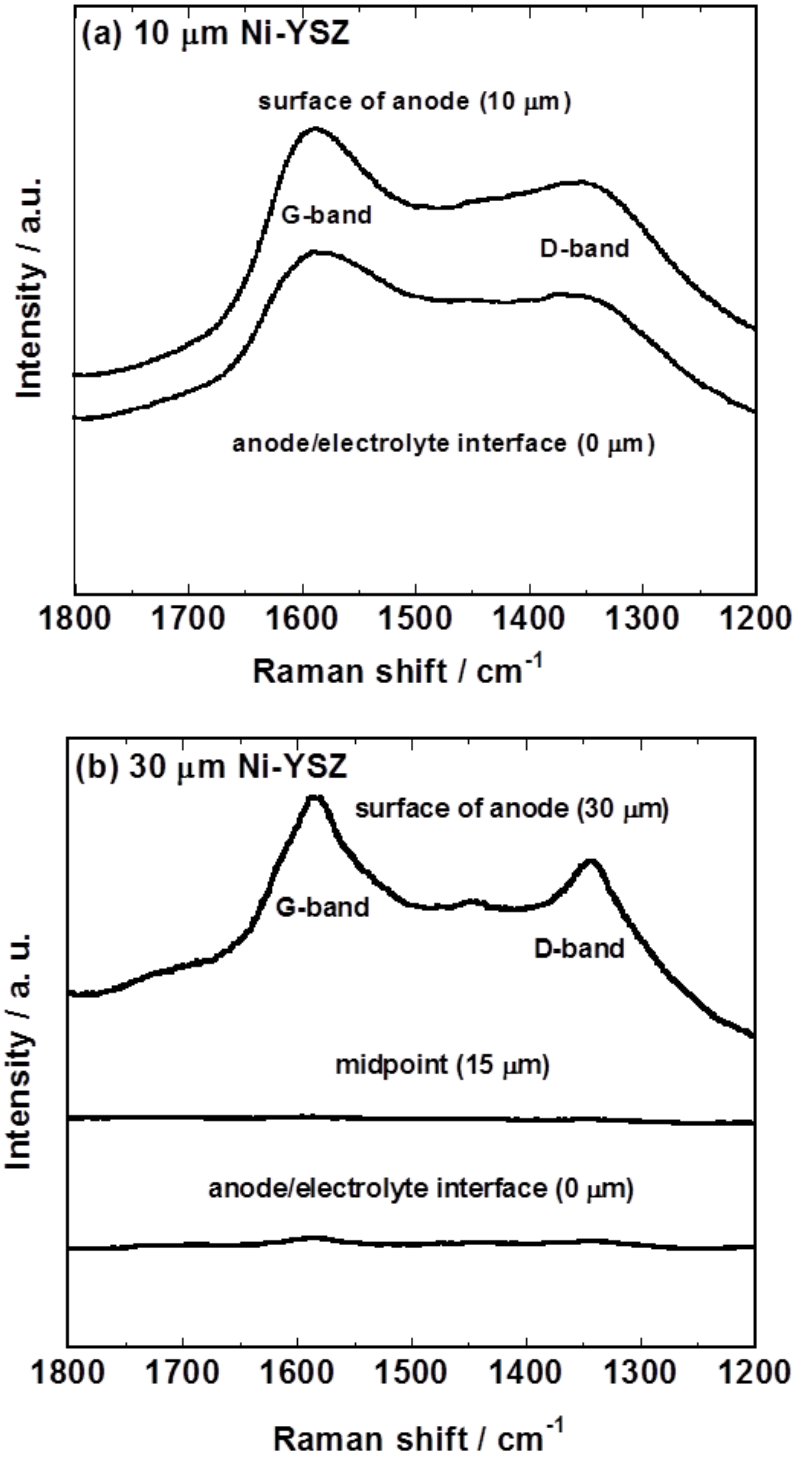


**Figure 1.7. Raman spectra of anode along the electrode thickness direction for (a) 10-μm and (b) 30-μm thick Ni–YSZ after discharge at 0.2 A $cm^{-2}$ with a supply of $CH_4$–$H_2O$–$N_2$ mixture (S/C = 0.1) at 1000 ºC.**

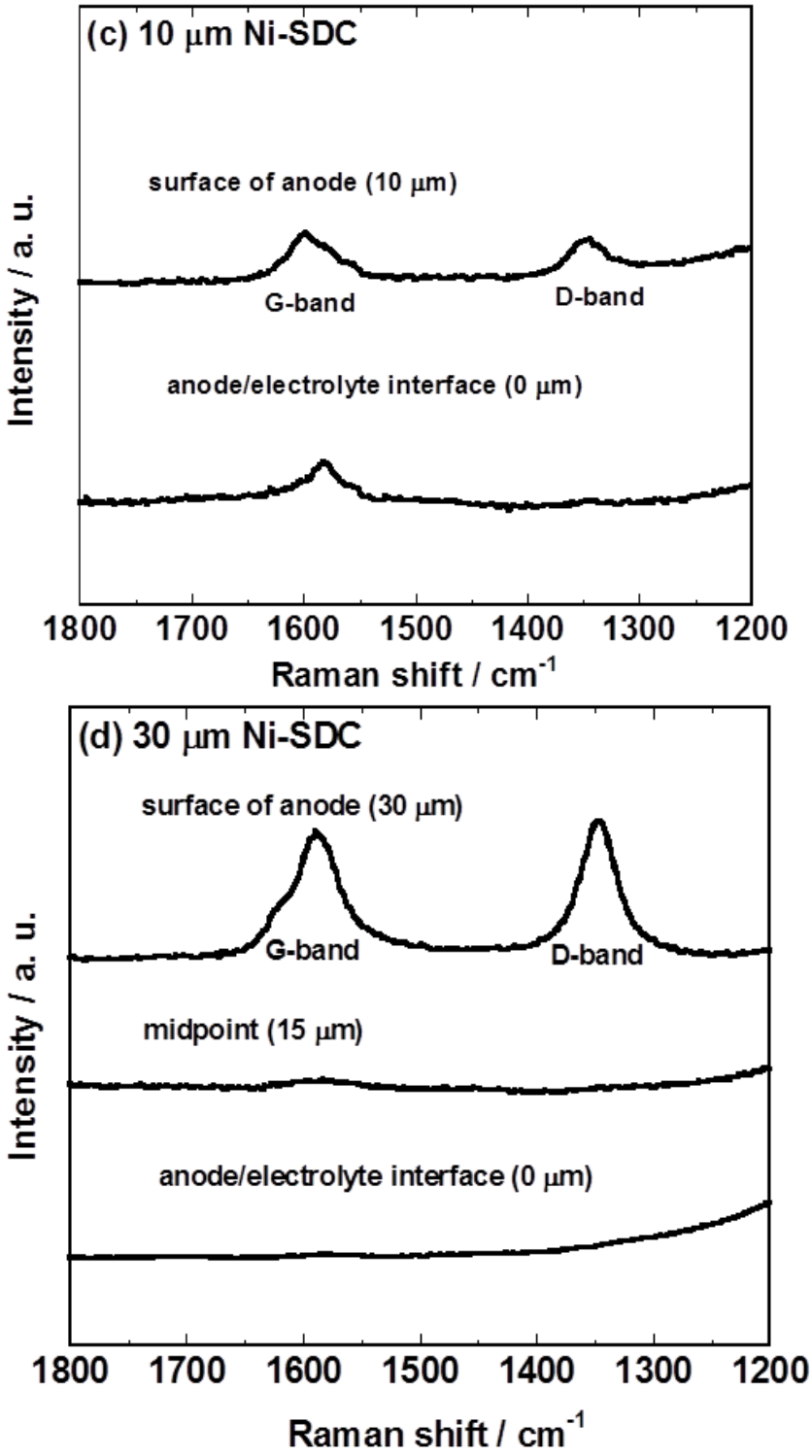


**Figure 1.7. Raman spectra of anode along the electrode thickness direction for (c) 10-μm and (d) 30-μm thick Ni–SDC after discharge at 0.2 A $cm^{-2}$ with a supply of $CH_4$–$H_2O$–$N_2$ mixture (S/C = 0.1) at 1000 ºC.**

# Chapter 2

# Comparison between Internal Steam and $CO_2$ Reforming of Methane for Ni–YSZ and Ni–ScSZ anodes of Solid Oxide Fuel Cells

## 2.1 Introduction

SOFCs are generally operated at a high temperature around 700–1000 ºC, which enable internal reforming of fuels such as hydrocarbon and alcohol. The internal reforming has advantages in terms of energy conversion efficiency and system simplification. However, carbon deposition must be prevented for hydrocarbon- and alcohol-fueled SOFCs. For instance, dry methane is decomposed to hydrogen and solid carbon at high temperatures. Therefore, methane fuel is generally supplied with sufficient steam for the following reaction of reforming [1].

$$CH_4 + H_2O \rightarrow 3H_2 + CO \qquad (2\text{–}1)$$

Carbon deposition can be prevented in $H_2O/CH_4 \geq 1$ as far as estimated from thermodynamic equilibrium at 1000 ºC. At a low ratio of $H_2O/CH_4 < 1$, deposited carbon leads to the degradation of the anode performance due to deactivation of nickel catalyst and inhibition of fuel diffusion [2]. In general, the steam reforming is conducted with an excess amount of steam at approximately $H_2O/CH_4 = 3$. However, the high steam content also induces deterioration of the anode performance by the oxidation of nickel particles [3]. A cermet composed of nickel-yttria-stabilized zirconia (Ni–YSZ) is widely used as an anode of SOFCs. Continuous power generation was also reported to be possible for several hundreds of hours at a low $H_2O/CH_4$ ratio of 0.03, when oxygen ion conductors in the anode changed from YSZ to scandia-stabilized zirconia (ScSZ) and yttriadoped ceria [4,5]. Especially, carbon deposited on Ni–YSZ and Ni–ScSZ anodes had different crystallinities and morphologies after power generation at

$H_2O/CH_4$ = 0.03 [4]. Dopants to zirconia in the anode affect cell performance and durability of the cells [6].

$$CH_4 + CO_2 \rightarrow 2H_2 + 2CO \quad (2–2)$$

Power generation was demonstrated with a supply of $CO_2$–containing gases such as biogas and anode exhaust gas [7, 8]. However, these gases include impurities, which were the main reasons of anode degradation. The compositions of biogas and exhaust gas are variable by operating conditions. Solid carbon is also deposited in $CO_2/CH_4 < 1$ as far as estimated from thermodynamic equilibrium at 1000 ºC. It is important to understand the difference of anode degradation between internal steam and $CO_2$ reforming in carbon deposition conditions. Furthermore, the compositions of hydrogen and carbon monoxide in reformate gases are varied with the initial $H_2O/CH_4$ or $CO_2/CH_4$ ratios and temperatures [9]. The $H_2$/CO ratios in the reformate gas affect the polarization resistance of anodes at 700–1000 ºC [2, 10, 11]. Carbon deposition was also possible by the Boudouard reaction (2–3) and reverse water gas reaction (2–4).

$$2CO \rightarrow C + CO_2 \quad (2–3)$$

$$H_2 + CO \rightarrow C + H_2O \quad (2–4)$$

It is important to determine which affects anode degradation, CO gas or $H_2$–CO mixture, in actual SOFC operating conditions. In this study, the performance and durability of SOFC anodes were investigated in comparison with (*i*) temperatures (750–1000 ºC), (*ii*) Ni–YSZ and Ni–ScSZ anodes, (*iii*) CO–$CO_2$ and $H_2$–CO–$CO_2$ fuels, and (*iv*) internal steam and $CO_2$ reforming of methane. First, the performance and ac impedance of the anode were evaluated with a supply of simulated gases in various ratios of $H_2$, CO, and $CO_2$ at 750–1000 ºC to evaluate the effect of the disproportionation and electrochemical oxidation of carbon monoxide. Second, the performance and durability were examined

with a supply of methane steam or carbon dioxide mixture in $H_2O/CH_4 \leq 1$ and $CO_2/CH_4 \leq 1$ at 850 ºC and 1000 ºC. These conditions induce carbon deposition as far as thermodynamic equilibrium. It was reported that the performance and durability of the Ni–ScSZ anode for internal steam reforming of methane were affected by heat-treatment conditions during cell manufacturing and by the operating temperature during power generation [12-14]. The internal steam and $CO_2$ reforming of methane were compared for the Ni–YSZ and Ni–ScSZ anodes in the carbon deposition conditions. Furthermore, the deposited carbon after power generation was analyzed by Raman spectroscopy and scanning electron microscopy (SEM). The effects of the performance and durability on the crystallinity and morphology of deposited carbon were investigated.

**2.2 Experimental**

Commercial YSZ [$(Y_2O_3)_{0.08}$-$(ZrO_2)_{0.92}$; Tosoh Corp.] and ScSZ [$(Sc_2O_3)_{0.1}$–$(CeO_2)_{0.01}$–$(ZrO_2)_{0.89}$); Daiichi Kigenso Kagaku Kogyo Co., Ltd.] were used as electrolytes. The anode cermets were prepared by mixing NiO (Wako Pure Chemical Industries, Ltd.) and YSZ (or ScSZ) powders in ethanol for 24 h; then the dried powder was fired at 1000 ºC for 5 h in air. The volume ratio of Ni to zirconia was 50:50 after nickel reduction. The anode layer was formed by screen-printing the mixture of the cermet powders (thickness is over 10 μm) and polyethylene glycol 400 on a YSZ disk (thickness: 0.5 mm, diameter: 24 mm), and by calcining at 1300 ºC for 5 h in air. A cathode material was perovskite oxide of LSM ($(La_{0.8}Sr_{0.2})_{0.98}MnO_{3-\delta}$; AGC Seimi Chemical CO., Ltd.). The cathode was also formed by the screen-printing procedure, and by calcining at 1150 ºC for 5 h in air. The diameter of electrode was 6 mm. Reference electrode of platinum wire was fixed around the YSZ disk by a use of

platinum paste.

The power generation tests were conducted at 750, 850 and 1000 ºC by using the instrument as shown in chapter 1. Platinum mesh and pyrex glass were used for current collector and gas sealing, respectively. No carbon deposition was confirmed only on the platinum mesh at 750 and 1000 ºC. After heating the cell to measurement temperature, hydrogen was supplied to anode for nickel reduction. Then, a cell voltage of 0.7 V was kept with a supply of 5 % $H_2O$–$H_2$ gas to anode and 100 % $O_2$ to cathode for 1 h until the cell performance was stabilized. Gaseous mixtures of CO–$CO_2$–$N_2$ (CO : $CO_2$ : $N_2$ = $x$ : 5 : 95-$x$) and $H_2$–CO–$CO_2$–$N_2$ ($H_2$ : CO : $CO_2$ : $N_2$ = 25-$y$ : $y$ : 5 : 70) were supplied to anode. Current-voltage characteristics were evaluated by potentio/galvanostat 1470E (Solartron Analytical), and then the drawn current of 0.050 A $cm^{-2}$ was kept in $x$ = 95 at 750 ºC. AC impedance of anode was measured between anode and reference electrode under open circuit voltage (OCV) in a frequency range from 500 kHz to 1 Hz by impedance analyzer 1455A (Solartron Analytical). For another series of experiment, gaseous mixture of $H_2O$– or $CO_2$–$CH_4$–$N_2$ ($H_2O$ or $CO_2$ : $CH_4$ : $N_2$ = 5 : $z$ : 95-$z$) was supplied to anode. The current-voltage characteristics and the AC impedance of anode were evaluated, and then the passed currents of 0.15 and 0.30 A $cm^{-2}$ were kept in $z$ = 10 ($H_2O/CH_4$ = 0.5 or $CO_2/CH_4$ = 0.5) at 850 and 1000 ºC, respectively. The total gas flow rate was 100 mL $min^{-1}$ to anode and cathode in every condition.

The rates of carbon deposition for Ni–YSZ and Ni–ScSZ were evaluated by a thermogravimetric (TG) analysis (Shimadzu Corp. TGA–50) with a supply of dry methane at 850 and 1000 ºC. The Ni–YSZ or Ni–ScSZ powder (*ca.* 20 mg) was put on a platinum basket in the TG system. Nitrogen was supplied with a flow rate of 90 mL $min^{-1}$ during heating at a rate of 10 K $min^{-1}$, and then hydrogen was supplied with a

flow rate of 30 mL $min^{-1}$ to reduce nickel for 30 min. The weight change was measured with a supply of dry methane (20 mL $min^{-1}$) for 30 min at 850 or 1000 ºC.

Equilibrium compositions were calculated by HSC Chemistry 5.11 (Outokumpu). The Ni–YSZ and Ni–ScSZ anodes after power generation with a supply of $H_2O/CH_4$ = 0.5 and $CO_2/CH_4$ = 0.5 were observed by Raman spectroscopy (Horiba Jobin Yvon LabRAM HR-800) and scanning electron microscopy (Carl Zeiss NVision40). Raman spectra in 1100–1800 $cm^{-1}$ were measured with a use of $Ar^+$ laser of 514.5 nm in air. The secondary electron and backscattered electron images were obtained by the scanning electron microscopy with an accelerating voltage of 1 kV.

## 2.3 Results and Discussion

Figure 2.1 shows the oxygen partial pressure in binary systems of $H_2$–$H_2O$ and CO–$CO_2$ at 750 ºC, 850 ºC and 1000 ºC in equilibrium by HSC Chemistry 5.11. The oxygen partial pressure is lowered either with increasing $H_2$ (or CO) concentration or with decreasing temperature. The oxygen partial pressures become plateau at high CO concentrations in only CO–$CO_2$ system. In these regions, carbon is deposited by the disproportionation of carbon monoxide in the equilibrium. The plateau regions expand at low temperatures. Carbon is expected to be deposited in $CO/(CO+CO_2) \geq 0.95$ at 850 ºC and in $CO/(CO+CO_2) \geq 0.79$ at 750 ºC. In comparison at the same ratios of $H_2/(H_2+H_2O)$ and $CO/(CO+CO_2)$, the oxygen partial pressure in $H_2$–$H_2O$ is larger than that in CO□$CO_2$ at 750 ºC, while the opposite result is obtained at 1000 ºC.

Next, the performance and durability of SOFC anodes were investigated in comparison with CO–$CO_2$ and $H_2$–CO–$CO_2$ fuels. Figure 2.2(a) shows the *I–V* characteristics with a supply of CO–$CO_2$–$N_2$ mixture to the Ni–YSZ anode at 750 ºC.

An OCV rose with increasing CO concentration due to the reduction in oxygen partial pressure, as shown in Fig. 2.1. The OCV agreed with the theoretical electromotive force derived from the Nernst equation in the equilibrium state. The slopes of *I*–*V* curves were almost the same except for $x = 95$ in Fig. 2.2(a). The slope for $x = 95$ was steep at low current densities. Figure 2.2(b) shows the impedance spectra of the anodes at OCVs. The arcs in the Nyquist plot became large at high CO concentrations. Especially, the arc diameter of $x = 95$ was more than 3 times as large as those of $x < 45$. Carbon is expected to be deposited at the composition of $x = 95$ in equilibrium, which leads to the large resistance such as activation and diffusion polarizations. Furthermore, the characteristic frequencies at the top of the arcs were 200 and 20 Hz at $x < 45$ and $x = 95$, respectively. Similar results were obtained in Ref. 15, which suggested the difficulty of CO electrochemical oxidation and gas diffusion due to carbon deposition.

Figure 2.3 shows the (a) *I*–*V* characteristics and (b) impedance spectra of the anodes with a supply of the $H_2$–CO–$CO_2$–$N_2$ mixture to the Ni–YSZ anode at 750 ºC. The *I*–*V* curve of y = 25 was slightly lower than those in the other conditions. For the fuels containing hydrogen, steam is produced by power generation and the water gas shift reaction proceeds

$$CO + H_2O \rightarrow H_2 + CO_2 \qquad (2\text{–}5)$$

However, Reaction (2–5) is impossible for the fuel without hydrogen because of no production of steam by power generation. According to results of impedance spectra, the arcs became large at high CO concentrations because diffusion of CO is slow. The result in Fig. 2.3(b) suggests that carbon was deposited more dominantly by the disproportionation of carbon monoxide (2–3) than by the reverse water gas reaction (2–4) at 750 ºC. The same series of experiments, as shown in Fig. 2.2 and 2.3, were

conducted for the Ni–YSZ and Ni–ScSZ anodes at 850 and 1000 ºC. Figure 2.4 shows the polarization resistance of the anodes estimated from the impedance spectra as a function of $CO/(H_2+CO)$ and $CO/(CO+CO_2)$ ratios at 750, 850, and 1000 ºC. The polarization resistance of the Ni–ScSZ anode was comparable to that of the Ni–YSZ anode in all conditions. The increasing rate of the polarization resistance as a function of CO concentration was large at 750 and 850 ºC. This result suggests that the electrochemical oxidation of carbon monoxide was difficult at low temperatures.

The polarization resistance increased steeply in $CO/(CO+CO_2) \geq 0.8$ at 750 ºC. This condition was within the carbon deposition region in Fig. 2.1. Figure 2.5 shows the time courses of cell voltage and anodic overpotential with a supply of the $CO–CO_2$ mixture ($CO:CO_2$ = 95:5) and a drawn current of 0.05 A $cm^{-2}$ at 750 ºC. The cell voltage decreased gradually because of the increase in the anodic overpotential. The deterioration rate for the Ni–YSZ anode was almost the same (2 mV $h^{-1}$) as that for the Ni–ScSZ anode. After power generation, a large amount of carbon was observed on the anodes. This result supported that carbon was deposited by the disproportionation of carbon monoxide in $CO/(CO+CO_2) = 0.95$ at 750 ºC. Power generation in the $CO–CO_2$ binary system becomes unstable at low temperatures.

First, the region of carbon deposition was confirmed for the $CO_2–CH_4$ system in equilibrium. Figure 2.6 shows the thermodynamic equilibrium compositions in the $CO_2–CH_4–N_2$ mixture at 1000 ºC. Carbon is deposited at $CO_2/CH_4 < 1$ in equilibrium. This result is analogous to $H_2O/CH_4 < 1$ with a supply of the $H_2O–CH_4–N_2$ mixture [4]. The region of carbon deposition expands at low temperatures. For instance, carbon is deposited in the region of $CO_2/CH_4 < 1.5$ at 750 ºC. The amount of hydrogen increases with a rise in initial $CH_4$ composition, whereas that of carbon monoxide is unchanged.

This result suggests that the cracking of methane is promoted at low $CO_2/CH_4$ ratios

$$CH_4 \rightarrow 2H_2 + C \qquad (2\text{–}6)$$

The ratio of hydrogen and carbon monoxide depends on the initial ratio of $CO_2/CH_4$. For instance, the percentage of hydrogen and carbon monoxide in the gas phase at $z'$ = 0.10 ($CO_2/CH_4$ = 0.50) are 17% and 8%, respectively, whereas those at $z'$ = 0.20 ($CO_2/CH_4$ = 0.25) are 32% and 8%, respectively. The ratio of hydrogen and carbon monoxide is different between steam and $CO_2$ reforming. The percentage of hydrogen and carbon monoxide after reforming the gaseous mixture of $H_2O$ : $CH_4$ : $N_2$ = 0.05 : 0.10 : 0.85 ($H_2O/CH_4$ = 0.50) are 22% and 4%, respectively. The CO concentration after $CO_2$ reforming is larger than that after steam reforming. The polarization resistance for $CO_2$ reforming is predicted to be higher due to high CO concentration than that for steam reforming. Next, the rate of carbon deposition was evaluated with a supply of dry methane by TG analysis. Figure 2.7 shows the time course of weight gain by carbon deposition for the Ni–YSZ and Ni–ScSZ powders at 850 and 1000 ºC. The amount of deposited carbon at 1000 ºC was larger than that at 850 ºC because the cracking of methane was promoted at high temperatures. The rate of carbon deposition for Ni–YSZ was larger than that for Ni–ScSZ at 1000 ºC, whereas the order was opposite at 850 ºC. Gunji *et al.* reported that the amount of deposited carbon was changed by heat-treatment conditions during cell manufacturing for Ni–ScSZ [12]. The heat-treatment conditions affected the crystal structure of ScSZ. ScSZ with the cubic phase at room temperature facilitated carbon deposition as compared with the rhombohedral phase. Furthermore, an additive of $Al_2O_3$, $Bi_2O_3$, $Ga_2O_3$, or $CeO_2$ in ScSZ led to the stabilization of the cubic phase at room temperature [16-18]. In this chapter, 1 mol % of $CeO_2$-doped ScSZ was used. The crystalline structure was confirmed to be cubic for both YSZ and ScSZ at

every temperature by X-ray diffraction. The results in Fig. 2.8 suggest that the rate of carbon deposition was affected by the dopant in zirconia and by the operating temperature. Figure 2.8 shows the *I–V* characteristics with a supply of $CO_2/CH_4$ = 0.5 and 1.0 to the Ni–YSZ and Ni–ScSZ anodes at (a) 850 and (b) 1000 ºC. At $CO_2/CH_4$ = 0.5, the OCV was *ca.* 1.2 and 1.3 V at 850 and 1000 ºC, respectively, which almost agreed with the theoretical value derived from the equilibrium compositions in Fig. 2.6. The slope of the *I–V* curve at $CO_2/CH_4$ = 0.5 in the carbon deposition condition was steeper than that at $CO_2/CH_4$ = 1.0 in a region of low current densities at 850 and 1000 ºC. However, the slopes at $CO_2/CH_4$ = 0.5 and 1.0 were almost the same at high current densities. Steam and carbon dioxide were produced by the power generation at high current densities, which promoted reforming of methane, as expressed by Reactions (2–1) and (2–2). The cell performance for the Ni–YSZ anode was lower than that for the Ni–ScSZ anode at $CO_2/CH_4$ = 0.5 in the carbon deposition condition at 1000 ºC. The impedance spectra of the anodes at OCV were obtained as shown in Fig. 2.9. The polarization resistance of the Ni–YSZ anode was larger than that of the Ni–ScSZ anode at 1000 ºC because carbon was deposited more easily as was observed in TG analysis, as shown in Fig. 2.7. On the contrary, the resistance of the Ni-YSZ anode was smaller than that of the Ni–ScSZ anode at 850 ºC. This result also corresponds to the TG analysis. Thus, the rate of carbon deposition was closely related to the polarization resistance of the Ni–YSZ and Ni–ScSZ anodes. In comparison between steam and $CO_2$ reforming, the polarization resistance in $H_2O/CH_4$ = 0.5 was smaller than that in $CO_2/CH_4$ = 0.5 for both Ni–YSZ and Ni–ScSZ anodes at 1000 ºC. This result suggested that the reforming of methane and electrochemical oxidation of fuel for steam reforming were promoted more than that for $CO_2$ reforming in the carbon deposition condition.

The durability was evaluated for Ni–YSZ and Ni–ScSZ anodes in the carbon deposition conditions. Figure 2.10 shows the time courses of cell voltage and anodic overpotential in $H_2O/CH_4$ = 0.5 and $CO_2/CH_4$ = 0.5 at 850 and 1000 ºC. At 850 ºC, no degradation was observed for the Ni–YSZ anode, whereas the cell voltage decreased slightly for the Ni–ScSZ anode. The decreasing rate of cell voltage corresponded to the increasing rate of anodic overpotential. The polarization resistances of the anodes were also reported to increase with elapsed time, which was mainly caused by carbon deposition [19]. At 1000 ºC, the degradation rate for the Ni–YSZ anode was larger than that for the Ni–ScSZ anode. Shiratori and Sasaki also reported the stable power generation with a supply of $CO_2$–$CH_4$ mixture for the Ni–ScSZ anode [20]. The cell voltage and anodic overpotential were stable during steam reforming for the Ni–ScSZ anode. Furthermore, both Ni–YSZ and Ni–ScSZ anodes were promoted to deteriorate for $CO_2$ reforming at 1000 ºC. Table 2.1 summarizes the initial polarization resistances of the Ni–YSZ and Ni–ScSZ anodes and the increasing rates of anodic overpotential for the initial 20 h with supplies of $H_2O/CH_4$ = 0.5 and $CO_2/CH_4$ = 0.5 at 850 and 1000 ºC. The initial polarization resistance of the anodes for $CO_2$ reforming was larger than that for steam reforming. The resistance was larger for the Ni–ScSZ anode at 850 ºC and for Ni–YSZ anode at 1000 ºC. In the durability test, the change in anodic overpotential was less than 1 mV $h^{-1}$ for the initial 20 h at 850 ºC. However, the degradation of the Ni–YSZ anode was remarkable at 1000 ºC. The increasing rate of anodic overpotential was 8.6 mV $h^{-1}$ for $CO_2$ reforming, which is larger than that for steam reforming at 1000 ºC.

After power generation, the deposited carbon on the Ni–YSZ and Ni–ScSZ anodes was observed by Raman spectroscopy and SEM. Figure 2.11 shows the Raman

spectra after power generation in $H_2O/CH_4$ = 0.5 and $CO_2/CH_4$ = 0.5 at 850 and 1000 ºC. Two peaks at 1350 $cm^{-1}$ (D-band) and 1585 $cm^{-1}$ (G-band) were attributable to amorphous carbon and crystalline graphite, respectively. At 850 ºC, small peaks of the G-band were observed in every condition. This result supported that the suppression of carbon deposition enabled the low degradation rate, as shown in Fig. 2.10. Yamaji *et al*. observed the strong G-band after exposure to 1.2% $H_2O$–$CH_4$ without current loading at 800 ºC [21]. Pomfret *et al*. reported that the intensity of the G-band decreased with a rise in current density because of the electrochemical oxidation of deposited carbon [22]. The G-band became small because of the current loading of 0.15 A $cm^{-2}$ at 850 ºC in this study. The intensity of the G-band gained at a high temperature of 1000 ºC. Furthermore, the intensity of the D-band increased only for the Ni–YSZ anode. The ratios of peak intensities between the D-band and G-band ($I_D/I_G$) were 0.25 and 0.75 for the Ni–YSZ anode after power generation in $H_2O/CH_4$ = 0.5 and $CO_2/CH_4$ = 0.5, respectively. The degradation rate was the largest for the Ni–YSZ anode in $CO_2/CH_4$ = 0.5, as shown in Fig. 2.10. Therefore, it is likely that the deposition of amorphous carbon gave rise to the deterioration of the cell performance.

Figure 2.12 shows the SEM images for the Ni–YSZ and Ni–ScSZ anodes after power generation in $H_2O/CH_4$ = 0.5 and $CO_2/CH_4$ = 0.5 at 1000 ºC. The black areas in the backscattered electron images were ascribed to deposited carbon by an energy-dispersive X-ray spectrometer with an accelerating voltage of 10 kV. Two morphological types of deposited carbon were observed on the Ni–YSZ anode. One was a gumlike carbon marked with dotted lines, and the other was carbon with an angular surface covering on Ni particles marked with solid lines. The gumlike carbon was observed only on the Ni–YSZ anode, which corresponded to amorphous carbon judging

from the Raman spectra in Fig. 2.11. This carbon was likely to cause deterioration by not only the decrease in catalytic activity but also the inhibition of gas diffusion. The amorphous carbon was more abundantly observed after $CO_2$ reforming than after steam reforming. The angular carbon was also observed on the Ni–ScSZ anode, which corresponded to graphite. This carbon was expected to be electrically conductive as compared to the amorphous one, although it caused the deactivation of the nickel catalyst. Furthermore, the rod-shaped carbon was observed only on the Ni–ScSZ anode marked with arrows in Fig. 2.12. The rod-shaped carbon with various radii was confirmed after $CO_2$ reforming. This carbon, being ascribed to crystalline graphite due to the absence of the D-band, did not cover Ni particles. This rod-shaped graphite affected the catalytic activity less than the amorphous carbon. The crystallinity and morphology of deposited carbon strongly influenced the performance and durability at low $H_2O/CH_4$ and $CO_2/CH_4$ ratios.

## 2.4 Conclusion

In this chapter, the cell performance and AC impedance of anode were evaluated in simulated gases with various ratios of $H_2$, CO and $CO_2$. The polarization resistance increased with a rise in CO concentration at low temperatures because of the difficulty of electrochemical oxidation of carbon monoxide. Carbon was deposited by the disproportionation of carbon monoxide in CO–$CO_2$ mixture ($CO:CO_2$ = 95:5) at 750 ºC, which led to degraded performance. The durability for the Ni–YSZ and Ni–ScSZ anodes were also examined to be compared between internal steam and $CO_2$ reforming of methane. The amount of deposited carbon at 1000 ºC was larger than that at 850 ºC, because the cracking of methane was facilitated at high temperatures. The descending

order of degradation rate was Ni–YSZ ($CO_2$) > Ni–YSZ (steam) > Ni–ScSZ ($CO_2$) > Ni–ScSZ (steam) at 1000 ºC. The amorphous carbon was observed only on the Ni–YSZ anode, which was possible to cause deterioration by the decrease of nickel catalytic activity and the inhibition of gas diffusion. In contrast, the rod-shaped crystalline graphite was observed only on the Ni–ScSZ anode. The cell voltage and anodic overpotential were stable for the Ni–ScSZ anode. The crystallinity and morphology of deposited carbon strongly influenced the performance of durability at low $H_2O/CH_4$ and $CO_2/CH_4$ ratios.

**References**


1. K. Eguchi, H. Kojo, T. Takeguchi, R. Kikuchi and K. Sasaki, Solid State Ionics, **152-153**, 411 (2002).
2. T. Takeguchi, Y. Kani, T. Yano, R. Kikuchi, K. Eguchi, K. Tsujimoto, Y. Uchida, A. Ueno, K. Omoshiki and M. Aizawa, J. Power Sources, **112**, 588 (2002).
3. T. Matsui, R. Kishida, J-Y. Kim, H. Muroyama and K. Eguchi, J. Electrochem. Soc., **157**, B776 (2010).
4. H. Sumi, K. Ukai, Y. Mizutani, H. Mori, C-J Wen, H. Takahashi and O. Yamamoto, Solid State Ionics, **174**, 151 (2004).
5. E. P. Murray, T. Tsai and S. A. Barnett, Nature, **400**, 649 (1999).
6. Z. Gao, K. Sekizawa and K. Eguchi, Electrochemistry, **67**, 336 (1999).
7. Y. Shiratori, T. Oshima and K. Sasaki, Int. J. Hydrogen Energy, **33**, 6316 (2008).
8. R. Peter, E. Riensche and P. Cremer, J. Power Sources, **86**, 432 (2000).
9. K. Sasaki and Y. Teraoka, J. Electrochem. Soc., **150**, A878 (2003).
10. K. Sasaki, Y. Hori, R. Kikuchi, K. Eguchi, A. Ueno, H. Takeuchi, M. Aizawa, K.

Tsujimoto, H. Tajiri, H. Nishikawa and Y. Uchida, J. Electrochem. Soc., **149**, A227 (2002).

11. A. Weber, B. Sauer, A. C. Müller, D. Herbstritt and E. Ivers-Tiffee, Solid State Ionics, **152-153**, 543 (2002).
12. A. Gunji, C. Wen, J. Otomo, T. Kobayashi, K. Ukai, Y. Mizutani and H. Takahashi, J. Power Sources, **138**, 285 (2004).
13. K. Ke, A. Gunji, H. Mori, S. Tsuchida, H. Takahashi, K. Ukai, Y. Mizutani, H. Sumi, M. Yokoyama and K. Waki, Solid State Ionics, **177**, 541 (2006).
14. T. Matsui, T. Iida, R. Kikuchi, M. Kawano, T. Inagaki and K. Eguchi, J. Electrochem. Soc., **155**, B1136 (2008).
15. V. Alzate-Restrepo, J. M. Hill, J. Power Sources, **195**, 1344 (2010).
16. M. Mizutani, M. Tamura, M. Kawai and O. Yamamoto, Solid State Ionics, **72**, 271 (1994).
17. Y. Arachi, T. Asai, O. Yamamoto, Y. Takeda, N. Imanishi, K. Kawate and C. Tamakoshi, J. Electrochem. Soc., **148**, A520 (2001).
18. M. Hirano, T. Oda, K. Ukai and Y. Mizutani, Solid State Ionics, **158**, 215 (2003).
19. J-H. Koh, Y-S. Yoo, J-W. Park and H. C. Lim, Solid State Ionics, **149**, 157 (2002).
20. Y. Shiratori and K. Sasaki, J. Power Sources, **180**, 738 (2008).
21. K. Yamaji, H. Kishimoto, Y. Xiong, T. Horita, N. Sakai, M. E. Brito and H. Yokokawa, Solid State Ionics, **179**, 1526 (2008).
22. M. B. Pomfret, J. Marda, G. S. Jackson, B. W. Eichhorn, A. M. Dean and R. A. Walker, J. Phys. Chem. C., **112**, 5232 (2008).

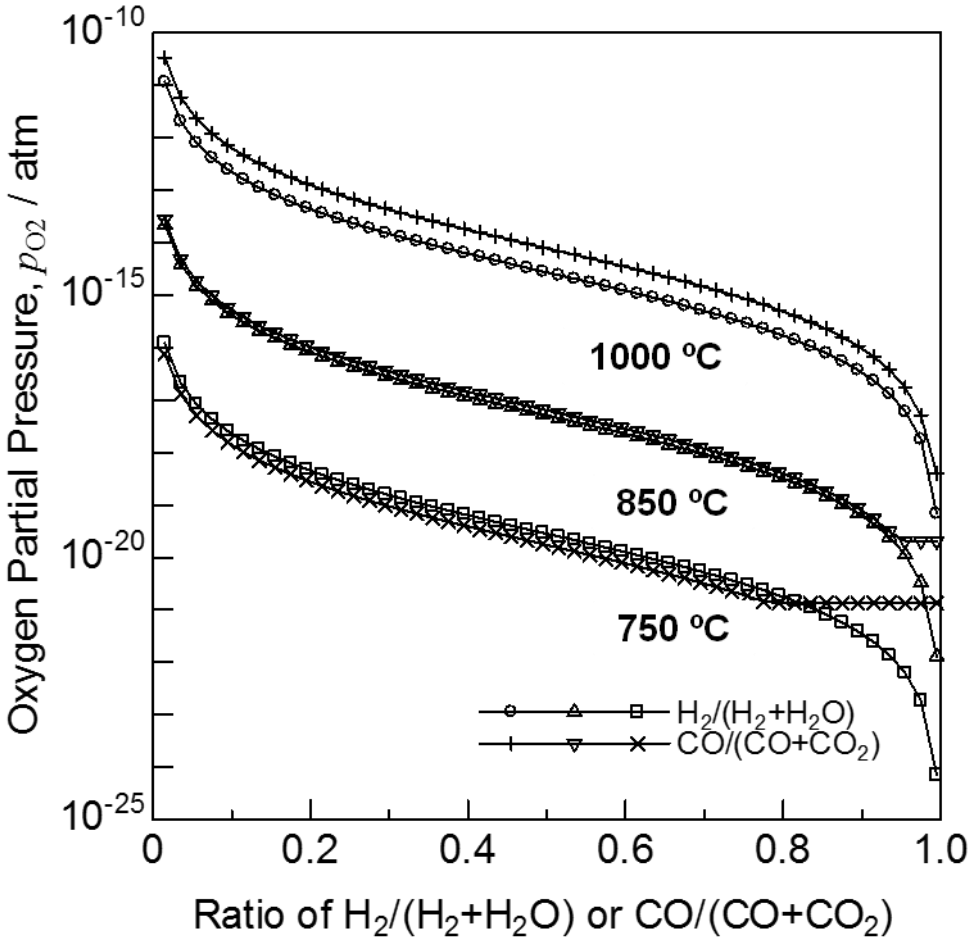


**Figure 2.1. Calculated oxygen partial pressures as a function of $H_2/(H_2+H_2O)$ or $CO/(CO+CO_2)$ ratio at 750, 850 and 1000 °C in equilibrium by HSC Chemistry 5.11.**

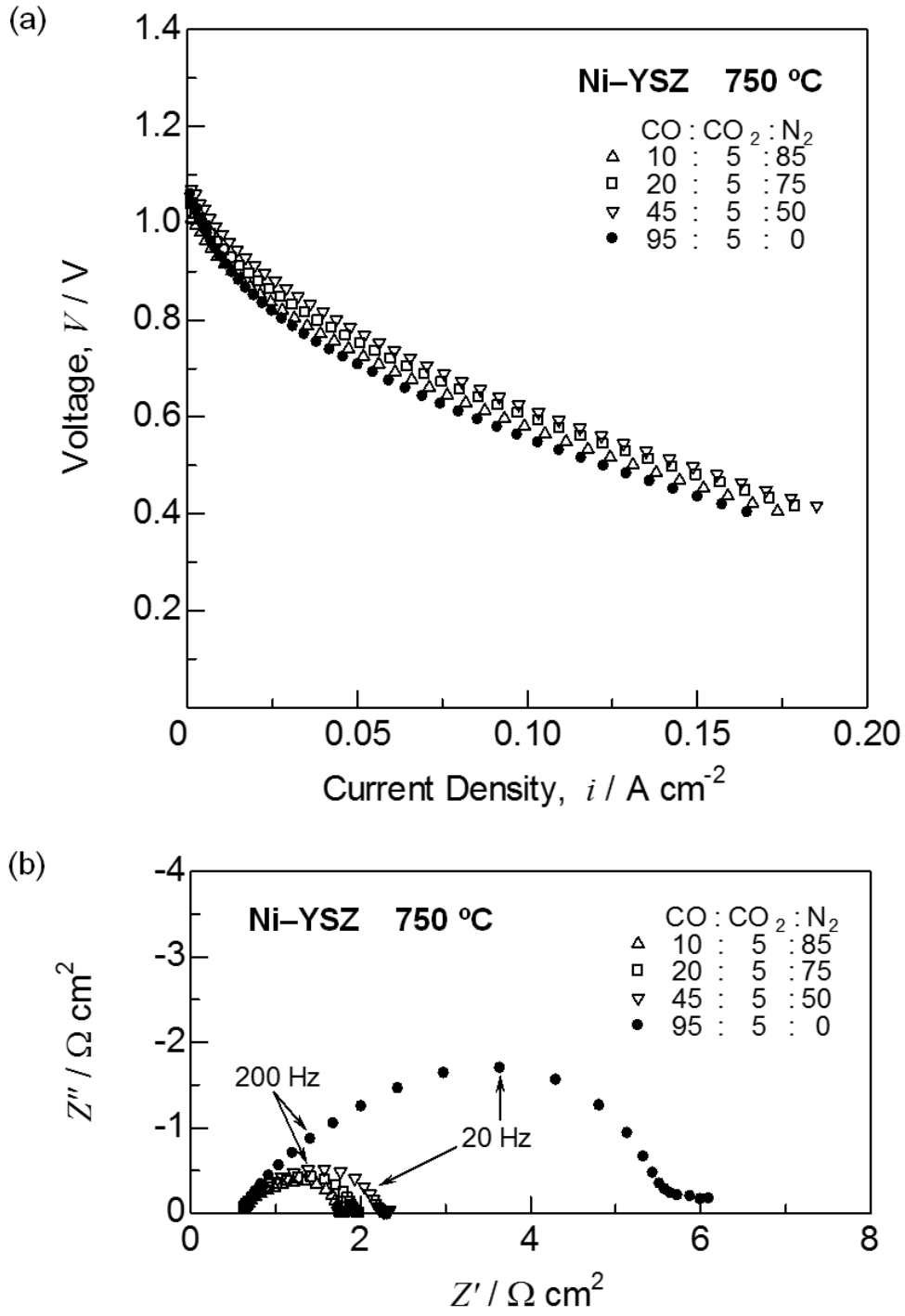


**Figure 2.2. (a) Current-voltage characteristics and (b) impedance spectra with a supply of CO-$CO_2$-$N_2$ mixture (CO : $CO_2$ : $N_2$ = *x* : 5 : 95-*x*) to the Ni–YSZ anode at 750 ºC.**

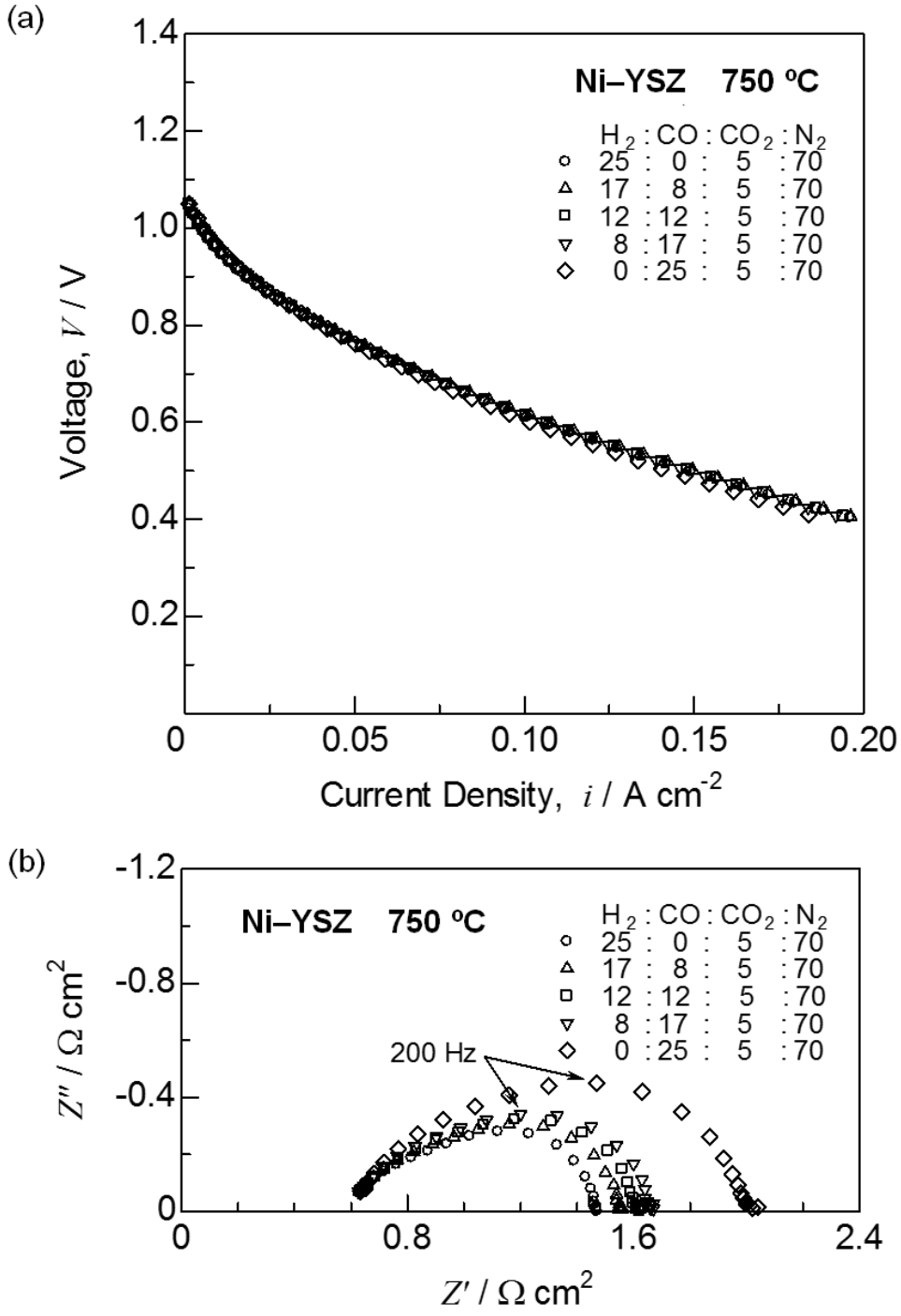


**Figure 2.3. (a) Current-voltage characteristics and (b) impedance spectra with a supply of $H_2$-CO-$CO_2$-$N_2$ mixture ($H_2$ : CO : $CO_2$ : $N_2$ = 25-*y* : *y* : 5 : 70) to the Ni–YSZ anode at 750 °C.**

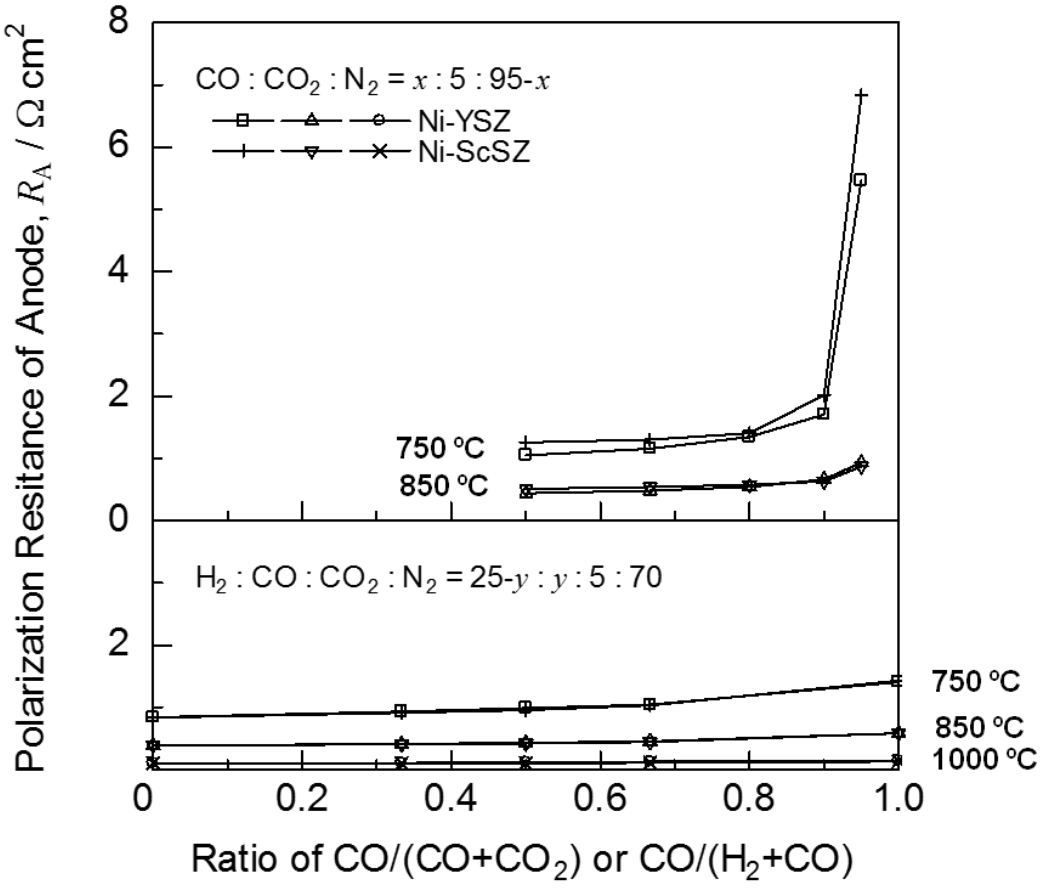


**Figure 2.4. Polarization resistances of the Ni-YSZ and Ni-ScSZ anodes as a function of CO/($H_2$+CO) or CO/(CO+$CO_2$) ratio at 750, 850 and 1000 °C.**

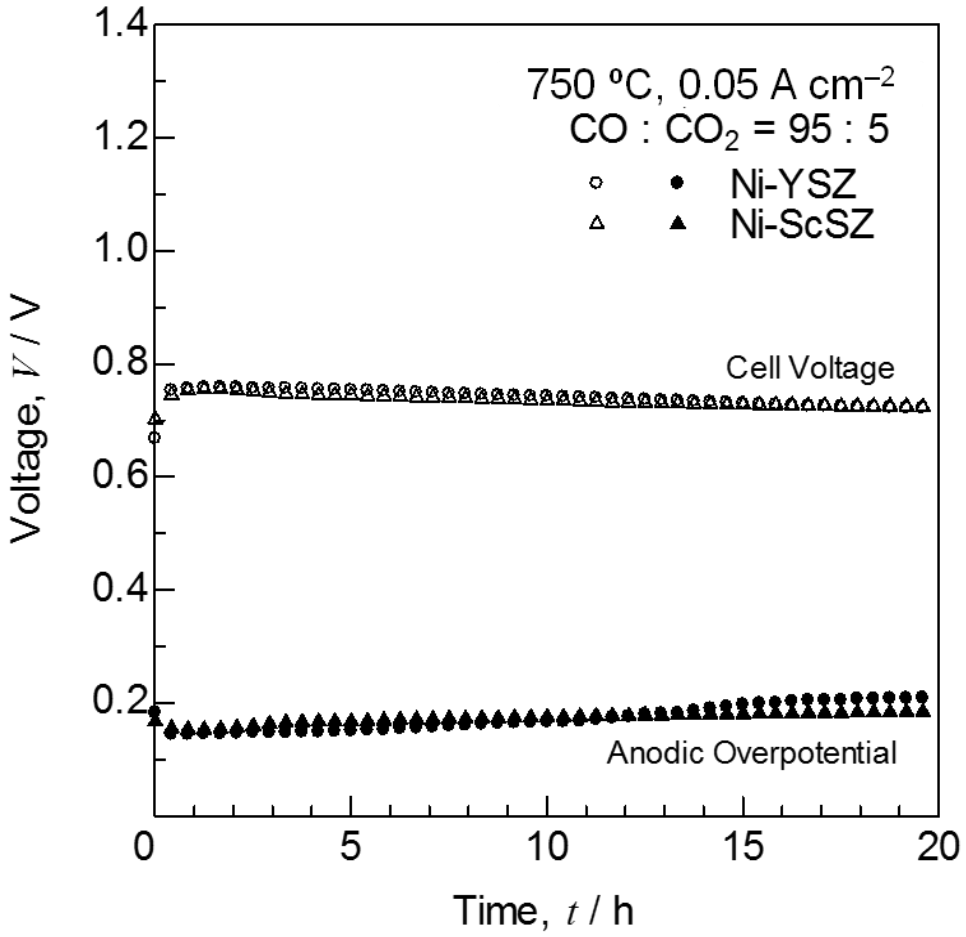


**Figure 2.5. Time courses of cell voltage and anodic overpotential with a supply of CO-$CO_2$ mixture (CO : $CO_2$ = 95 : 5) to the Ni–YSZ and Ni–ScSZ anodes and a drawn current of 0.05 A $cm^{-2}$ at 750 ºC.**

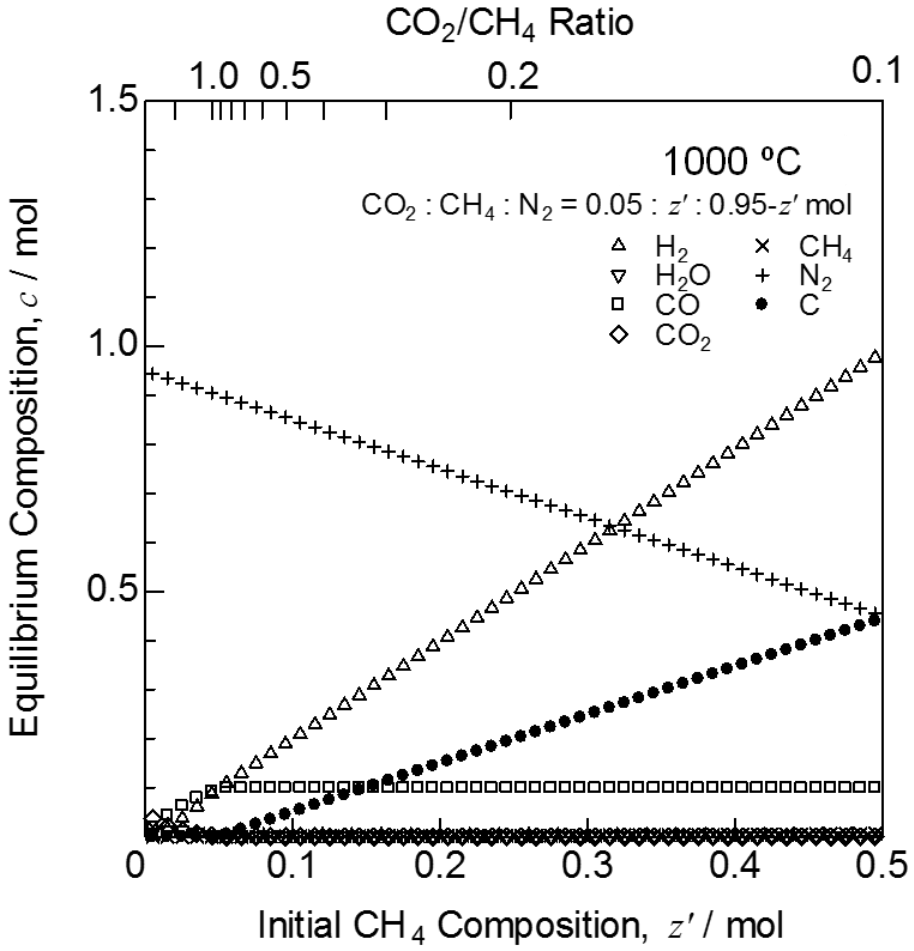


**Figure 2.6. Thermodynamic equilibrium compositions in $CO_2$–$CH_4$–$N_2$ mixture ($CO_2$ : $CH_4$ : $N_2$ = 0.05 : $z$' : 0.95-$z$') at 1000 ºC.**

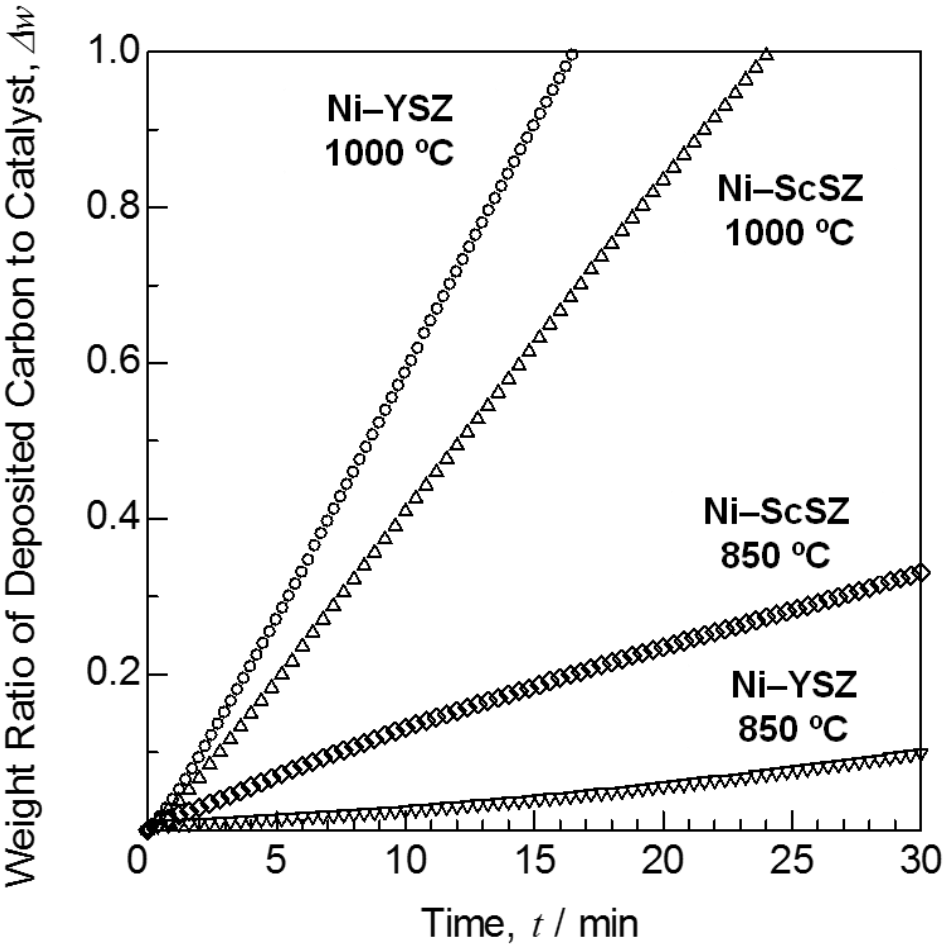


**Figure 2.7. Time courses of weight ratio of deposited carbon to catalyst with a supply of dry methane for the Ni–YSZ and Ni–ScSZ powders at 850 and 1000 °C.**

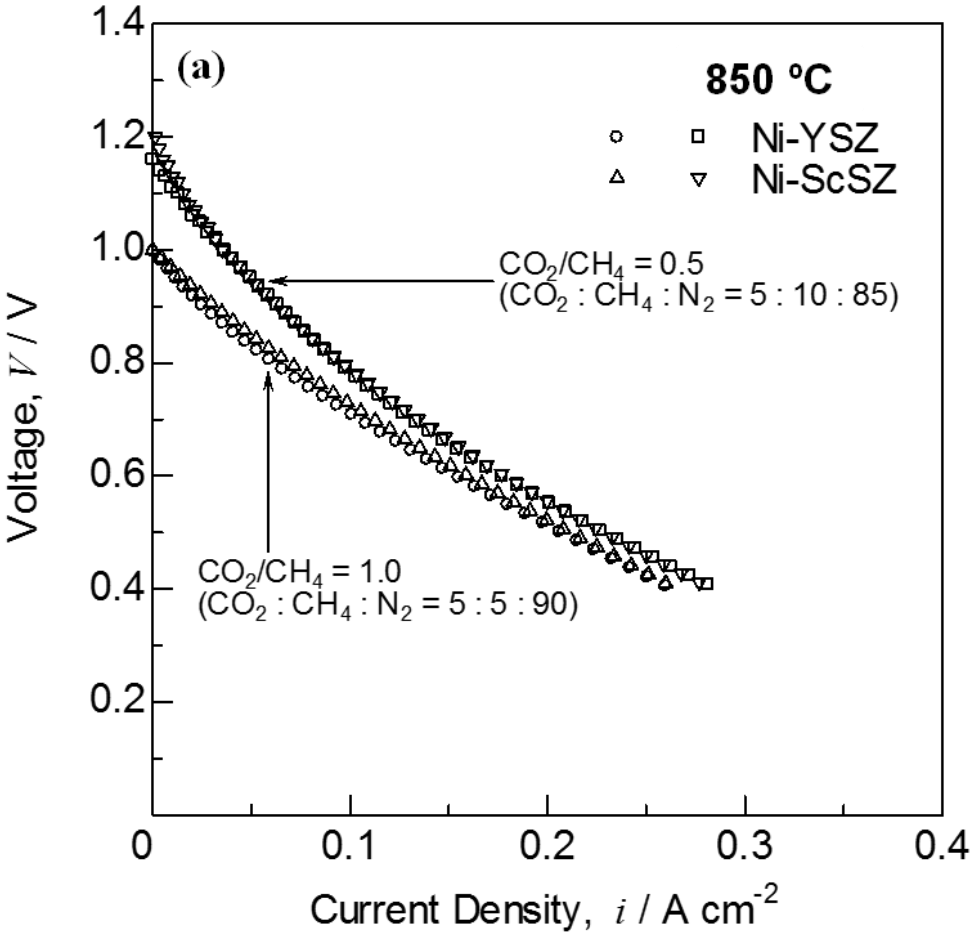


**Figure 2.8. Current-voltage characteristics with a supply of $CO_2$–$CH_4$–$N_2$ mixture ($CO_2$ : $CH_4$ : $N_2$ = 5 : *z* : 95-*z*) to the Ni–YSZ and Ni-ScSZ anodes at (a) 850 °C.**

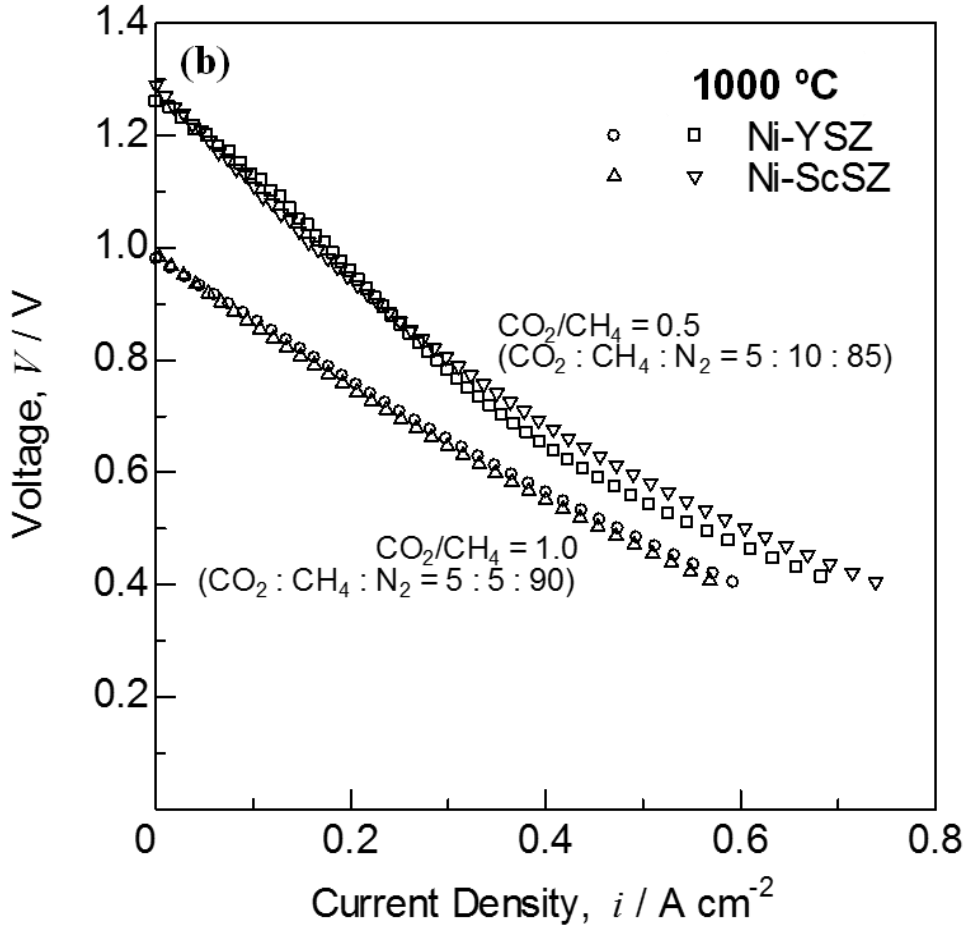


**Figure 2.8. Current-voltage characteristics with a supply of $CO_2$-$CH_4$-$N_2$ mixture ($CO_2$ : $CH_4$ : $N_2$ = 5 : *z* : 95-*z*) to the Ni-YSZ and Ni-ScSZ anodes at (b) 1000 °C.**

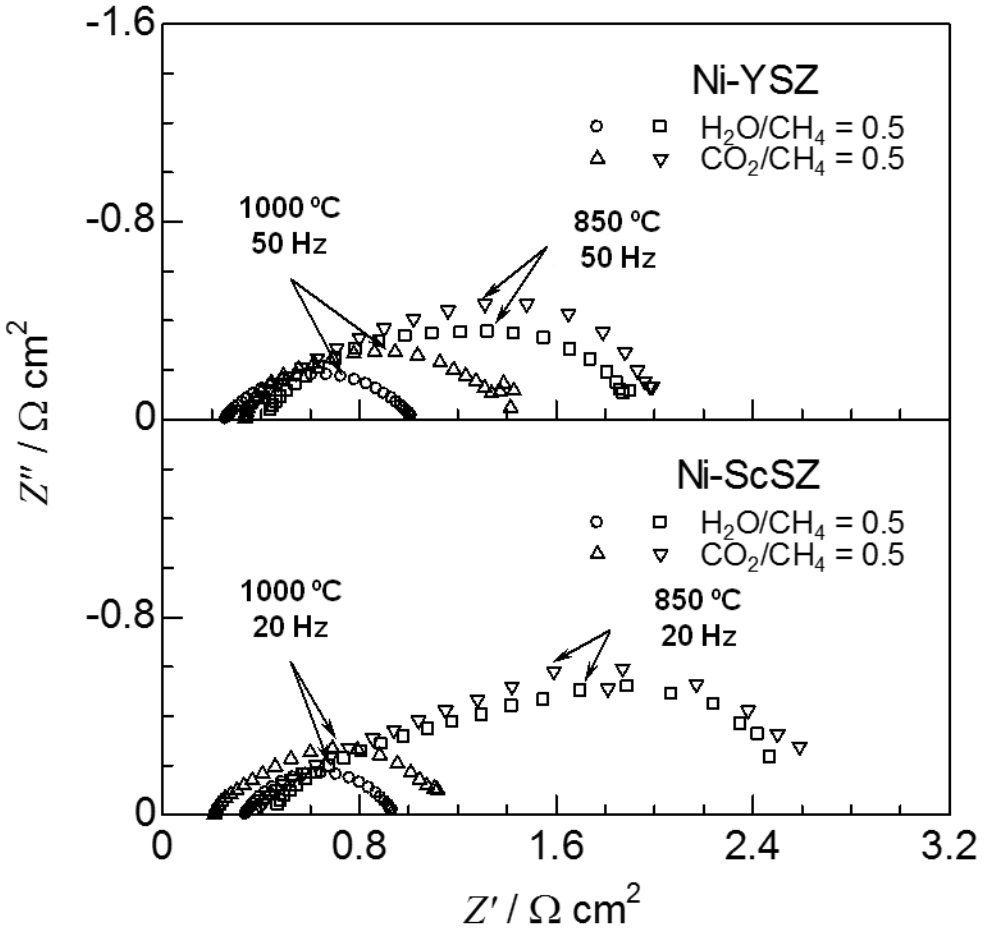


**Figure 2.9. Impedance spectra with a supply of $H_2O$ or $CO_2$–$CH_4$–$N_2$ mixture ($H_2O$ or $CO_2$ : $CH_4$ : $N_2$ = 5 : 10 : 85) to the Ni-YSZ and Ni-ScSZ anodes at 850 and 1000 ºC.**

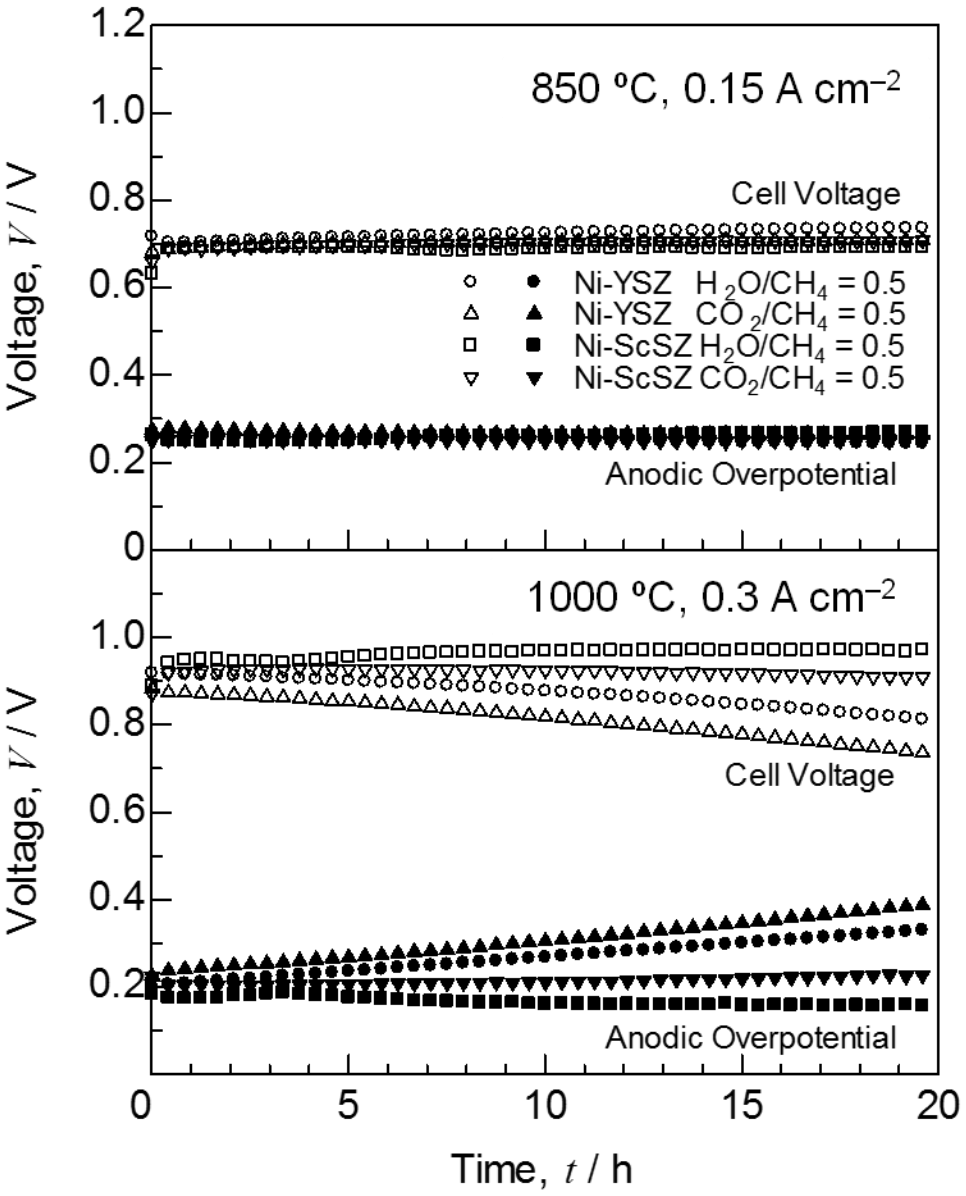


**Figure 2.10. Time courses of cell voltage and anodic overpotential with a supply of $H_2O$ or $CO_2$–$CH_4$–$N_2$ mixture ($H_2O$ or $CO_2$ : $CH_4$ : $N_2$ = 5 : 10 : 85) to the Ni-YSZ and Ni-ScSZ anodes at 850 and 1000 ºC.**

**Table 2.1. Initial polarization resistances of the Ni–YSZ and Ni–ScSZ anodes and increasing rates of anodic overpotential for initial 20 h with supplies of $H_2O/CH_4$ = 0.5 and $CO_2/CH_4$ = 0.5 at 850 and 1000 °C.**

| Temperature | Anode | Fuel | Initial polarization resistance of anode ($\Omega\ cm^2$) | Increasing rate of anodic overpotential ($mV\ h^{-1}$) |
|---|---|---|---|---|
| 850 °C | Ni-YSZ | $H_2O/CH_4 = 0.5$ | 1.5 | −0.9 |
| | | $CO_2/CH_4 = 0.5$ | 1.7 | −0.5 |
| | Ni-ScSZ | $H_2O/CH_4 = 0.5$ | 2.0 | 0.3 |
| | | $CO_2/CH_4 = 0.5$ | 2.2 | 0.1 |
| 1000 °C | Ni-YSZ | $H_2O/CH_4 = 0.5$ | 0.75 | 6.5 |
| | | $CO_2/CH_4 = 0.5$ | 1.1 | 8.3 |
| | Ni-ScSZ | $H_2O/CH_4 = 0.5$ | 0.60 | −1.2 |
| | | $CO_2/CH_4 = 0.5$ | 0.91 | 0.3 |

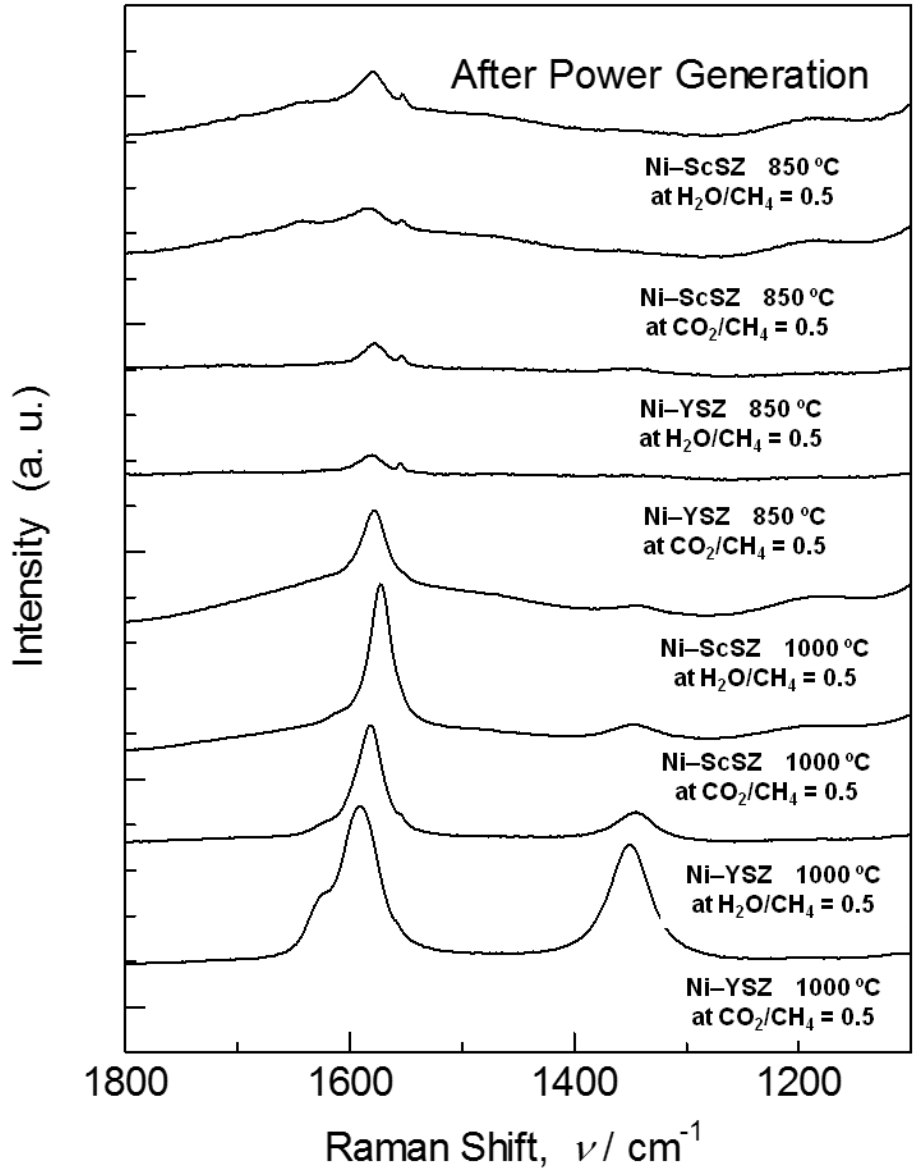


**Figure 2.11. Raman spectra for the Ni–YSZ and Ni–ScSZ anodes after power generation with a supply of $H_2O$ or $CO_2$–$CH_4$–$N_2$ mixture ($H_2O$ or $CO_2$ : $CH_4$ : $N_2$ = 5 : 10 : 85) at 850 and 1000 °C.**

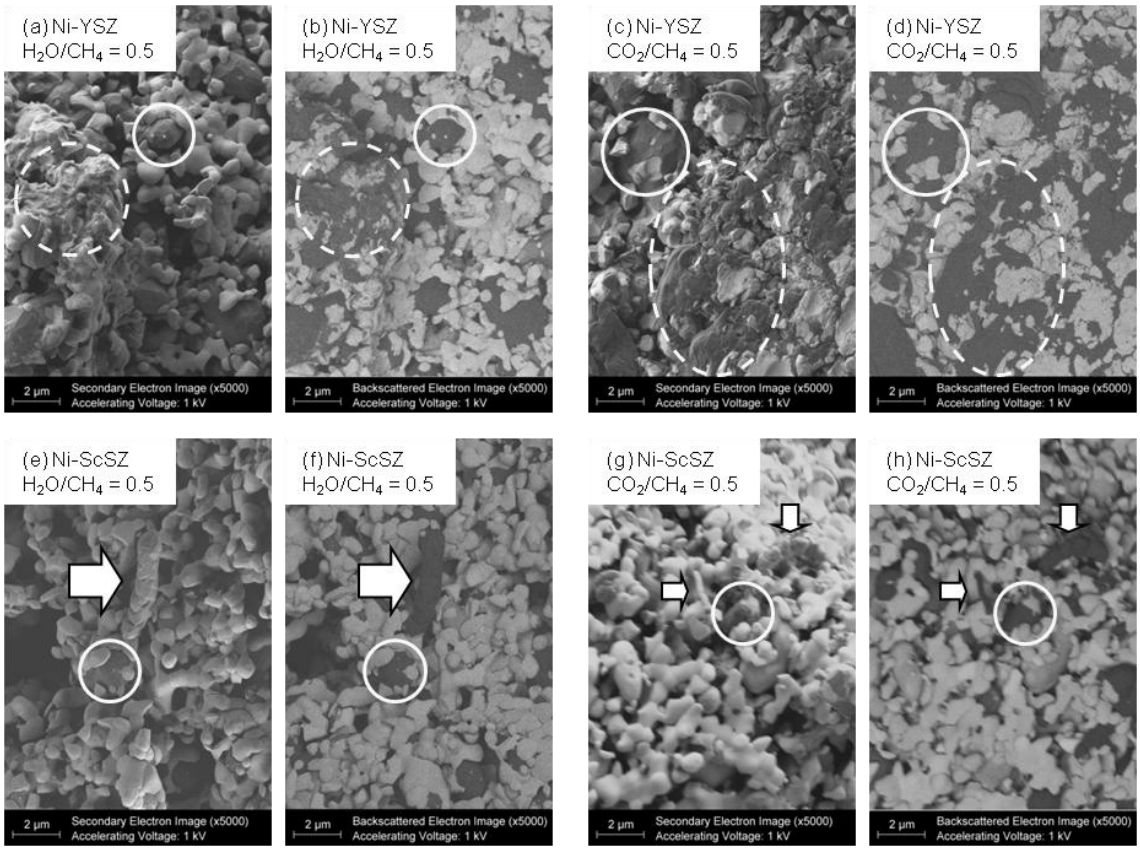


**Figure 2.12. Scanning electron microscopic images for the (a)-(d) Ni–YSZ and (e)-(h) Ni–ScSZ anodes after power generation. (a), (b), (e), (f) are at $H_2O/CH_4$ = 0.5 and (c), (d), (g), (h) are at $CO_2/CH_4$ = 0.5 at 1000 ºC. The photos of (a), (c), (e), (g) are secondary electron images, and those of (b), (d), (f), (h) are backscattered electron images.**

# Chapter 3

# Effect of Carbon Deposition by Carbon Monoxide Disproportionation on Electrochemical Characteristics at Low Temperature Operation for Solid Oxide Fuel Cells

## 3.1 Introduction

Hydrocarbon fuels are supplied in internal reforming for SOFCs as mentioned in chapters 1 and 2. Solid carbon is expected to be deposited by cracking reaction of methane fuels at low steam/carbon (S/C) ratios, which causes the deterioration of the anode performance due to deactivation of nickel catalyst and inhibition of fuel diffusion. The cracking reaction of hydrocarbon tends to proceed at high temperatures in thermodynamic equilibrium [1]. On the other hand, we should also pay attention to the carbon deposition by disproportionation reaction of carbon monoxide at low temperatures [2, 3]. The carbon deposition was actually confirmed with a supply of CO-rich gas for Ni–Fe and $Ni/SiO_2$ catalysts at 400–650 ºC [3-7]. It was reported that carbon dioxide reforming of methane is possible to cause the carbon deposition at low temperatures because of high CO concentration in reformate gas [8]. Under SOFC operation, the anodic overpotential increased with a rise in CO concentration in $H_2$–CO mixture at low temperatures [9-11]. However, water is generally contained in reformate gas, syngas, biogas and so on. The reaction system becomes complicated for the fuels containing water due to the occurrence of water gas shift reaction. The effects of the carbon deposition by CO disproportionation on the electrochemical characteristics are insufficient to be investigated under SOFC operation.

In this chapter, power generation tests were conducted at relatively low

temperature (650 ºC) as a function of $H_2$/CO ratios in $H_2$–CO–$H_2O$ and $H_2$–CO–$CO_2$ mixtures to investigate the influences of CO disproportionation and water gas shift reactions on electrochemical characteristics. Electrolyte- and anode-supported cells were used to evaluate the effect of the anode thickness. The power generation tests were also conducted for a low S/C ratio of methane at 800 ºC. The anodes after power generation were observed with field emission-scanning electron microscopy (FE–SEM) and Raman spectroscopy to compare the crystallinity, morphology and distribution of deposited carbon by CO disproportionation and methane cracking.

### 3.2 Experimental

Two types of electrolyte- and anode-supported cells were used in this study. Electrolyte, anode and cathode were $(Y_2O_3)_{0.08}$–$(ZrO_2)_{0.92}$ (YSZ), Ni–YSZ and $(La_{0.6}Sr_{0.4})(Co_{0.2}Fe_{0.8})O_3$ (LSCF), respectively. For the electrolyte-supported cells, the Ni–YSZ slurry was printed on a side of YSZ disk (thickness: 200 μm, diameter: 20 mm), and the $Ce_{0.8}Sm_{0.2}O_{1.9}$ (SDC) slurry was painted on the opposite side of the YSZ disk to prevent the reaction between the YSZ electrolyte and the LSCF cathode. The Ni–YSZ and SDC layers were co-sintered at 1300 ºC for 5 h in air. Then, the LSCF slurry was printed on SDC barrier layer, and was calcined at 900 ºC for 5 h in air. The thickness and diameter of electrodes were 30 μm and 6 mm, respectively. For the anode-supported cells, the YSZ electrolyte and $Ce_{0.8}Y_{0.2}O_{1.9}$ (YDC) barrier layers (thickness: 10 μm) were formed on Ni–YSZ anode substrate (thickness: 500 μm, diameter: 20 mm), and were co-sintered at 1300 ºC for 5 h in air. Then, the LSCF cathode (thickness: 30 μm, diameter: 17 mm) was calcined on YDC barrier layer at 900 ºC for 5 h in air.

In power generation tests, the mixtures of $H_2$ : CO : $H_2O$ (or $CO_2$) : $N_2$ = 25-$x$ : $x$ :

*y* : 75-*y* (*x* = *y* ) and pure $O_2$ were supplied to anode and cathode at 650 ºC, respectively. The total gas flow rate was 100 mL $min^{-1}$ in every condition. The water or carbon dioxide was supplied to define an oxygen partial pressure in the anode chamber. The changes in the species ($H_2O$, $CO_2$) were to investigate the effects of carbon deposition and water gas shift reaction. Current-voltage (*I*–*V*) characteristics were evaluated with potentiostat/galvanostat (Solartron Analytical 1470E). The ac impedance was measured under open circuit voltage (OCV) in the frequency range from 100 kHz to 0.1 Hz with an impedance analyzer (Solartron Analytical 1455A) at the anode-reference electrode and the anode-cathode for the electrolyte- and anode-supported cells, respectively. The compositions of exhaust gases from the anode chamber were analyzed with thermal conductivity detector (TCD) in micro gas chromatography (Valian 490-GC; $H_2$, $N_2$, $CH_4$, CO : Molecular Sieve 5A column $CO_2$ : Porapak U column) for the anode-supported cells. The power generation tests were also conducted in the mixture of $H_2O$ : $CH_4$ : $N_2$ = 1 : 10 : 89 at 800 ºC. The durability was evaluated for 20 h in the mixtures of $CO_2$ : CO : $N_2$ = 5 : 25 : 70 at 650 ºC and $H_2O$ : $CH_4$ : $N_2$ = 1 : 10 : 89 at 800 ºC. The anodes after the durability tests were observed with FE-SEM (Carl Zeiss NVision40) and Raman spectroscope (Horiba Jobin Yvon LabRAM HR-800). An accelerating voltage of FE-SEM was 2 kV to obtain the secondary electron and backscattered electron images. Raman spectra were measured in air with the use of a 514.5 nm $Ar^+$ laser. Equilibrium compositions were calculated by HSC Chemistry 5.11 (Outokumpu).

### 3.3 Results and Discussion

Figure 3.1 shows the temperature dependence of thermodynamic equilibrium compositions in (a) $CO_2$ : CO : $N_2$ = 0.05 : 0.25 : 0.70 mol and (b) $H_2O$ : $CH_4$ : $N_2$ =

0.01 : 0.10 : 0.89 mol. In $CO–CO_2$ mixture, carbon can be deposited by disproportionation of carbon monoxide called as the Boudouard reaction.

$$2CO \rightarrow CO_2 + C \quad (3–1)$$

This reaction tends to proceed at low temperatures as shown in Fig. 3.1 (a). Carbon will not be deposited above 900 ºC in equilibrium via this reaction. On the other hand, carbon is deposited by methane cracking at low S/C ratios from methane fuel.

$$CH_4 \rightarrow 2H_2 + C \quad (3–2)$$

This reaction tends to proceed at high temperatures as shown in Fig. 3.1 (b), whereas the Boudouard reaction favors low temperatures.

Next, the *I–V* and ac impedance characteristics were evaluated in $H_2 : CO : CO_2 : N_2 = 25\text{-}x : x : y : 75\text{-}y$ at 650 ºC. In the cases of $y = 5$ ($CO_2$), carbon can be deposited at $x > 17$ in equilibrium. Figure 3.2 shows the *I-V* characteristics for the (a) electrolyte- and (b) anode-supported cells with a supply of $H_2$-CO-$CO_2$ mixture at $y = 5$ and 650 ºC. The slopes of *I–V* curves became steep at low current density and $x > 17$ for the electrolyte-supported cells, which suggests the inhibition of electrode reaction by carbon deposition. The slopes of *I–V* curves, however, were almost the same at low current density in every condition for the anode-supported cells. The slopes at high current density became steep with an increase in *x*, because the diffusion resistance of carbon monoxide was larger than that of hydrogen in the thick anode layer for the anode-supported cells.

Figure 3.3 shows the ac impedance spectra with supplies of $H_2–CO–H_2O$ (or $CO_2$)–$N_2$ mixtures at OCV and 650 ºC. The impedances were measured at the anode-reference electrode and the anode-cathode for the (a) electrolyte- and (b) anode-supported cells, respectively. The impedance arcs were enlarged with increasing

CO concentration in every case for the electrolyte-supported cells. This result suggests that the rate of electrochemical oxidation of carbon monoxide is slower than that of hydrogen at low temperatures. It was reported that the increasing rate of the polarization resistance became small as a function of CO concentration at high temperatures, and the resistance in pure carbon monoxide was almost the same as that in pure hydrogen at 1000 ºC [15]. The polarization resistance in $H_2$–$H_2O$–CO–$N_2$ mixture was smaller than that in $H_2$–CO–$CO_2$–$N_2$ mixture at $x$ = 25 and 650 ºC for the electrolyte-supported cells. This result was caused by the promotion of water gas shift reaction and the decrease in the CO concentration.

. $$CO + H_2O \leftrightarrow H_2 + CO_2 \quad (3–3)$$

For the anode-supported cells, the impedance spectra were almost unchanged against CO concentration in all conditions as shown in Fig. 3.3(b). The carbon deposition did not lead to increase in the polarization resistance. This result agreed well with the similar slope of the *I*–*V* curves at low current density as shown in Fig. 3.2(b). Next, the compositions of anode exhaust gases at OCV and 62.5 mA $cm^{-2}$ were analyzed with micro gas chromatography to investigate whether the water gas shift reaction proceeded. Table 3.1 shows the results of gas chromatography analysis and equilibrium calculation at $y$ = 3 in $H_2$–CO–$H_2O$ mixture, $y$ = 5 in $H_2$–CO–$CO_2$ mixture and 650 ºC. The production of hydrogen and carbon dioxide are facilitated in equilibrium by forward reaction (3–3) with increasing CO concentration, $x$, in $H_2$–CO–$H_2O$ mixture. On the contrary, the formation of steam and carbon monoxide are promoted by reverse reaction (3–3) with decreasing $x$ in $H_2$–CO–$CO_2$ mixture. Furthermore, carbon monoxide decreases and carbon dioxide increases in the carbon deposition condition by the Boudouard reaction (3–1). Actually at OCV, the production

of hydrogen at $x$ = 25 in CO–$H_2O$ mixture and that of carbon monoxide at $x$ = 0 in $H_2$–$CO_2$ mixture confirmed the progress of water gas shift reaction. In addition, the Boudouard reaction also proceeded as evidenced by the increasing amount of carbon dioxide from the initial amount of 5 mL $min^{-1}$ at $x$ > 17 in $H_2$–CO–$CO_2$ mixture. The difference between the calculation and the experimental values at OCV increased with a rise in CO concentration. This result suggests that the rate of the Boudouard reaction was slower than that of water gas shift reaction at 650 ºC. Hydrogen and carbon monoxide are oxidized electrochemically under current loading.

$$H_2 + O^{2-} \rightarrow H_2O + 2e^- \quad (3–4)$$

$$CO + O^{2-} \rightarrow CO_2 + 2e^- \quad (3–5)$$

The decrease in the sum of hydrogen and carbon monoxide was approximately 1 mL $min^{-1}$ in all conditions under a current loading of 142 mA. This result agreed with the estimated consumption of 6.96 mL $min^{-1}$ $A^{-1}$ from Faraday's law by the reactions of (3–4) and (3–5). The $H_2$/CO ratio was almost unchanged experimentally with and without current loading in all conditions. Carbon monoxide was consumed by the electrochemical oxidation (3–5) and/or water gas shift reaction (3–3) at a low temperature of 650 ºC.

Next, the carbon deposition behavior was compared with methane cracking. Figure 3.4 shows the *I–V* characteristics and ac impedance spectra for the (a) electrolyte- and (b) anode-supported cells at 800 ºC with supplies of $H_2O$–$H_2$ and $H_2O$–$CH_4$ mixtures. The impedance for the electrolyte-supported cell in Fig. 3.4(a) was measured between the anode and reference electrode as well as in Fig. 3.3(a). Carbon is expected to be deposited at S/C < 1 and 800 ºC in equilibrium. The OCV value in $H_2O$–$CH_4$ mixture was larger than that in $H_2O$–$H_2$ mixture because of the decrease in

oxygen partial pressure in the carbon deposition condition. The slopes of *I–V* curves became steep at low current density arcs in $H_2O$–$CH_4$ mixture. The impedance arcs in $H_2O$–$CH_4$ mixture were larger than that in $H_2O$–$H_2$ mixture for both of the cells. This result was different from no change of impedance spectra in $CO_2$–CO mixture for the anode-supported cells in Fig. 3.3(b). The slopes at high current density in $H_2O$–$CH_4$ mixture was steeper than that in $H_2O$–$H_2$ mixture for the anode-supported cells, which supposed the increase in diffusion resistance of methane as well as carbon dioxide in the thick anode layer.

Durability tests were conducted to investigate carbon deposition behavior precisely. Figure 3.5 shows the time courses of cell voltage for the (a) electrolyte- and (b) anode-supported cells with supplies of $CO_2$–CO mixture at 650 ºC and $H_2O$–$CH_4$ mixtures at 800 ºC. The cell voltage decreased rapidly for the initial 10–60 min in $H_2O$–$CH_4$ mixture for both cells, followed by the voltage gradual decrease. On the other hand, the voltage continuously decreased in $CO_2$–CO mixture. This result suggests that the rate of carbon deposition in $H_2O$–$CH_4$ mixture is different from that in $CO_2$–CO mixture.

The Ni–YSZ anodes after durability test were observed with FE–SEM and Raman spectroscopy. Figure 3.6 shows the backscattered electron images of the cross-section for the anode-supported cells after power generation for 20 h in (a) $CO_2$–CO mixture at 650 ºC and (b) $H_2O$–$CH_4$ mixture at 800 ºC. The black areas were ascribed to the deposited carbon, which was confirmed by an energy-dispersive X-ray spectrometer. Although a large amount of carbon was deposited near the anode surface after power generation in $CO_2$–CO mixture, less amount of carbon was observed near the interface between the anode and the electrolyte. This result suggests that the Boudouard reaction

(3–1) proceeds only near the anode surface. On the other hand, the large amount of deposited carbon was observed from the anode surface to the anode/electrolyte interface after power generation in $H_2O$–$CH_4$ mixture, which supported the methane cracking reaction (3–2) proceeded in the whole anode layer. These results also propose that the reaction rate of methane cracking at 800 ºC is slower than that of CO disproportionation at 650 ºC. Figure 3.7 shows the secondary electron images of the Ni–YSZ anodes near the surface after power generation for 20 h in (a) $CO_2$–CO mixture at 650 ºC and (b) $H_2O$–$CH_4$ mixture at 800 ºC. The deposited carbon as the coated layer on the nickel particles was observed after power generation in $CO_2$–CO mixture. However, the agglomerated cokes were deposited after power generation in $H_2O$–$CH_4$ mixture. The carbon with a similar morphology was observed after power generation at 1000 ºC and S/C = 0.5 in methane fuel. The morphologies of deposited carbon for the electrolyte-supported cells were almost the same as that for the anode-supported cells. As the anode layer was thinner for the electrolyte-supported cells, the deposited carbon was confirmed from the anode surface to the anode/electrolyte interface after power generation in $CO_2$–CO mixture. The polarization resistance of the anode became large in the carbon deposition conditions except in $CO_2$–CO mixture for the anode-supported cells, which had no deposited carbon in the vicinity of the anode/electrolyte interface. Therefore, the increase in polarization resistance strongly correlated with the carbon deposition near the anode/electrolyte interface.

Raman spectra were measured to investigate the local structure and distribution of deposited carbon. Figure 3.8 shows the mapping images and spectra for the Ni–YSZ anodes of the anode-supported cells after power generation for 20 h in (a, c) $CO_2$–CO mixture at 650 ºC and (b, d) $H_2O$–$CH_4$ mixture at 800 ºC. The peaks at 1350 $cm^{-1}$

(D-band) and 1585 $cm^{-1}$ (G-band) are attributed to amorphous carbon and crystalline graphite, respectively. The mapping images for the intensities of D-band and G-band were taken at 5 μm intervals in the area of 20 μm in width × 400 μm in height. The stronger the peak intensity is the darker mapping images become in Fig. 3.8(a) and (b). While the peak intensity of G-band was strong near the anode surface, the intensity was weak in the vicinity of the anode/electrolyte interface after power generation in $CO_2$–CO mixture. This result agrees with the distribution of deposited carbon observed with FE–SEM as shown in Fig. 3.6(a). The strong peaks of G-band were observed from the anode surface to *ca.* 200 μm in depth, which resulted from the occurrence of CO disproportionation during the durability test for 20 h in this region. The peak intensity of D-band was weak in the whole anode layer. The carbon was attributed to crystalline graphite and deposited as a coating layer on the nickel particles as shown in Fig. 3.7 (a). On the other hand, the peak intensities of D-band and G-band were unchanged throughout the anode layer after power generation in $H_2O$–$CH_4$ mixture. This result also agrees with the wide distribution of deposited carbon observed with FE–SEM as shown in Fig. 3.6(b). The intensity ratio of D-band/G-band after power generation in $H_2O$–$CH_4$ mixture was larger than that in $CO_2$–CO mixture. The agglomerated cokes as shown in Fig. 3.7(b) contained the large amount of amorphous carbon. The distribution in deposited carbon as shown in Fig. 3.8 suggests that the rate of methane cracking at 800 ºC is slower than that of CO disproportionation at 650 ºC. The deposited carbon near the anode/electrolyte interface affected strongly the increase in the polarization resistance.

### 3.4 Conclusion

In this chapter, the cell performance and ac impedance were evaluated at 650 ºC and as a function of $H_2$/CO ratios in $H_2$–CO–$H_2O$ and $H_2$–CO–$CO_2$ mixtures, and carbon deposition behavior by carbon monoxide disproportionation and methane cracking was compared. The polarization resistance was enlarged with increasing CO concentration for the electrolyte-supported cells. This result suggests that electrochemical oxidation of carbon monoxide is more difficult than that of hydrogen at low temperatures. The polarization resistance in $H_2$–CO–$H_2O$ mixture was smaller than that in $H_2$–CO–$CO_2$ mixture because of the decrease in CO concentration by water gas shift reaction. While the polarization resistance was unchanged in CO–$CO_2$ mixture for the anode-supported cells, the resistance increased in $H_2O$-$CH_4$ mixture for both of the cells in the carbon deposition condition. The graphite was deposited as coating layer on the nickel particles only near the anode surface facing to the flowing gas after durability test in CO–$CO_2$ mixture for the anode-supported cells. On the other hand, a large amount of agglomerated amorphous carbon was deposited from the anode surface to the interface between the anode and the electrolyte after power generation in $H_2O$–$CH_4$ mixture. These results suggest that the rate of methane cracking at 800 ºC was slower than that of CO disproportionation at 650ºC. It was concluded that the increase in polarization resistance was strongly correlated with the carbon deposition near the anode/electrolyte interface.

### References

1. K. Ke, A. Gunji, H. Mori, S. Tsuchida, H. Takahashi, K. Ukai, Y. Mizutani, H. Sumi, M. Yokoyama, K. Waki, *Solid State Ionics*, **177** 541 (2006).

2. M. Audier, M. Coulon, L. Bonnetain, *Carbon*, **17** 391 (1979).

3. J. Guinot, M. Audier, M. Coulon, L. Bonnetain, *Carbon*, **19** 95 (1981).

4. E. G. M. Kuijpers, A. J. H.M. Kock, M. W. C. M. Nieuwesteeg, J. W. Geus, *J. Catal.*, **95** 13 (1985).

5. C. Mirodatos, H. Praliaud, M. Primet, *J. Catal.*, **107** 275 (1987).

6. P. E. Nolan, D. C. Lynch, A. H. Cutler, *Carbon*, **32** 477 (1994).

7. J. Jiao, P. E. Nolan, S. Seraphin, A. H. Cutler, D. C. Lynch, *J. Electrochem. Soc.*, **143** 932 (1996).

8. K. Tomishige, Y-G. Chen, K. Fujimoto, *J. Catal.*, **181** 91 (1999).

9. K. Sasaki, Y. Hori, R. Kikuchi, K. Eguchi, A. Ueno, H. Takeuchi, M. Aizawa, K. Tsujimoto, H. Tajiri, H. Nishikawa, Y. Uchida, *J. Electrochem. Soc.*, **149** A227 (2002).

10. A. Weber, B. Sauer, A. C. Müller, D. Herbstritt, E. Ivers-Tiffee, *Solid State Ionics*, **152-153** 543 (2002).

11. V. Alzate-Restrepo, J. M. Hill, *J. Power Sources*, **195** 1344 (2010).

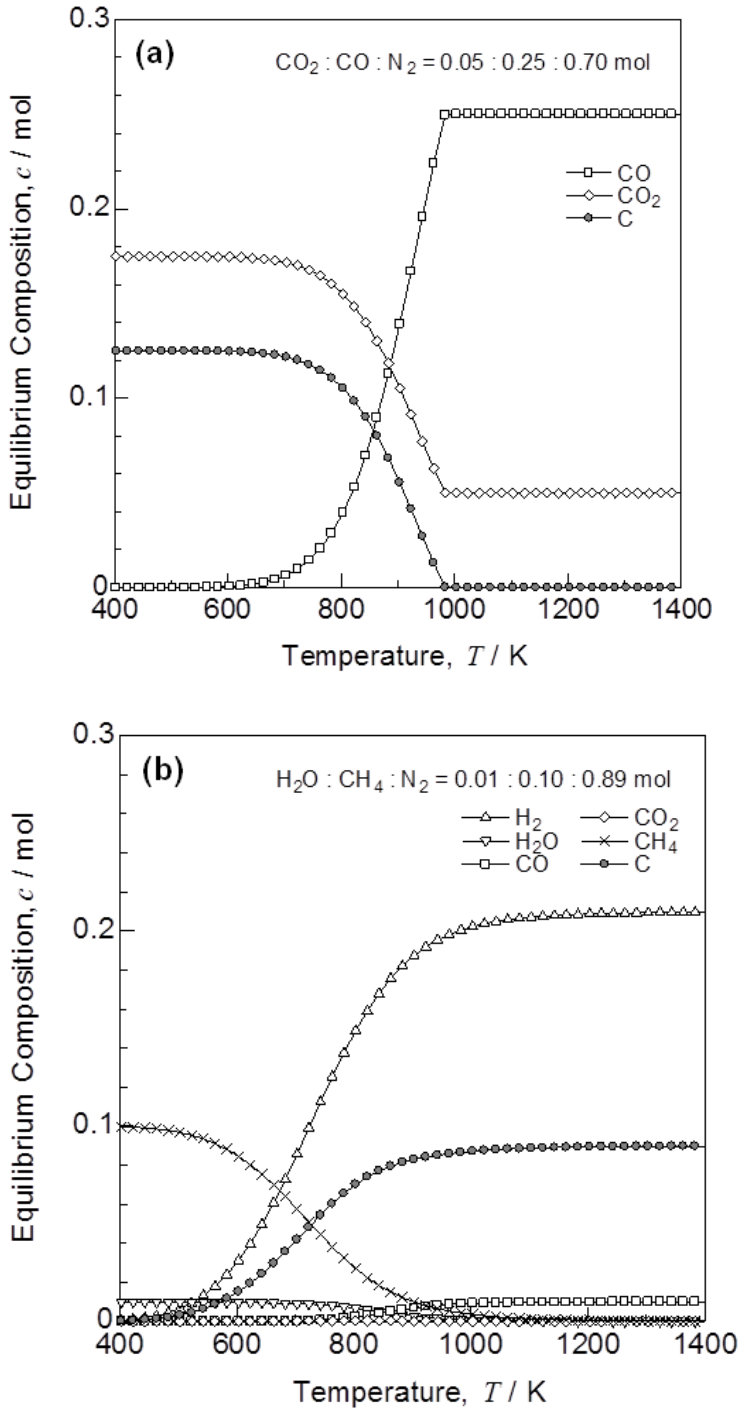


**Figure 3.1. Thermodynamic equilibrium compositions in (a) $CO_2$ : CO : $N_2$ = 0.05 : 0.25 : 0.70 and (b) $H_2O$ : $CH_4$ : $N_2$ = 0.01 : 0.10 : 0.89 mol.**

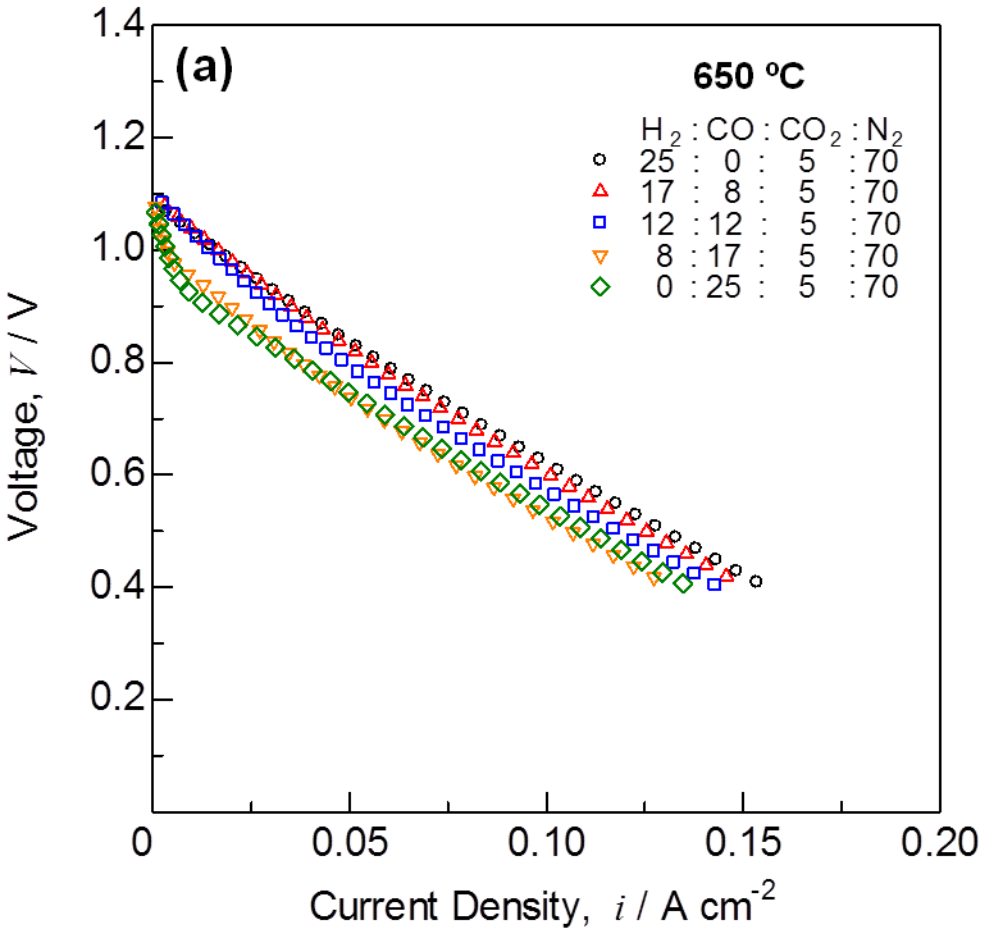


**Figure 3.2. Current-voltage characteristics for the (a) electrolyte-cells with a supply of $H_2$-CO-$CO_2$ mixture at 650 °C.**

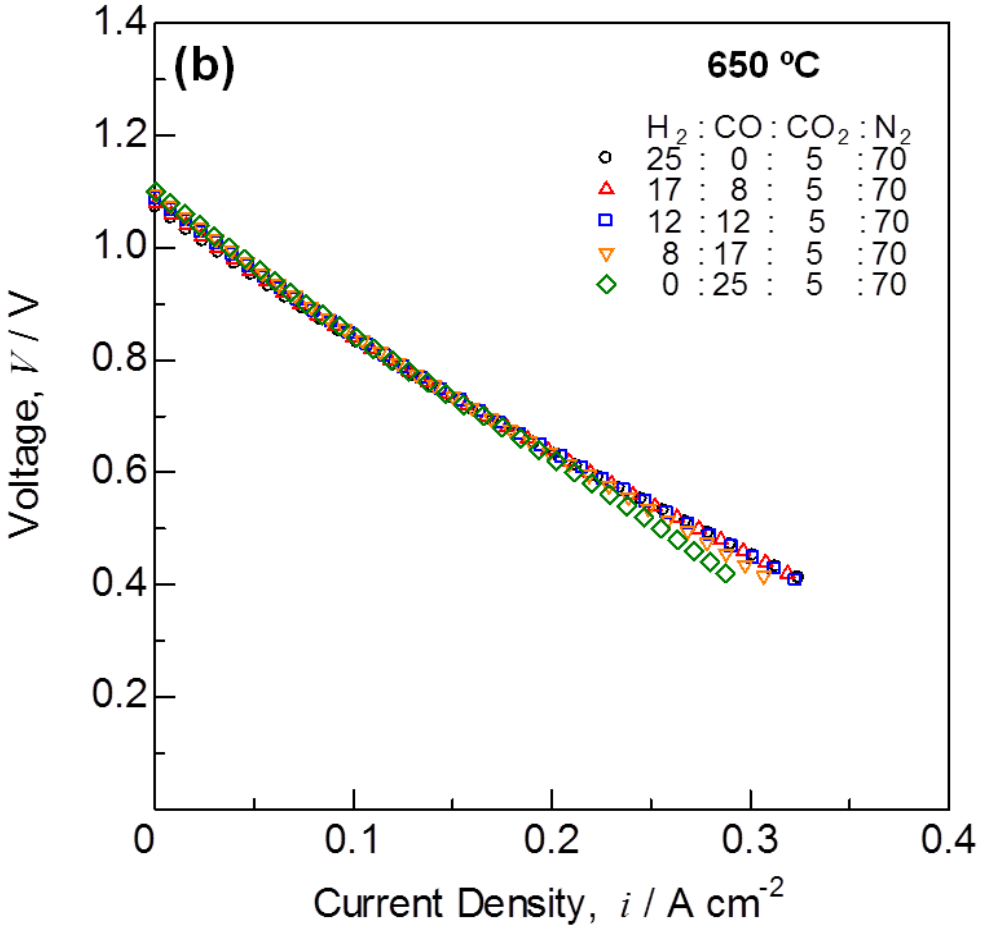


**Figure 3.2. Current-voltage characteristics for the (b) anode-supported cells with a supply of $H_2$-CO-$CO_2$ mixture at 650 ºC.**

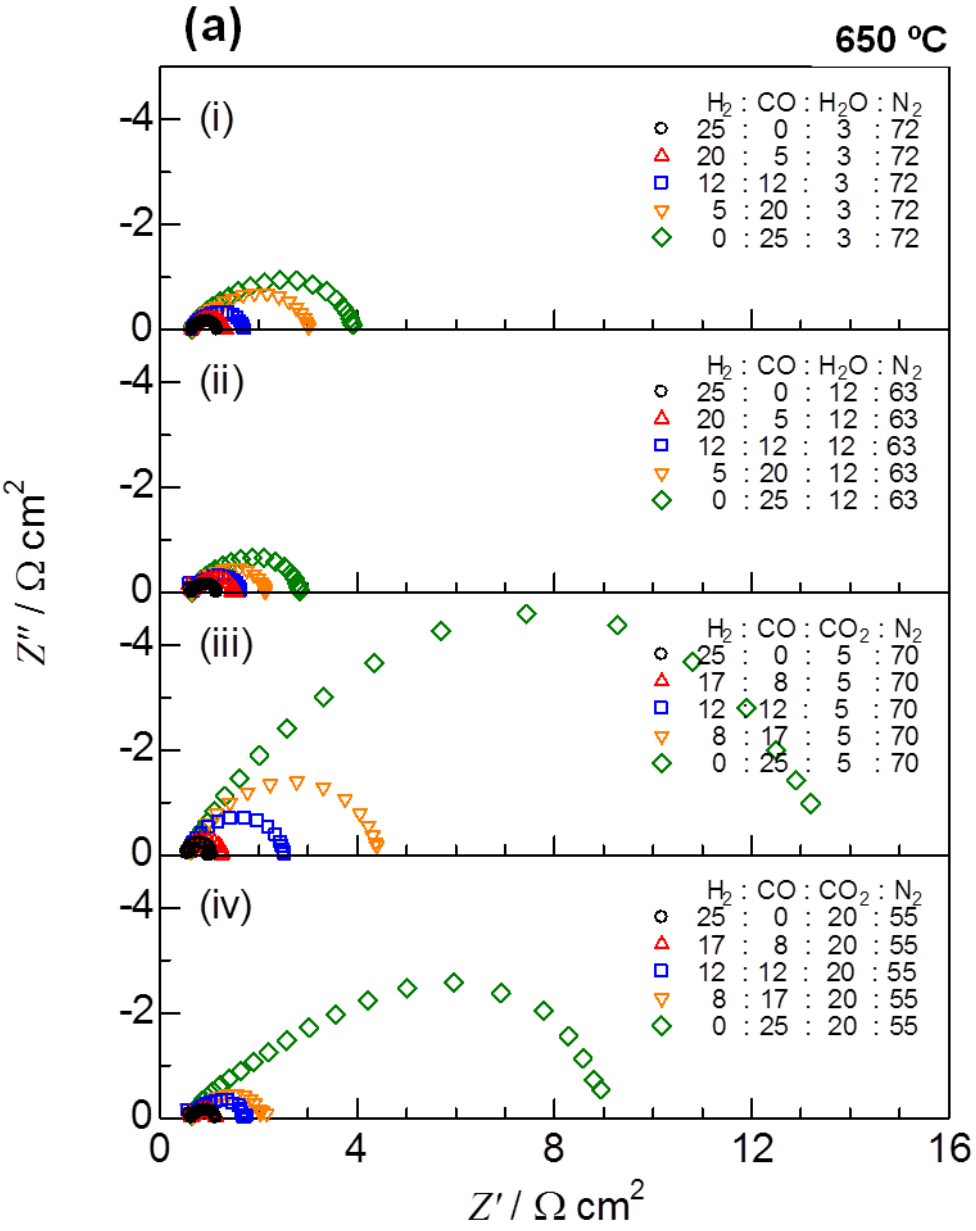


**Figure 3.3. AC impedance spectra for the (a) electrolyte-cells with a supply of $H_2$-CO-$H_2O$(or $CO_2$) mixture at 650 °C. The impedances were measured between the anode, and reference electrode for the electrolyte-supported cell and between the anode and cathode for anode-supported cell.**

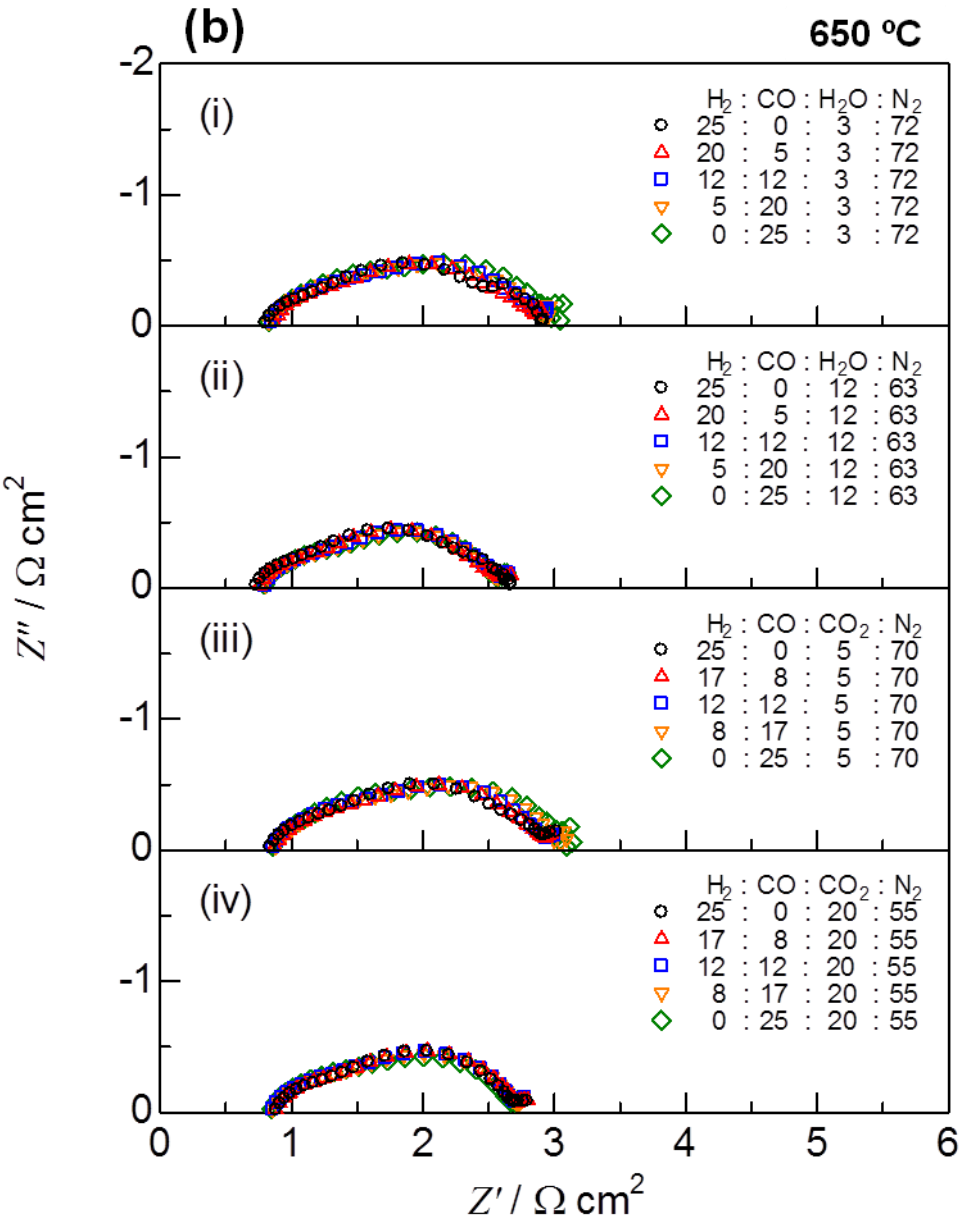


**Figure 3.3. AC impedance spectra for the (b) anode-supported cells with a supply of $H_2$-CO-$H_2O$(or $CO_2$) mixture at 650 ºC. The impedances were measured between the anode, and reference electrode for the electrolyte-supported cell and between the anode and cathode for anode-supported cell.**

**Table 3.1 Gas production of $H_2$, CO and $CO_2$ (mL $min^{-1}$) and $H_2$/CO ratios in anode exhaust gas for the anode-supported cells at 0, 142 mA and 650 ºC with supplies of $H_2$ : CO : $H_2O$ or $CO_2$ : $N_2$ = 25-*x* : *x* : *y* : 75-*y*.**

| $H_2$–CO–$H_2O$ mixture ($y$ = 3) | | | | | | | $H_2$–CO–$CO_2$ mixture ($y$ = 5) | | | | | | |
|---|---|---|---|---|---|---|---|---|---|---|---|---|---|
| *x* | | $H_2$ | $H_2O$ | CO | $CO_2$ | $H_2$/CO | *x* | | $H_2$ | $H_2O$ | CO | $CO_2$ | $H_2$/CO |
| 0 | Calc. | 25.0 | 3.0 | 0.0 | 0.0 | ∞ | 0 | Calc. | 20.5 | 4.0 | 3.4 | 1.3 | 6.02 |
| | 0 mA | 22.3 | – | 0.0 | 0.0 | ∞ | | 0 mA | 16.4 | – | 2.9 | 2.1 | 4.21 |
| | 142 mA | 21.3 | – | 0.0 | 0.0 | ∞ | | 142 mA | 15.7 | – | 2.4 | 2.5 | 4.61 |
| 5.0 | Calc. | 19.7 | 2.5 | 3.7 | 0.9 | 5.32 | 8.3 | Calc. | 13.7 | 2.2 | 9.6 | 3.2 | 1.43 |
| | 0 mA | 18.2 | – | 4.5 | 1.0 | 4.04 | | 0 mA | 11.9 | – | 9.1 | 4.3 | 1.18 |
| | 142 mA | 17.6 | – | 4.4 | 1.2 | 4.00 | | 142 mA | 11.4 | – | 8.4 | 5.1 | 1.21 |
| 12.5 | Calc. | 12.9 | 1.8 | 8.8 | 2.5 | 1.47 | 12.5 | Calc. | 10.1 | 1.9 | 11.8 | 4.4 | 0.86 |
| | 0 mA | 12.9 | – | 10.4 | 2.1 | 1.24 | | 0 mA | 9.2 | – | 12.2 | 5.2 | 0.70 |
| | 142 mA | 12.2 | – | 10.1 | 2.9 | 1.21 | | 142 mA | 8.8 | – | 11.4 | 6.2 | 0.71 |
| 20.0 | Calc. | 6.5 | 1.3 | 12.2 | 4.8 | 0.53 | 16.7 | Calc. | 5.8 | 1.3 | 13.9 | 6.2 | 0.42 |
| | 0 mA | 7.5 | – | 16.7 | 2.7 | 0.45 | | 0 mA | 6.5 | – | 15.5 | 5.9 | 0.39 |
| | 142 mA | 6.8 | – | 16.4 | 3.8 | 0.41 | | 142 mA | 6.2 | – | 14.5 | 7.0 | 0.40 |
| 25.0 | Calc. | 2.4 | 0.6 | 14.2 | 6.6 | 0.17 | 25.0 | Calc. | 0.0 | 0.0 | 16.7 | 9.1 | 0.00 |
| | 0 mA | 3.5 | – | 21.2 | 2.8 | 0.17 | | 0 mA | 0.0 | – | 22.0 | 7.0 | 0.00 |
| | 142 mA | 2.4 | – | 20.8 | 4.2 | 0.12 | | 142 mA | 0.0 | – | 20.8 | 8.5 | 0.00 |

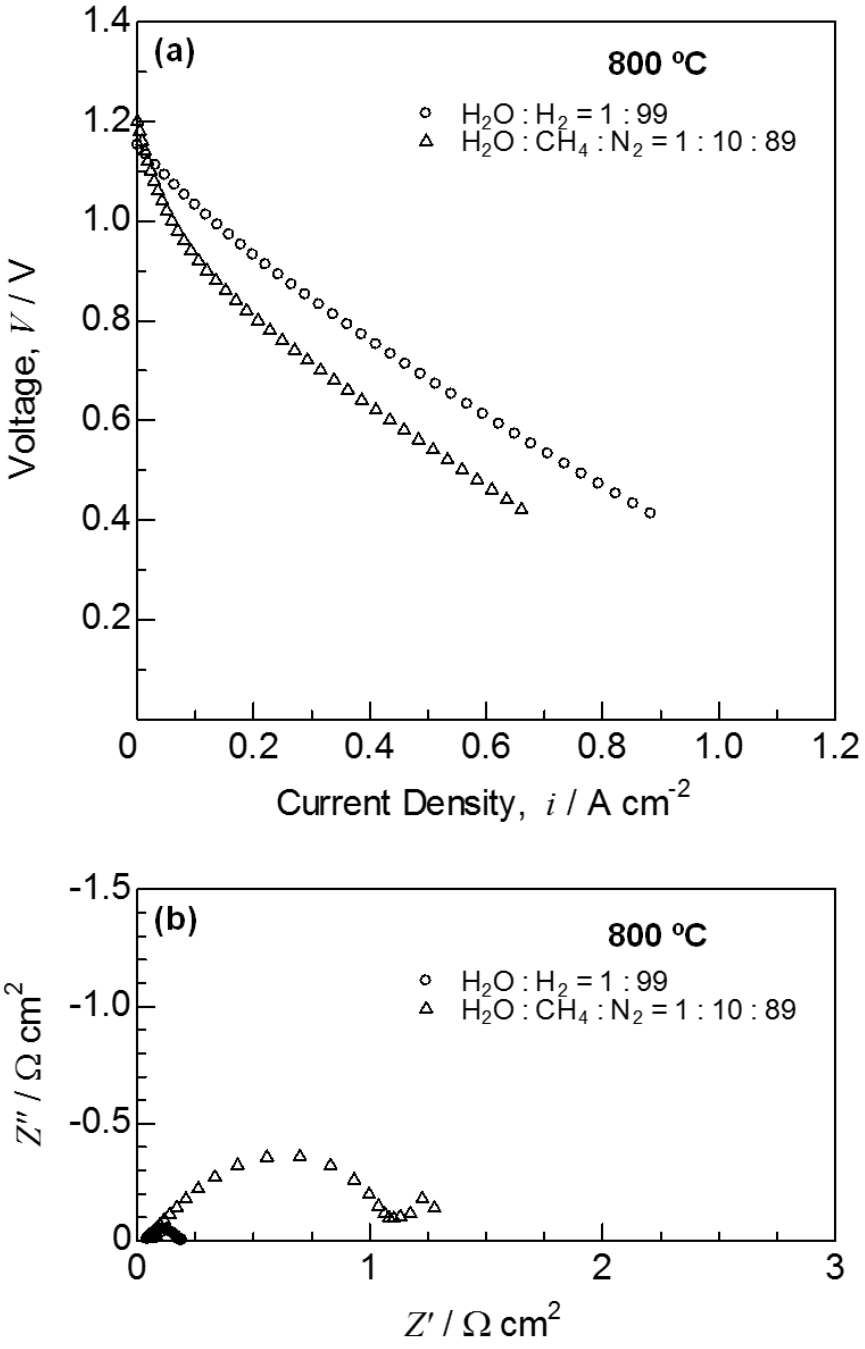


**Figure 3.4. (a) Current-voltage characteristics and (b) AC impedance spectra for the (a, b) electrolyte-cells with supplies of $H_2O$-$H_2$ and $H_2O$-$CH_4$ mixtures at 800°C. The impedances were measured between the anode and reference electrode for the electrolyte-supported cell, and between the anode and cathode for anode-supported cell.**

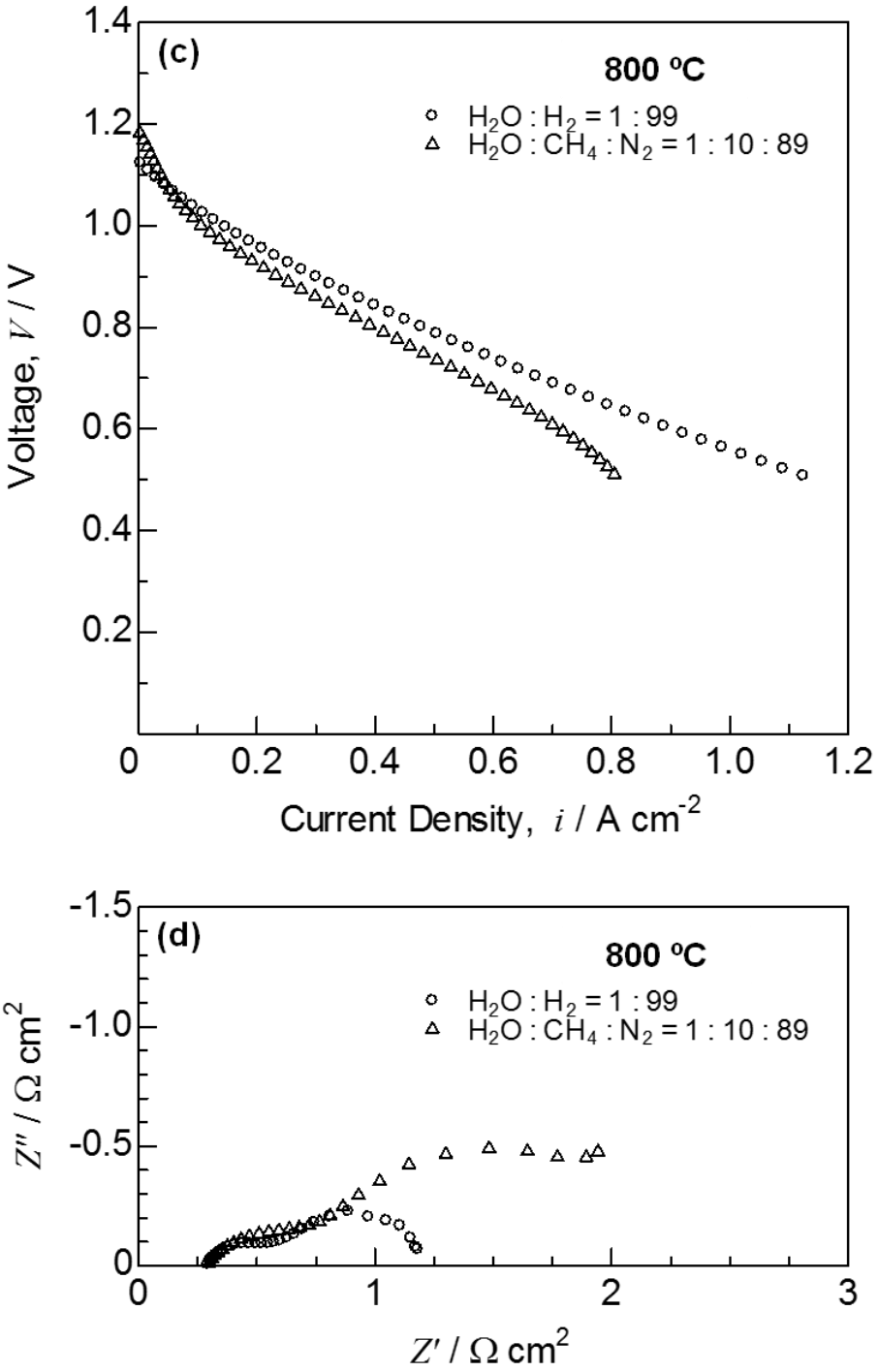


**Figure 3.4. (c) Current-voltage characteristics and (d) AC impedance spectra for the (c, d) anode-supported cells with supplies of $H_2O$-$H_2$ and $H_2O$-$CH_4$ mixtures at 800°C. The impedances were measured between the anode and reference electrode for the electrolyte-supported cell, and between the anode and cathode for anode-supported cell.**

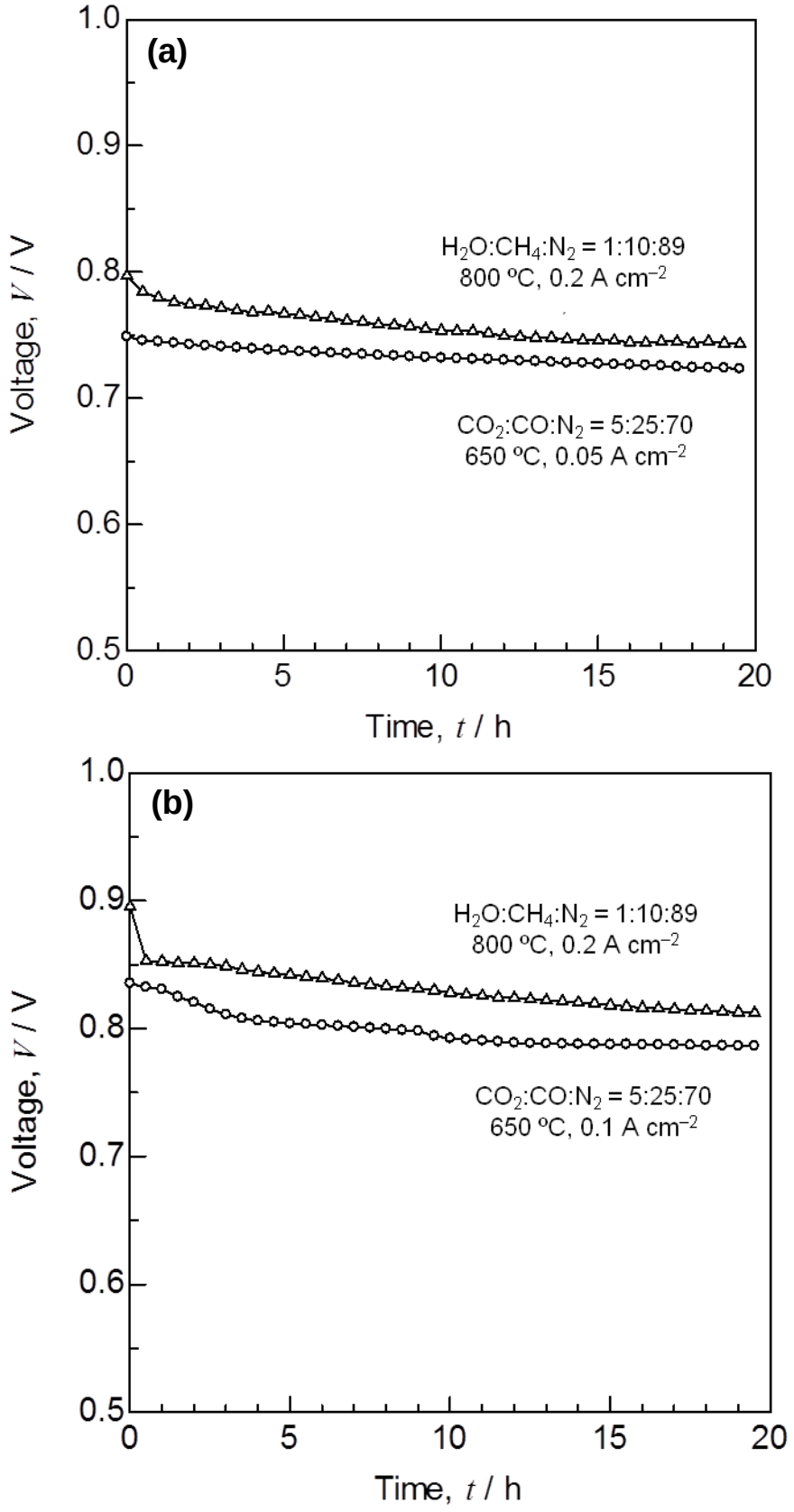


**Figure 3.5. Time courses of cell voltage for the (a) electrolyte- and (b) anode-supported cells with supplies of $CO_2$-CO mixture at 650 ºC and $H_2O$-$CH_4$ mixture at 800 ºC.**

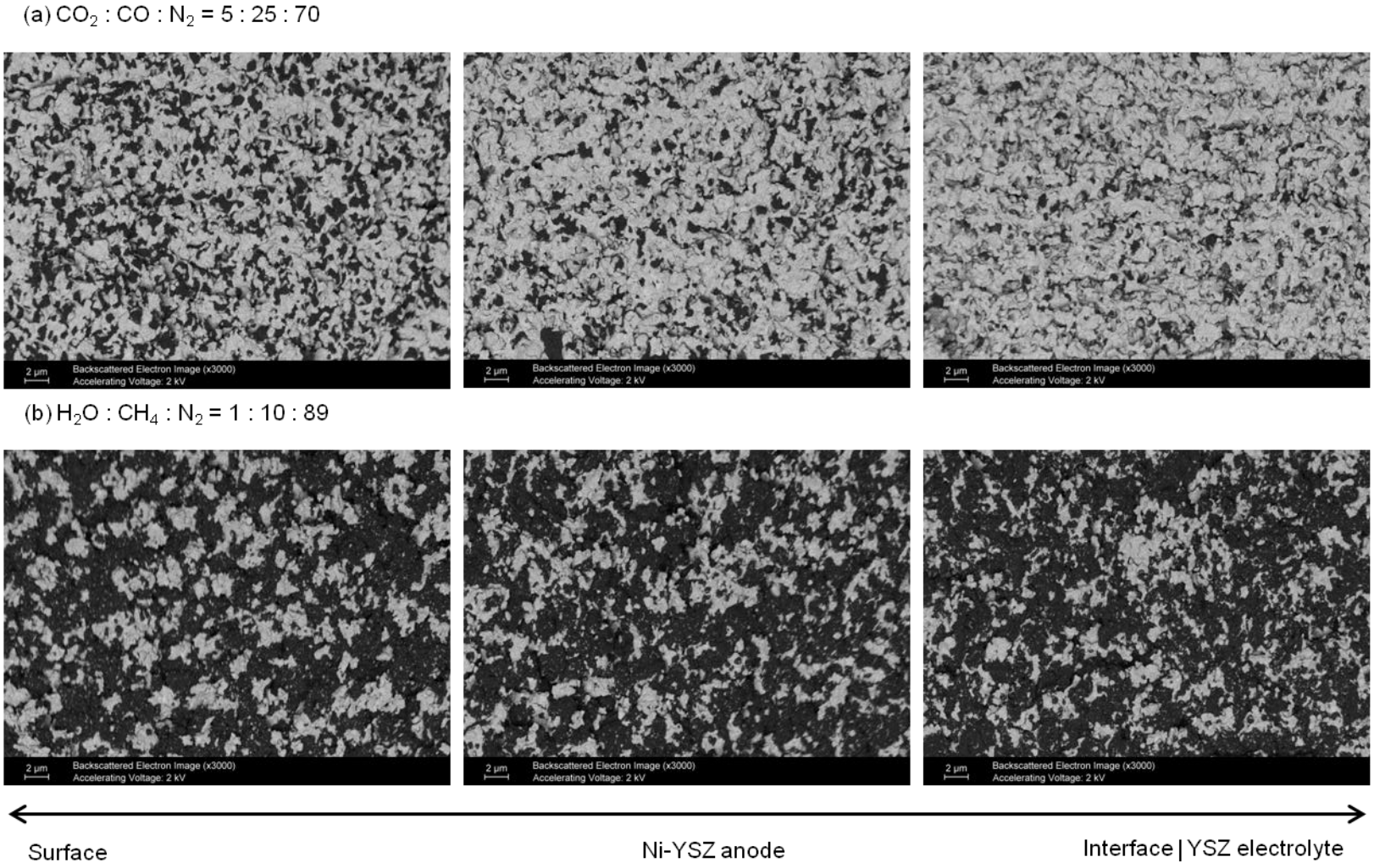


**Figure 3.6. Backscattered electron images for the Ni–YSZ anodes of the anode-supported cells after power generation for 20 h with supplies of (a) $CO_2$–CO mixture at 650 °C and (b) $H_2O$–$CH_4$ mixture at 800 °C.**

(a) $CO_2$ : CO : $N_2$ = 5 : 25 : 70

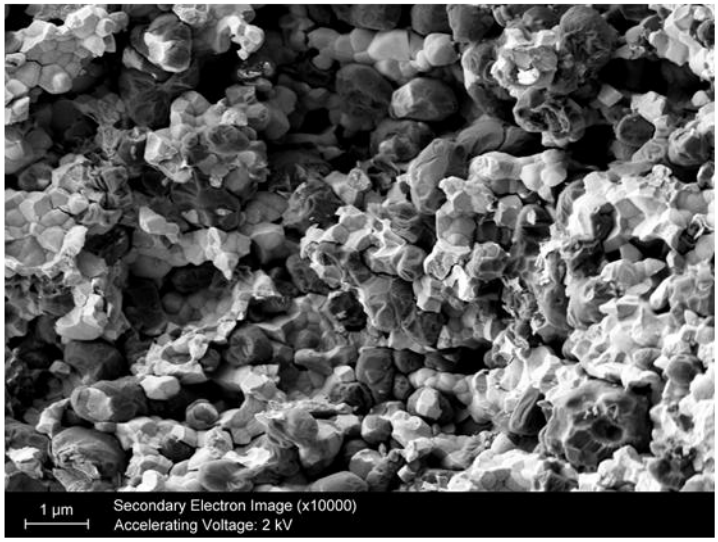


(b) $H_2O$ : $CH_4$ : $N_2$ = 1 : 10 : 89

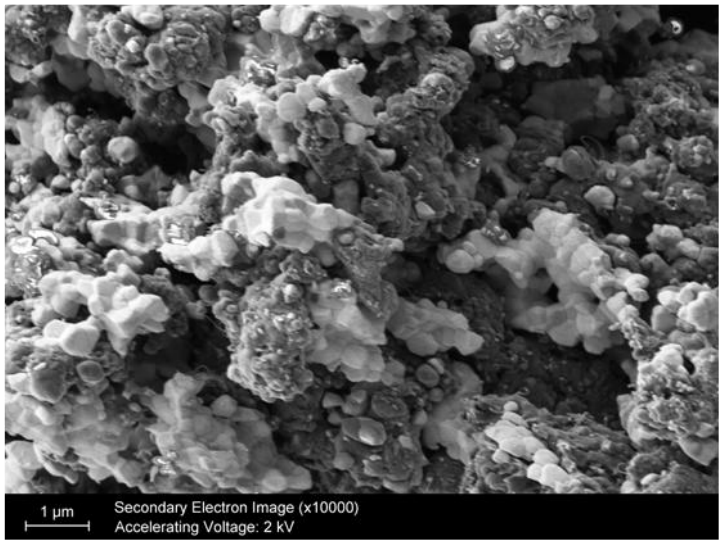


**Figure 3.7. Secondary electron images for the Ni-YSZ anodes of the anode-supported cells after power generation for 20 h with supplies of (a) CO-$CO_2$ mixture at 650 ºC and (b) $H_2O$-$CH_4$ mixture at 800 ºC.**

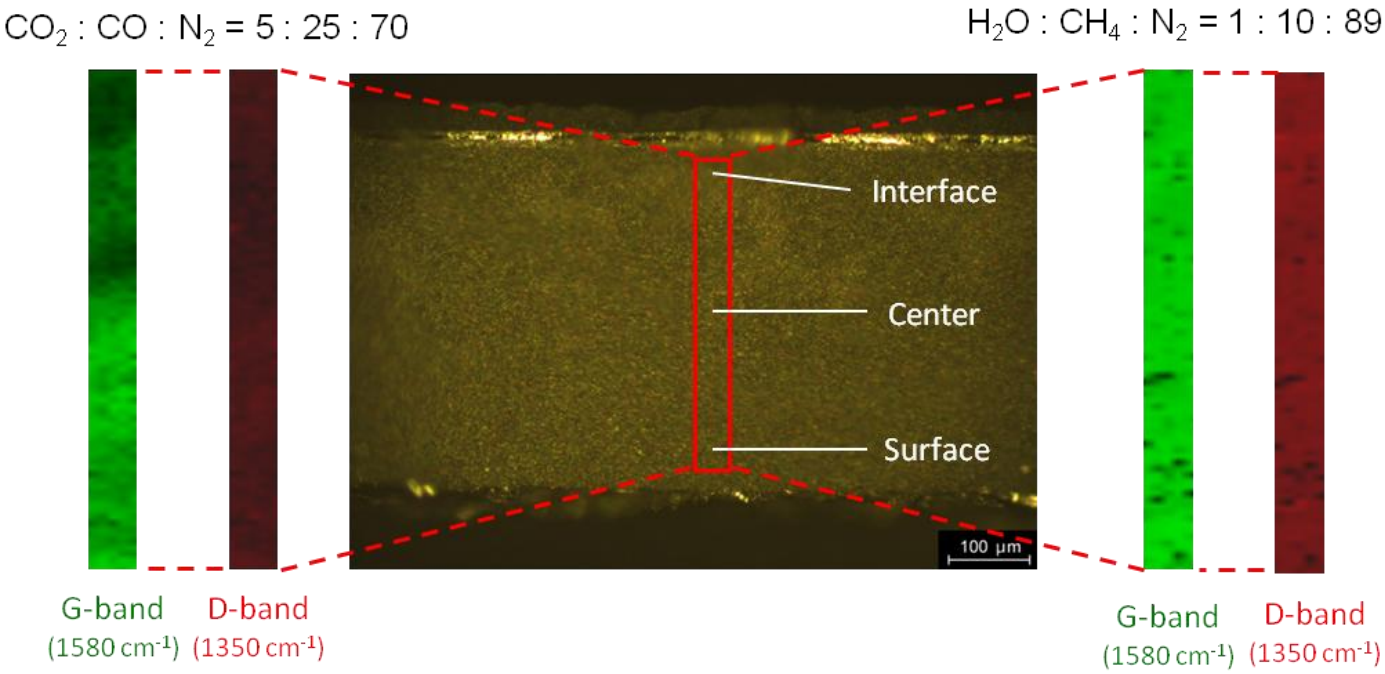


**Figure 3.8. Raman mapping image and spectra for the Ni-YSZ anodes of the anode-supported cells after power generation for 20 h with supplies of (a) $CO_2$-CO mixture at 650 ºC and (b) $H_2O$-$CH_4$ mixture at 800 ºC.**

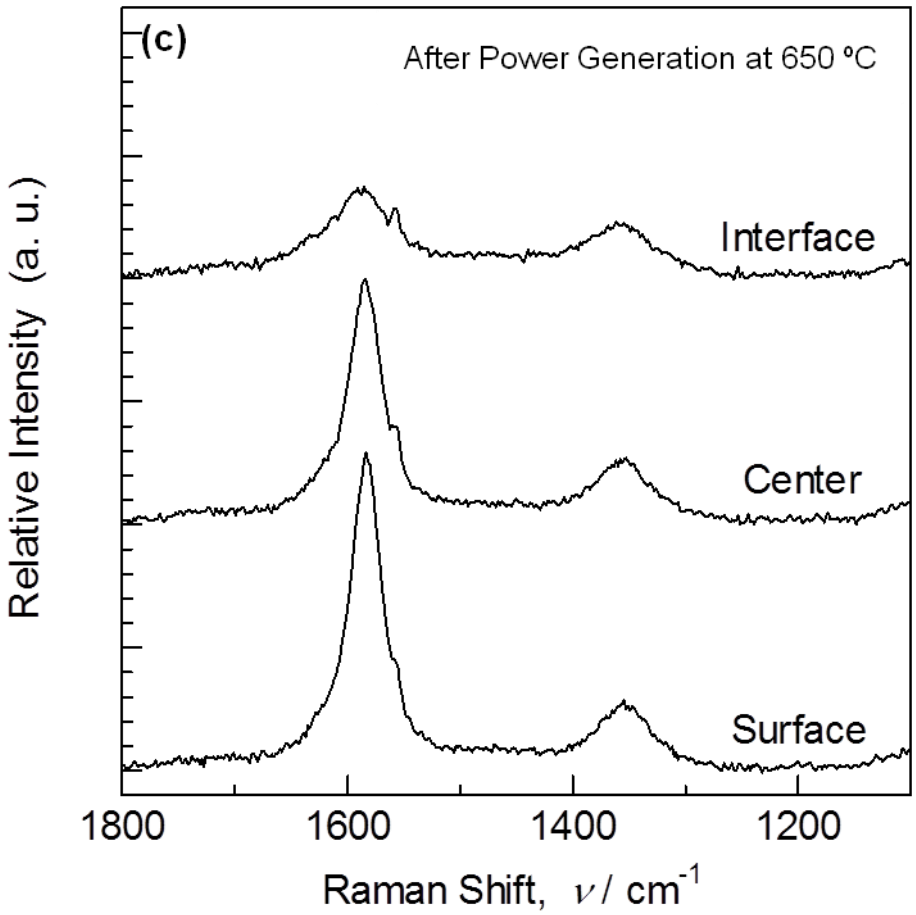


**Figure 3.8. Raman mapping image and spectra for the Ni-YSZ anodes of the anode-supported cells after power generation for 20 h with supplies of (c) $CO_2$-CO mixture at 650 ºC.**

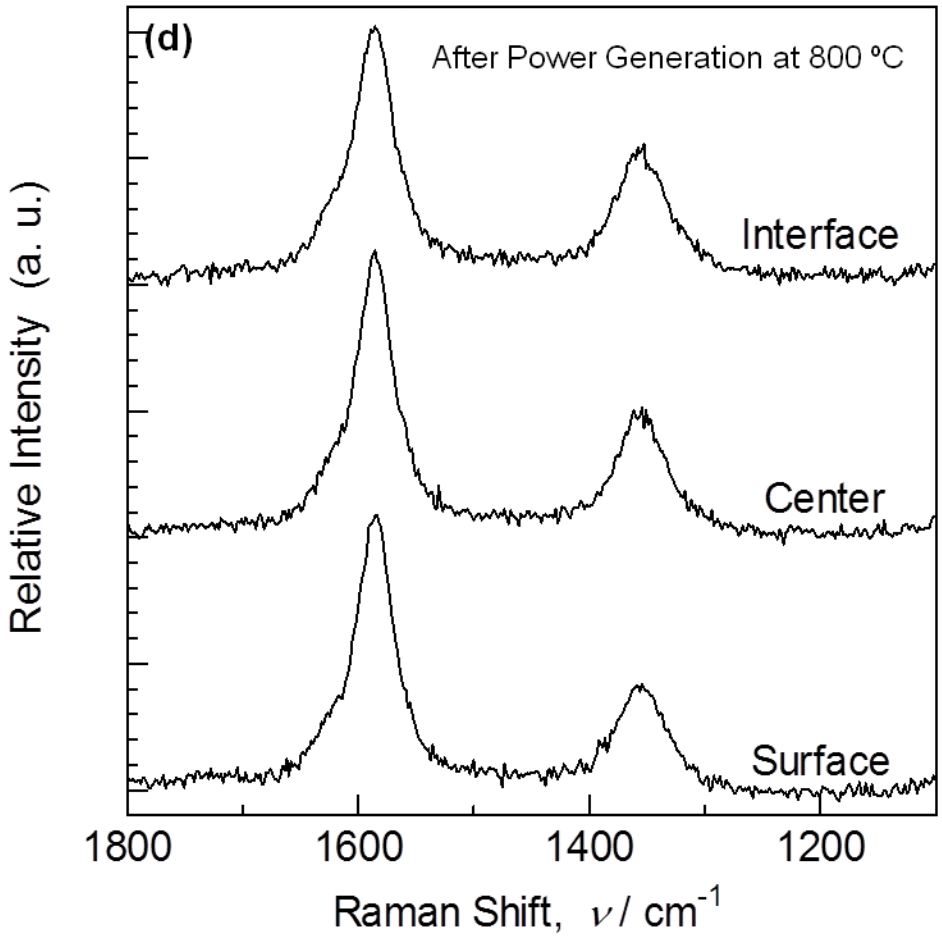


**Figure 3.8. Raman mapping image and spectra for the Ni-YSZ anodes of the anode-supported cells after power generation for 20 h with supplies of (d) $H_2O$-$CH_4$ mixture at 800 ºC**

# Chapter 4

# Influence of Carbon Deposition and Removal on Performance of Ni–YSZ Anode in Internal Methane Steam Reforming for Solid Oxide Fuel Cells

## 4.1 Introduction

The deterioration of anode performance induced by carbon deposition is a serious problem for internal reforming operation as reported in chapter 1 to chapter 3. It is suggested that the deposited carbon damaged the electric conduction path and disturbed the fuel diffusion in the anode, resulting in increases of ohmic and polarization resistances. Because it is difficult to inhibit carbon deposition completely, the carbon removal from the anode is also important for SOFCs. In the hydrogen production process by steam reforming of hydrocarbon, the regeneration treatment was used to recover Ni–base catalyst performance [1-3]. On the other hand, Ihara *et al.* reported that deposited carbon on Ni–YSZ or Ni–gadolinia-doped ceria (Ni–GDC) anode reacted with $O^{2-}$ from cathode directly [4,5]. Although deposited carbon could be removed in anode by various methods, it is still unclear about the electrochemical performance change of the anode induced by carbon deposition and removal.

In this chapter, therefore, the author focuses on the change in anodic performance after carbon removal by gas-feed and current passage in Ni–YSZ anode. The effect of carbon removal from anode was observed by scanning electron microscopy (SEM). The changes of anodic performance induced by carbon deposition and removal were evaluated by impedance spectroscopy.

## 4.2 Experimental

The commercial NiO–YSZ powder (AGC seimi chemical company) with a volume ratio of Ni : YSZ = 47 : 53 and a perovskite-type oxide of $(La_{0.8}Sr_{0.2})_{0.97}MnO_3$ (LSM) powder were used for the anode and cathode, respectively. The powder of each electrode material was mixed with polyethylene glycol (Wako Pure Chemical Industries) to form a slurry. The Ni–YSZ cermet slurry was screen-printed on one face of the YSZ disk (Tosoh, thickness: 500 μm, diameter: 24 mm) at the center, followed by the calcination at 1400 ºC for 5 h (anode thickness: *ca.* 15 μm). The cathode slurry was coated in the same way on the other face of the disk and subsequently heated at 1150 ºC for 5 h. Platinum paste was painted on the side edge of YSZ electrolyte to make the reference electrode. The fabricated cell was sandwiched by alumina tubes with Pyrex glass seals.

The influence of carbon deposition and removal on the anodic performance was investigated at 1000 ºC. A gaseous mixture of 30% $CH_4$–3% $H_2O$–67% $N_2$ was supplied with a steam to carbon ratio (S/C) of 0.1 at OCV for 20 min for carbon deposition. Then, a gaseous mixture of 10% ($H_2$, $H_2O$, or $CO_2$)–90% He and 10% $H_2$–5% $H_2O$–85% He were supplied to the anode for 1 h to remove the deposited carbon. The performance changes were measured by impedance spectroscopy in 90% $H_2$–10% $H_2O$. In addition, the deposited carbon was also removed by discharge at 0.1 A $cm^{-2}$ in 10% $H_2$–90% He or 0.3 A $cm^{-2}$ in 1% $H_2$–99% He. The impedance spectra were also measured in 90% $H_2$–10% $H_2O$ before carbon deposition and after carbon removal. A flow rate of the gaseous mixture in each condition was 100 ml $min^{-1}$. The CellTest system (Solarton Analytical, potentiostat/galvanostat 1470E and frequency response analyzer 1455A)

was used for the electrochemical measurement. During these operations, pure oxygen was supplied to the cathode as an oxidant with a flow rate of 100 ml $min^{-1}$.

The cross-section of anodes before and after carbon removal treatment were analyzed by a scanning electron microscope (FE–SEM, NVision 40, Carl Zeiss) equipped with an energy-dispersive X-ray spectrometer (EDX, Oxford).

### 4.3 Results and discussion

4.3.1 Carbon removal through flowing $H_2$, $CO_2$, and $H_2O$ at OCV

The equilibrium of carbon gasification with $H_2$, CO, and $H_2O$ was predicted by thermodynamic calculation. The standard Gibbs free estimated carried out by MALT/CHD software as shown in Fig. 4.1. In the case of gasification with $CO_2$ and $H_2O$, carbon tends to be gasified with increasing temperature. On the other hand, carbon is difficult to react with $H_2$ at high temperature. In particular, the free energy for carbon removal carbon gasification reaction by $H_2$, $CO_2$ and $H_2O$ at 1000 ºC is as follows:

$$C + 2H_2 \rightarrow CH_4 \qquad \Delta G^o_{1000\ ^oC} = 48.933\ kJ\ mol^{-1} \qquad (4)$$

$$C + CO_2 \rightarrow 2CO \qquad \Delta G^o_{1000\ ^oC} = -26.065\ kJ\ mol^{-1} \qquad (5)$$

$$C + H_2O \rightarrow CO + H_2 \qquad \Delta G^o_{1000\ ^oC} = -46.751\ kJ\ mol^{-1} \qquad (6)$$

As a result, the ease of carbon gasification at 1000 ºC is expected in the following sequence, $H_2O > CO_2 > H_2$.

The experiments of carbon deposition in $CH_4$ mixture and then removal with $H_2$, CO, and $H_2O$ were conducted. Figure 4.2 shows the backscattered electron image of Ni–YSZ anode after holding at OCV for 20 min by supplying 30% $CH_4$–3% $H_2O$–67% $N_2$ mixture (S/C = 0.1). The light gray region was attributed to Ni or YSZ by EDX analysis, and the dark gray region to carbon. Carbon distributed homogenously in the

whole Ni–YSZ anode layer, covering the surface of Ni particles. After carbon deposition treatment, the impedance spectrum of the Ni–YSZ anode was measured. Figure 4.3 shows that the ohmic resistance (defined as the high frequency intercept of the impedance spectra) remained unchanged after the carbon deposition while the polarization resistance (defined as the distance between the *x*-intercepts of the semicircle) increased due to the reduction of reactive sites by carbon deposition.

Subsequently, the deposited carbon was removed by flowing $H_2$, $CO_2$, and $H_2O$ for 1 h, and the backscattered electron (BSE) images of the cross-section of Ni–YSZ anode are shown in Fig. 4.4(a–c). As shown in Fig. 4.4(a), after flowing 10% $H_2$–90% He for 1 h, most of carbon still remained in the anode. In the case of 10% $CO_2$–90% He (see Fig. 4.4(b)), much less carbon was observed in the anode. On the other hand, after flowing 10% $H_2O$–90% He, carbon was removed completely and all of Ni particles and YSZ can be observed clearly in Fig. 4.4(c). These results agree with the sequence of ease in carbon gasification predicted by the thermodynamic calculation.

The impedance spectra of the Ni–YSZ anode before carbon deposition and after carbon removal by different gases were measured at OCV in 90% $H_2$–10% $H_2O$ and the results are shown in Fig. 4.5. After carbon removal by 10% $H_2$–90% He, the ohmic resistance (see Fig. 4.5(a)) remained unchanged while the polarization resistance increased significantly as compared with that before the carbon deposition. This is because a part of the reactive sites, *i.e.*, triple-phase boundary of YSZ, Ni and gas phases, were still covered by carbon. In the case of carbon removal by 10% $CO_2$–90% He, the increment of the polarization resistance was much smaller than in the case of $H_2$, resulting from less remained carbon in the anode (see in Fig. 4.4(b)). However, the ohmic resistance increased after carbon removal by $CO_2$. Although 10% $H_2O$–90% He

removed carbon more effectively (see in Fig. 4.4(c)), both the ohmic and polarization resistances increased dramatically (Fig. 4.5(c)). The degradation of anode after supply of $CO_2$ and $H_2O$ for 1 h may be caused by surface oxidation of Ni in the cermet, which is determined by the oxygen partial pressure ($P(O_2)$). According to the thermodynamic data, metallic nickel is oxidized to NiO at $P(O_2) > 10^{-13}$ atm at 1000 ºC. $P(O_2)$ during supply of $H_2$–He mixture was *ca.* $10^{-21}$ atm (calculated from OCV), under this condition, no oxidation reaction of Ni would occur. However, the value of $P(O_2)$ was *ca.* $10^{-11}$ atm in $CO_2$–He or $H_2O$–He atmosphere. As a result, Ni would be oxidized to less conductive and inactive species, such as NiO, leading to performance degradation of the anode. Since $H_2O$ removed carbon the most effectively, the larger surface of Ni in the cermet was exposed to $H_2O$ and oxidized.

In order to suppress the oxidation of Ni particles, $H_2$ was supplied to anode together with $H_2O$ to reduce $P(O_2)$. Figure 4.6 shows the backscattered electron images of the Ni–YSZ anode cross-section after the supply of 10% $H_2$–5% $H_2O$–85% He for 1 h. $P(O_2)$ was estimated to be *ca.* $10^{-15}$ atm according to the OCV value. The corresponding impedance spectra measured at OCV in 90% $H_2$–10% $H_2O$ are shown in Fig. 4.7. Most of carbon was removed from the Ni–YSZ anode cross-section in Fig. 4.6. As is shown in Fig.4.7, no significant change in the ohmic resistance of the anode was observed before carbon deposition and after the carbon removal treatment. Consequently, it is convinced that the oxidation of Ni was inhibited, leading to the suppression of performance degradation. In this way, carbon was effectively removed without significant performance degradation of the anode.

4.3.2 Carbon removal through power generation

The deposited carbon on the anode can be also removed by applying current [4-6]. After the carbon deposition at OCV for 20 min by supplying 30% $CH_4$–3% $H_2O$–67% $N_2$, the anode was polarized at constant current densities of 0.1 and 0.3 A $cm^{-2}$. Figure 4.8 shows the typical backscattered electron images of the anode cross section after discharging at 0.1 A $cm^{-2}$ in 10% $H_2$–90% He and 0.3 A $cm^{-2}$ in 1% $H_2$–99% He for 1 h. After discharge at 0.1 A $cm^{-2}$ in 10% $H_2$–90% He for 1 h, the deposited carbon disappeared significantly near the anode/electrolyte interface in Fig. 4.8(a). During discharge operation, the electrochemically active sites were located in the vicinity of anode/electrolyte interface. As a result, $H_2O$ was generated by the electrochemical reaction and reacted with carbon more effectively than $H_2$. Moreover, in the case of 0.3 A $cm^{-2}$ in 1% $H_2$–99% He for 1 h, carbon was removed entirely from the Ni–YSZ anode cross section. It is indicated that the generated $H_2O$ was effective in removing deposited carbon even in the lower $H_2$ concentration condition.

The impedance spectra of the anode before carbon deposition and after carbon removal were also measured at OCV in 90% $H_2$–10% $H_2O$ and the results are shown in Fig. 4.9. The ohmic resistance increased slightly after discharge at constant current densities of 0.1 A $cm^{-2}$ in 10% $H_2$–90% and 0.3 A $cm^{-2}$ in 1% $H_2$–99% He for 1 h. As mentioned above, the electrochemical reaction occurred mainly near the anode/electrolyte interface. In addition, because deposited carbon would disturb the gas diffusion in the anode [7], $O^{2-}$ from cathode may react with Ni due to fuel shortage condition. Thus, the increase of ohmic resistance may be attributed to disconnection of nickel network and/or the increase in contact resistance between the anode and the electrolyte [8]. On the other hand, it is indicated from the comparison of Fig. 4.5(a) with

Fig. 4.9(a) that the changes in the polarization resistance corresponded well with residual carbon after carbon removal operation (see in Fig. 4.4(a) and Fig. 4.8(a)). Moreover, after discharge at 0.3 A $cm^{-2}$ in 1% $H_2$–99% He for 1 h in Fig. 4.9(b), the polarization resistance of anode was completely recovered because of carbon removal entirely (see in Fig. 4.8(b)). Even through discharge at 0.3 A $cm^{-2}$, the total flow rate of $H_2O$ generated through electrochemical reaction was estimated to be 0.65 ml $min^{-1}$, which covered only 0.65% in the anode gas. Therefore, the amount of removed carbon is expected to be less than that with supply of 10% $H_2$–5% $H_2O$–85% He as far as the concentration of oxidant is concerned. However, the polarization resistance after supply of 10% $H_2$–5% $H_2O$–85% He in Fig. 4.7 was still 2-fold larger than initial state. It is suggested that a part of deposited carbon still remained in the anode. Kishimoto *et al*. suggested that the $H_2O$ via the electrochemical reaction on the TPB can diffuse on the Ni surface to remove deposited carbon or promote reforming reaction effectively [9, 10].

## 4.4 Conclusions

In this study, it was attempted to remove carbon from the anode by two methods. Carbon was removed homogenously in the whole Ni–YSZ anode layer by flowing $H_2$, $H_2O$, and $CO_2$. The other method was supplying $O^{2-}$ to the anode via current passage. In this case, carbon near anode/electrolyte interface was removed preferentially. The ease of carbon removal in different atmospheres as followed the order: $O^{2-} > H_2O > CO_2 > H_2$. However, Ni in the anode cermet tended to be oxidized by $H_2O$ and $CO_2$, which gave rise to the performance degradation of the anode. On the other hand, in the 10% $H_2$–5% $H_2O$ atmosphere ($P(O_2) < 10^{-13}$ atm), carbon could be removed without the

significant performance degradation. In the case of carbon removal through electrochemical reaction, carbon could be removed the most effectively without appreciable performance degradation.

**References**


1. J. L. Figueiredo and D. L. Trimm, *J. Catal.*, **40**, 154 (1975).
2. R. Aiello, J. E. Fiscus, H. Loye, and M. D. Amiridis, *Appl. Catal. A General*, **192**, 227 (2000).
3. S. Takenaka, Y. Tomikubo, E. Kato, K. Otuka, *Fuel*, **83**, 47 (2004) .
4. M. Ihara, K. Matsuda, H. Sato, and C. Yokoyama, *Solid State Ionics*, **175**, 51 (2004).
5. S. Hasegawa and M. Ihara, *J. Electrochem. Soc.*, **155**(1), B58 (2008).
6. J.-H. Koh, B.-S. Kong, H.-C. Lim, and Y.-S. Yoo, *Electrochem. Solid-state Lett.*, **4**, A12(2001).
7. Y.-H. Lee, H. Sumi, H. Muroyama, T. Matsui, and K. Eguchi, *J. Electrochem. Soc.*, **160**(6), F579 (2013).
8. H. Sumi, R. Kishida, J. Kim, H. Muroyama, T. Matsui, and K. Eguchi, *J. Electrochem. Soc.*, **157**(12), B1747 (2010).
9. H. Kishimoto, K. Yamaji, T. Horita, Y.P. Xiong, N. Sakai, M.E. Brito, and H. Yokokawa, *J. Electrochem. Soc.*, **153**(6), A982 (2006).
10. H. Kishimoto, Katsuhiko Yamaji, Teruhisa Horita, Yueping Xiong, Natsuko Sakai, M. E. Brito, and Harumi Yokokawa, *J. Power Sources*., **172**, 67 (2007).

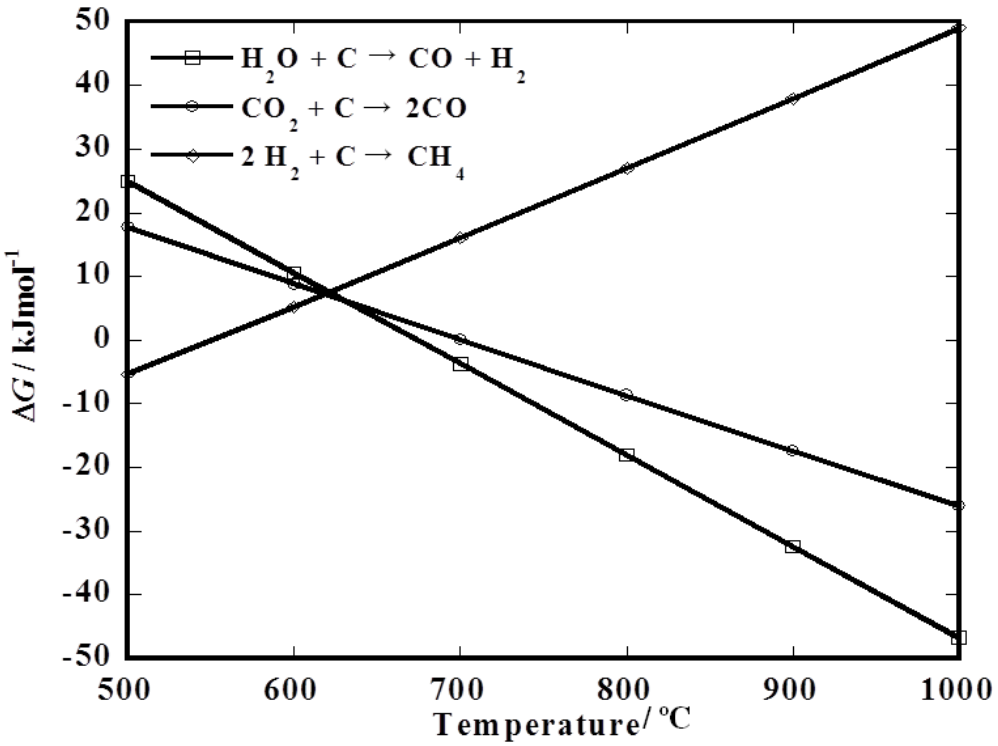


**Figure 4.1. Free energy of carbon gasification by $H_2$, $H_2O$, and $CO_2$ from 500 ºC to 1000 ºC.**

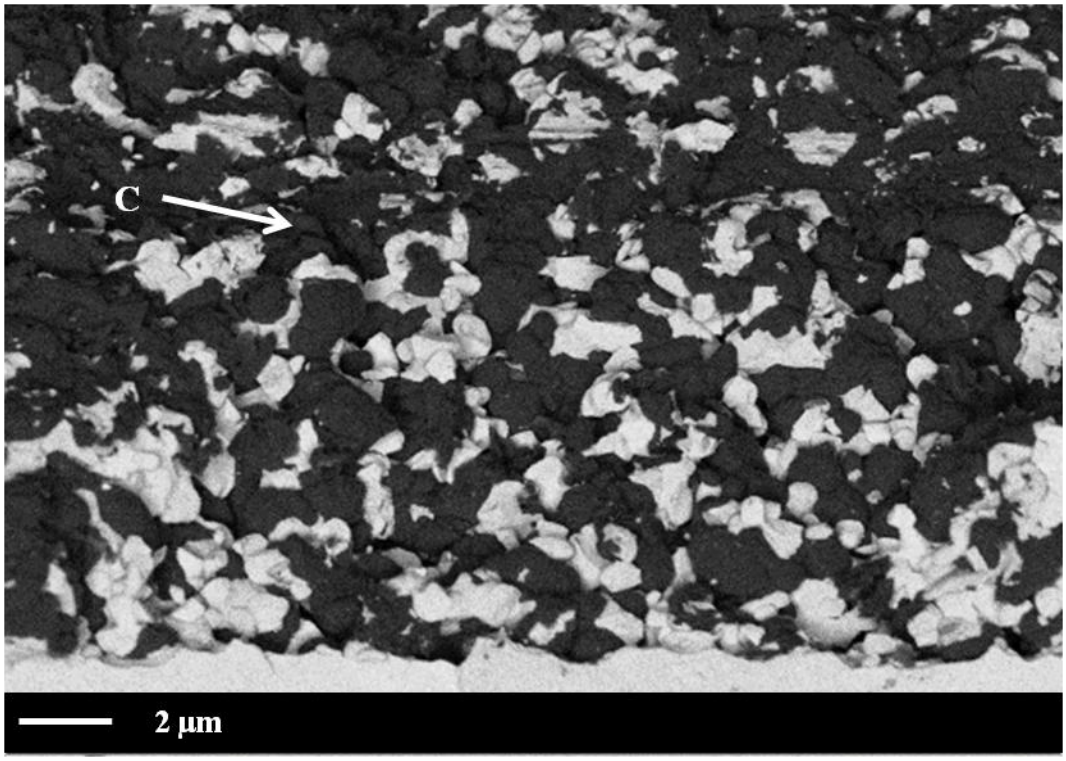


**Figure 4.2. Backscattered electron image of the Ni–YSZ anode layer under OCV at 1000 ºC before and after supply of 30% $CH_4$–3% $H_2O$–67% $N_2$ to anode for 20 min.**

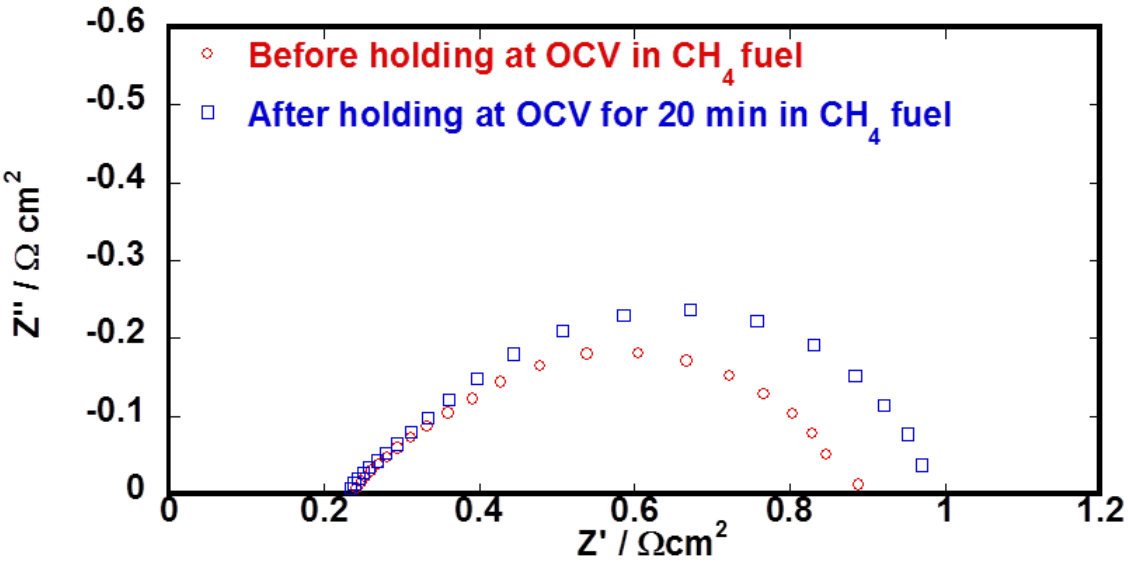


**Figure 4.3. Impedance spectra of the Ni–YSZ anode under OCV at 1000 ºC before and after supply of 30% $CH_4$–3% $H_2O$–67% $N_2$ to anode for 20 min.**

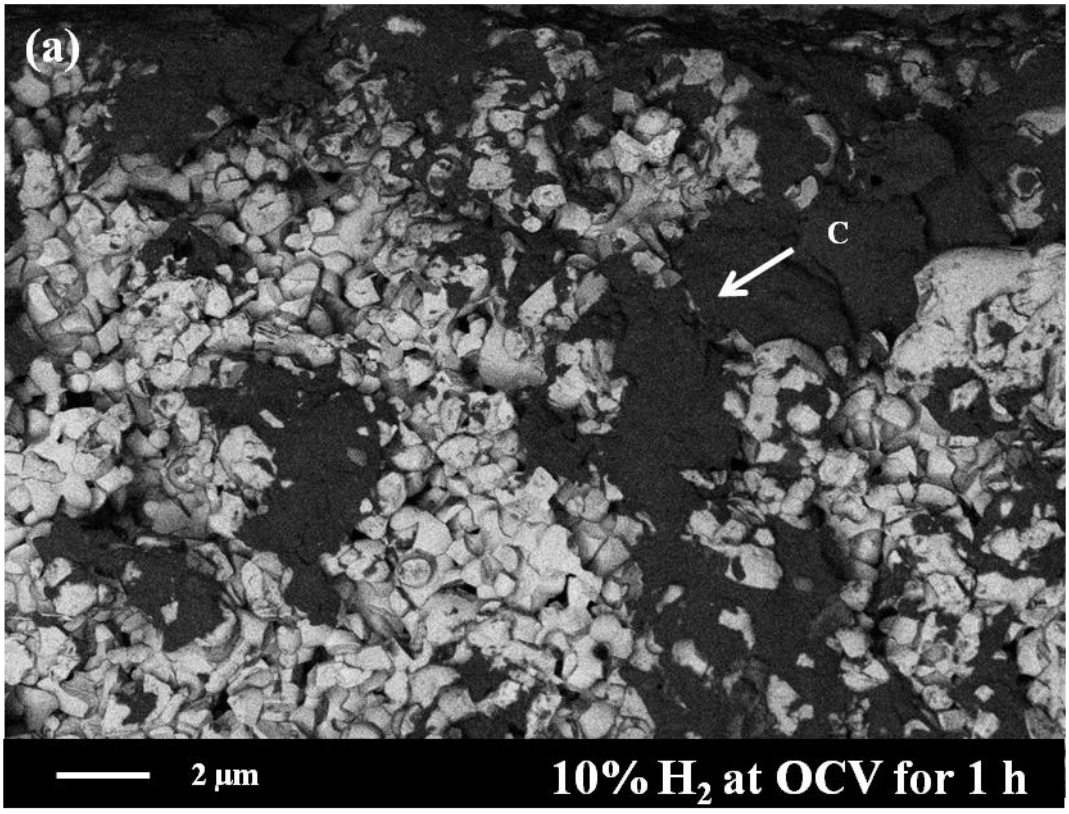


**Figure 4.4. Backscattered electron images for the Ni–YSZ anode layer after removing carbon by flowing (a) 10% $H_2$–90% He at OCV for 1 h.**

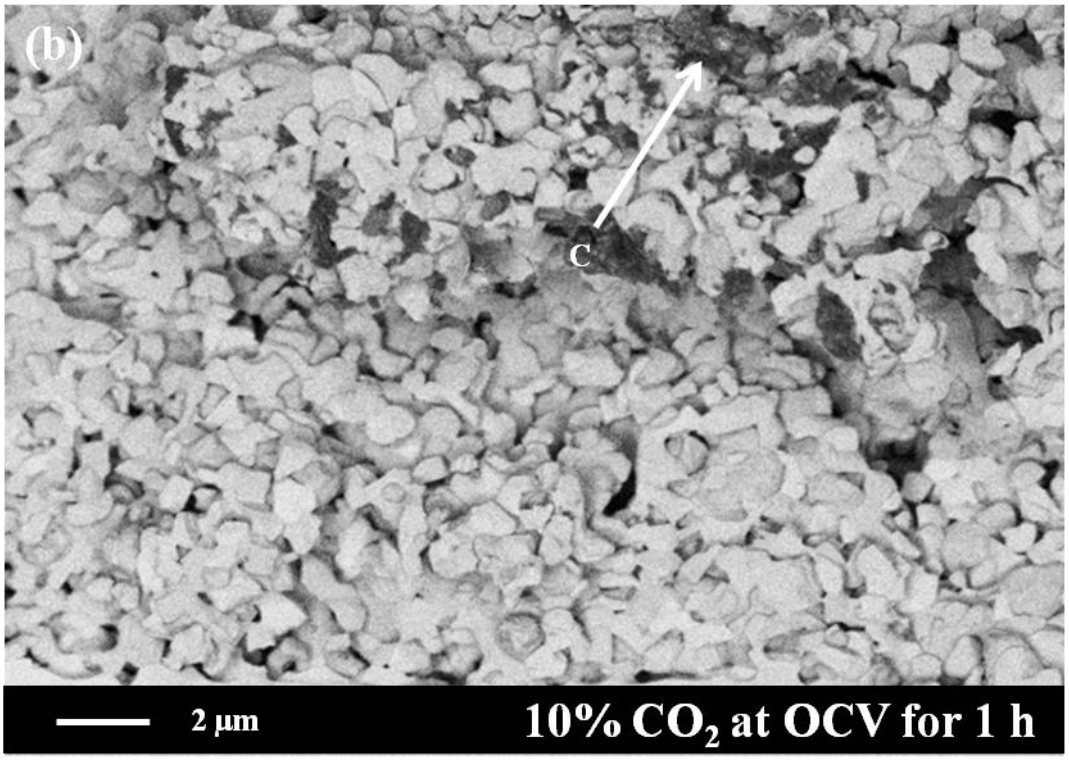


**Figure 4.4 Backscattered electron images for the Ni–YSZ anode layer after removing carbon by flowing (b) 10% $CO_2$–90% He at OCV for 1 h.**

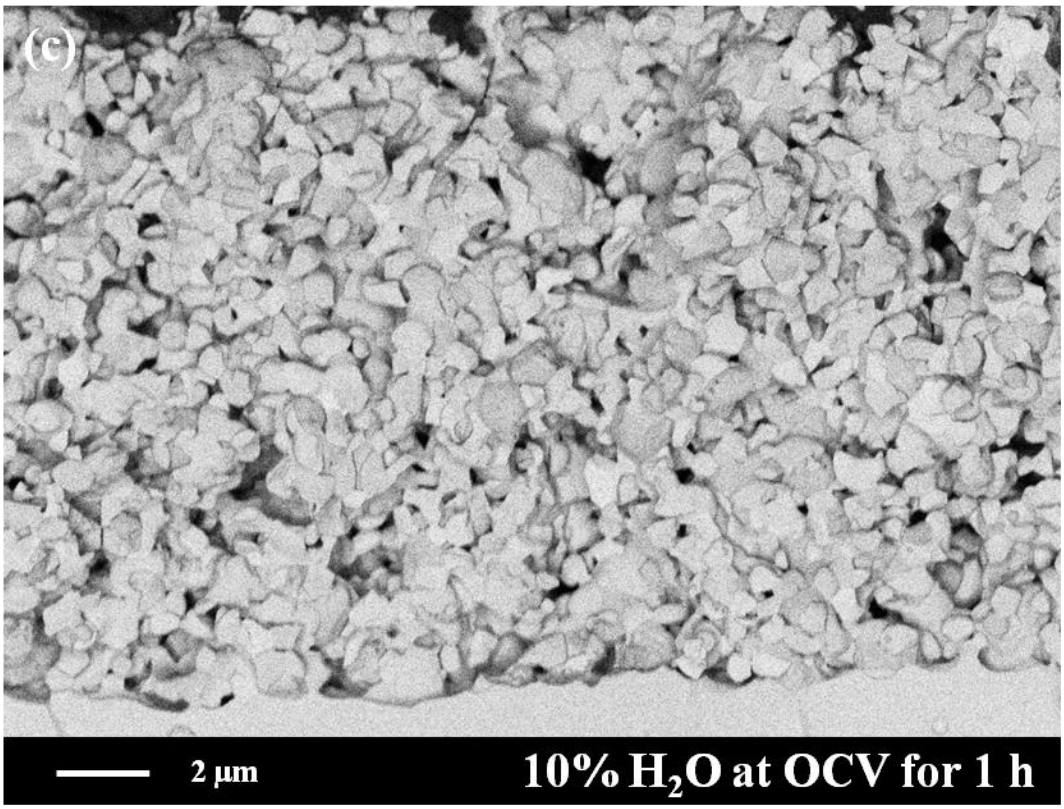


**Figure 4.4 Backscattered electron images for the Ni–YSZ anode layer after removing carbon by flowing (c) 10% $H_2O$–90% He at OCV for 1 h.**

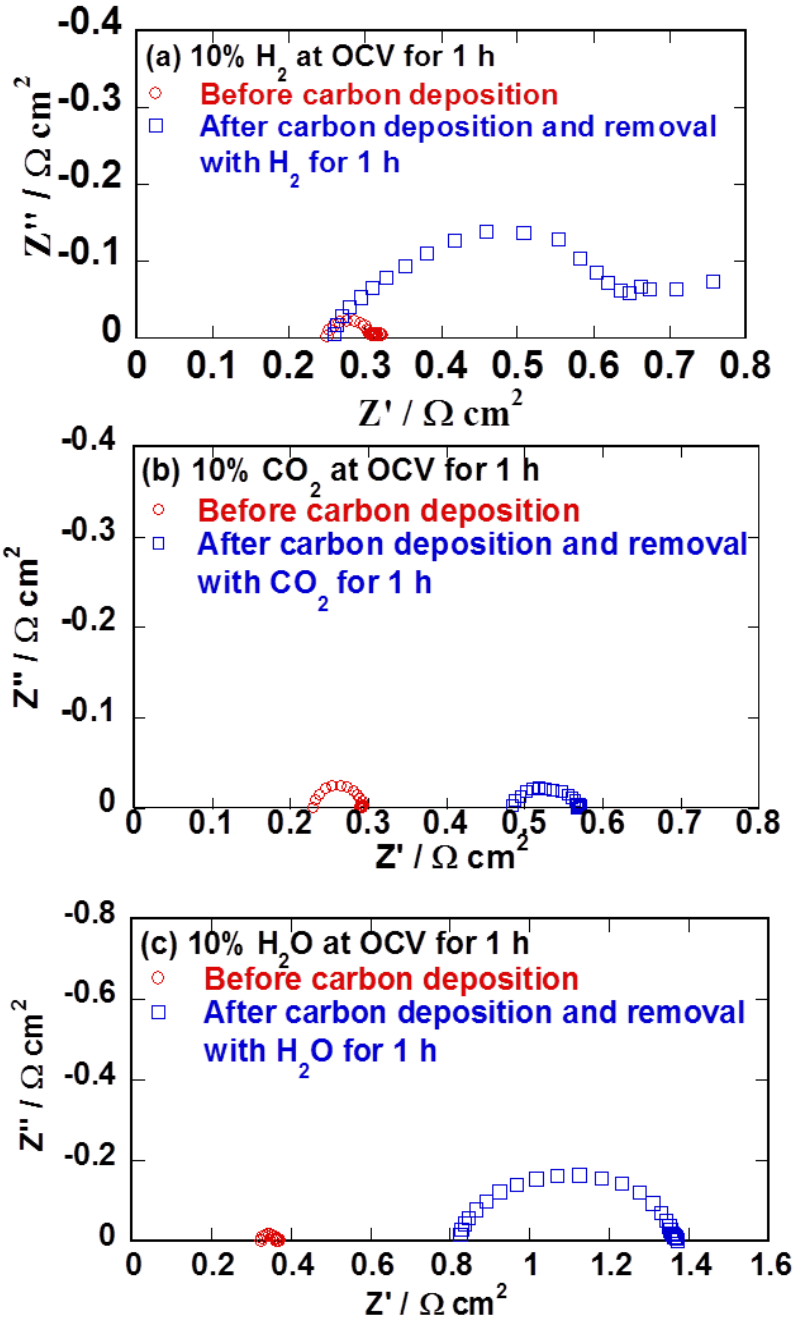


**Figure 4.5 Impedance spectra of the Ni–YSZ anode under OCV at 1000 °C with measurement on a 10% $H_2O$–90% $H_2$ to anode before carbon deposition and after removing carbon by flowing (a) 10% $H_2$–90% He, (b) 10% $CO_2$–90% He, and (c) 10% $H_2O$–90% He.**

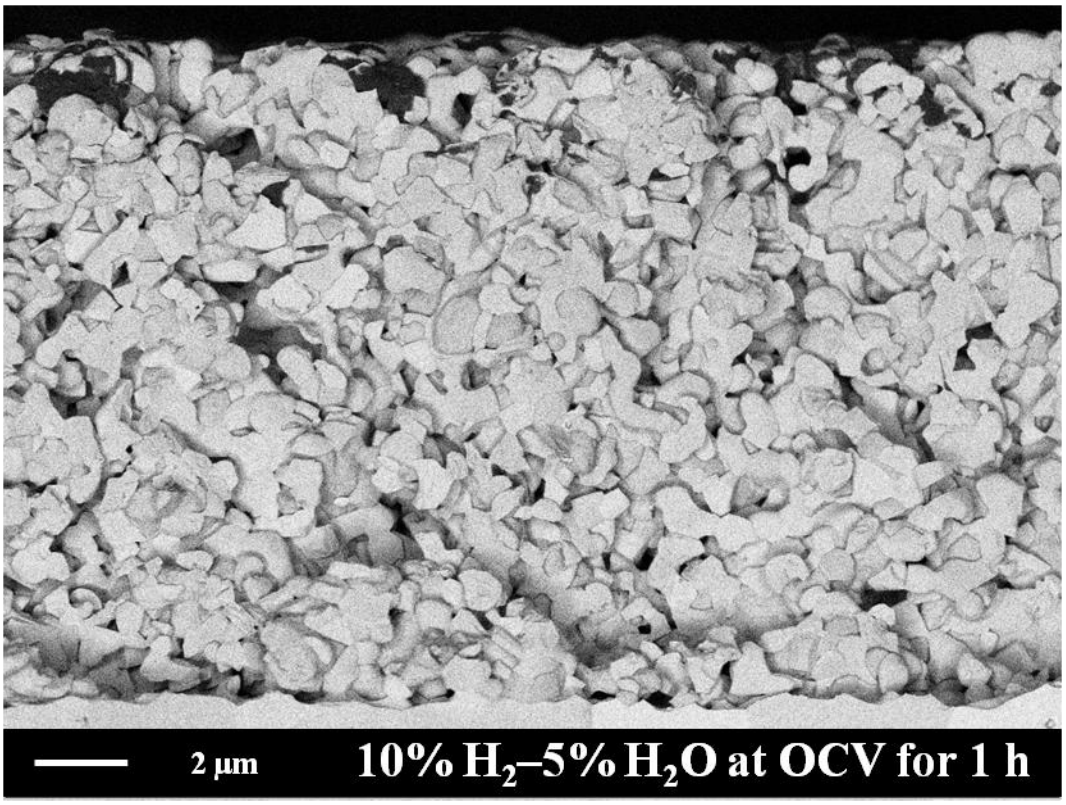


**Figure 4.6 Backscattered electron images for the Ni–YSZ anode layer after removing carbon by flowing 10% $H_2O$–5% $H_2$–85% He at OCV for 1 h.**

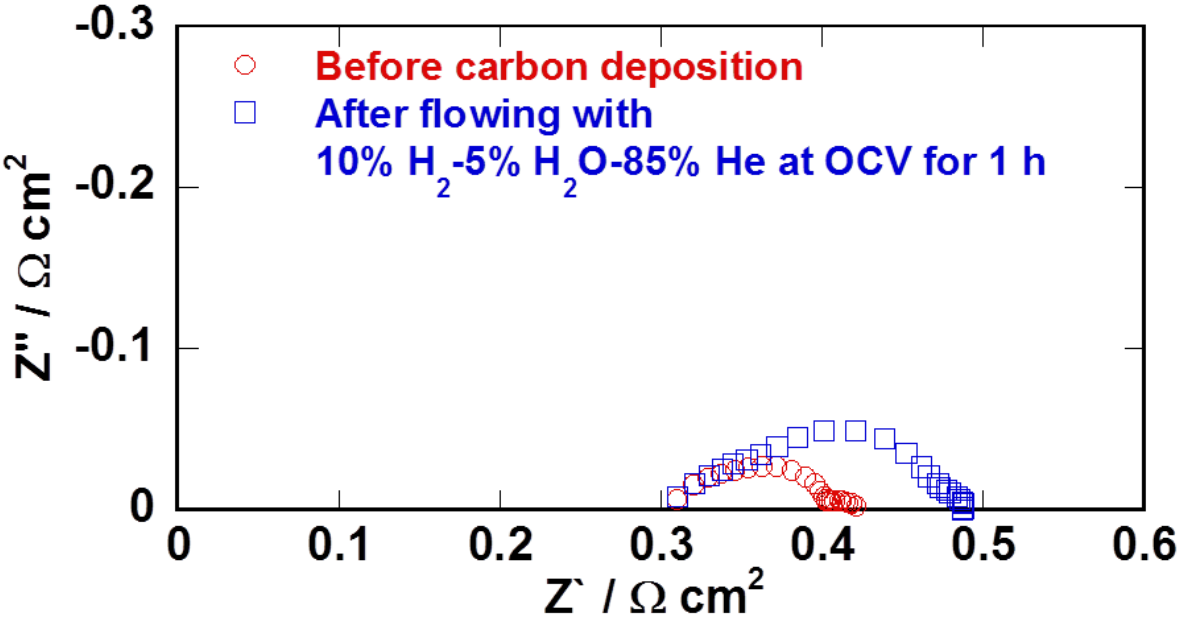


**Figure 4.7 Impedance spectra of the Ni–YSZ anode under OCV at 1000 °C with measurement on a 10% $H_2O$–90% $H_2$ to anode before carbon deposition and after removing carbon by flowing 10% $H_2$–5% $H_2O$.**

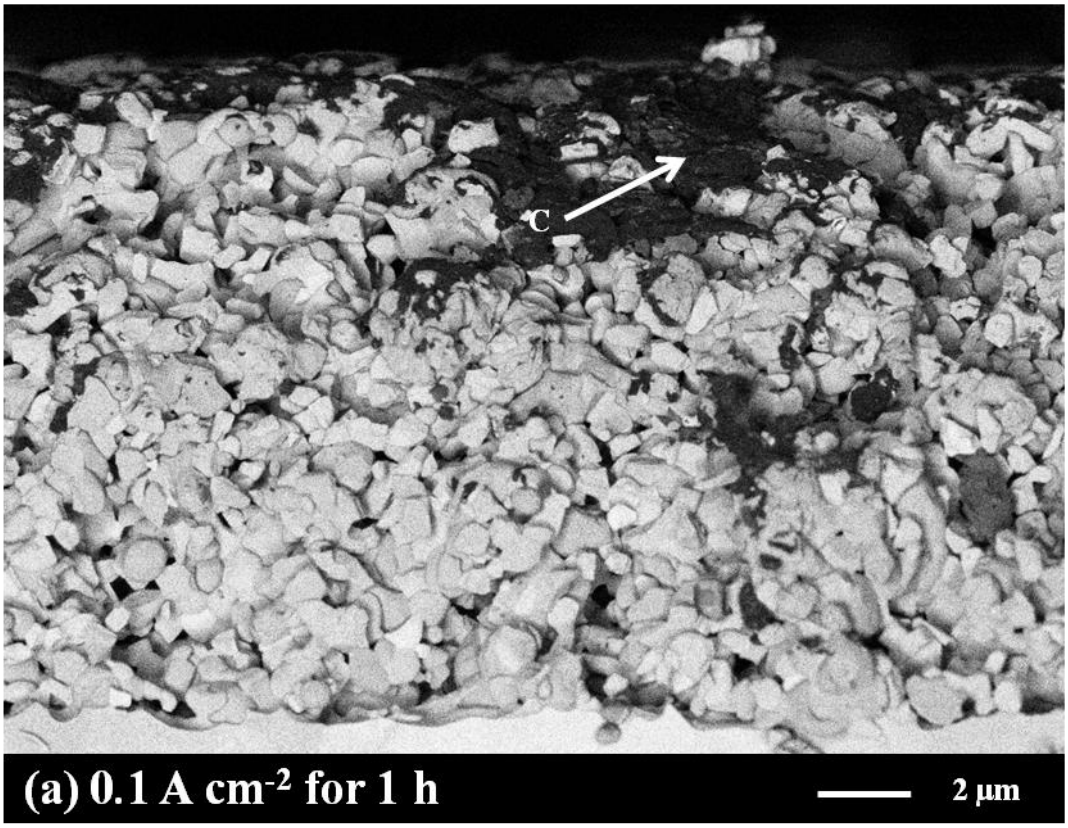


**Figure 4.8. Backscattered electron images for the Ni–YSZ anode layer after removing carbon by discharge at (a) 0.1 A $cm^{-2}$ in 10% $H_2$–90% He for 1 h.**

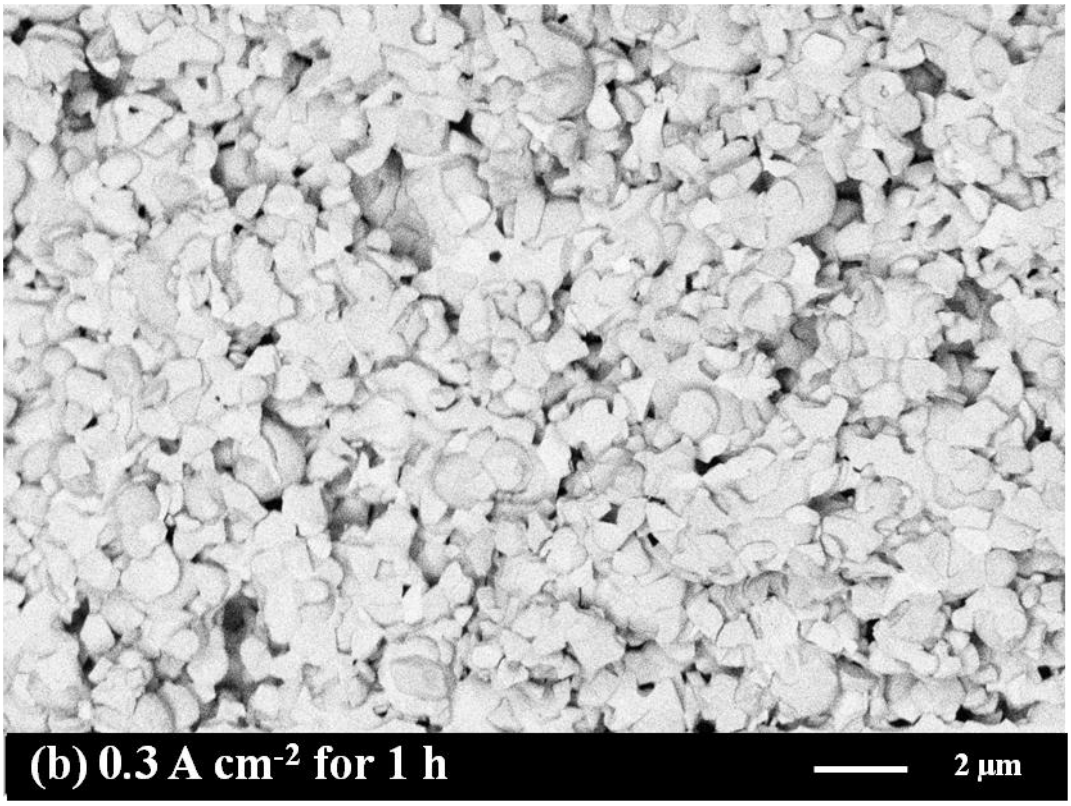


**Figure 4.8. Backscattered electron images for the Ni–YSZ anode layer after removing carbon by discharge at (b) 0.3 A $cm^{-2}$ in 1% $H_2$–99% He for 1 h.**

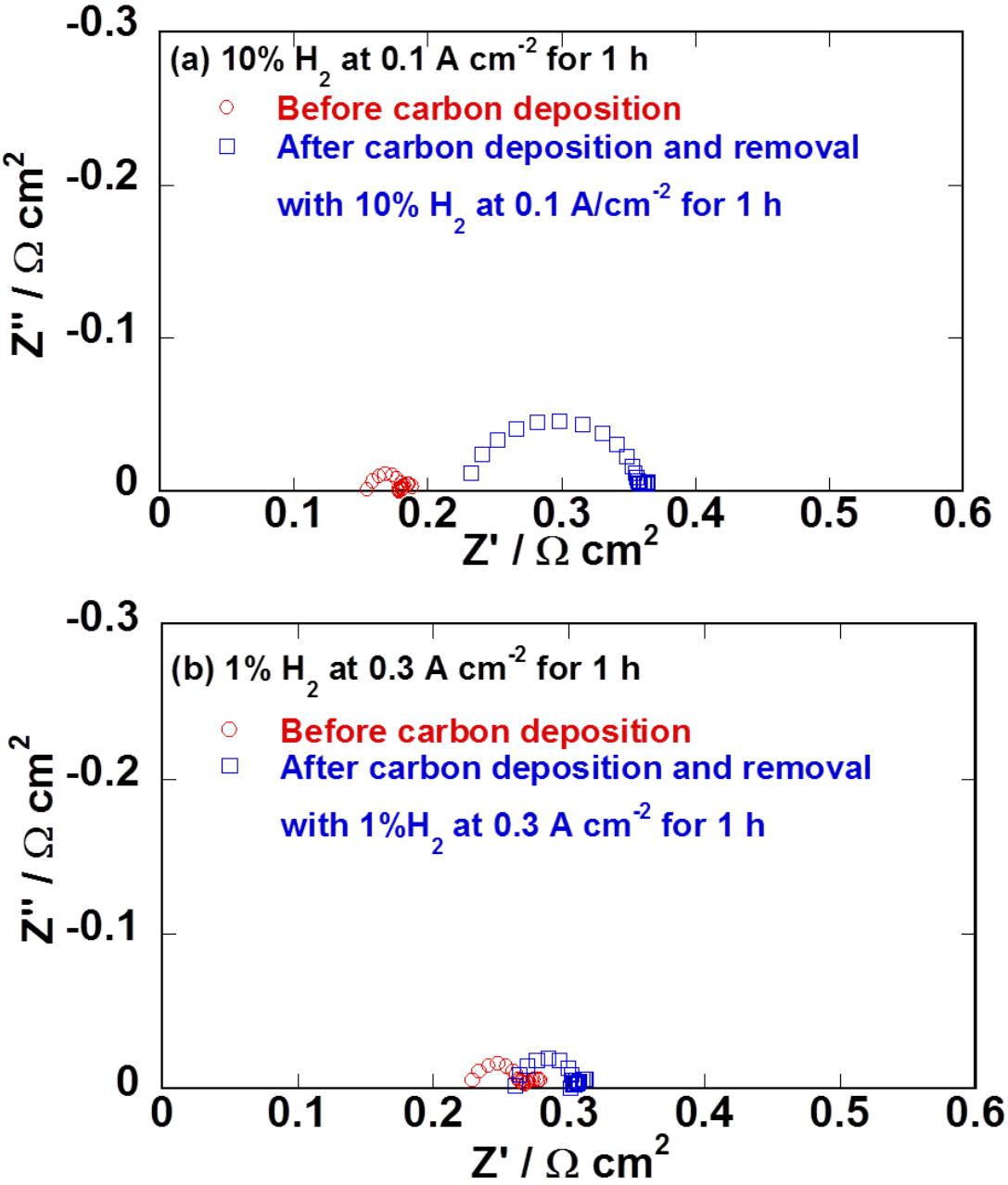


**Figure 4.9 Impedance spectra of the Ni–YSZ anode under OCV at 1000 ºC with measurement on a 10% $H_2O$–90% $H_2$ to anode before carbon deposition and after removing carbon by discharge at (a) 0.1 A $cm^{-2}$ in 10% $H_2$–90% He and (b) 0.3 A $cm^{-2}$ in 1% $H_2$–99% He for 1 h.**

# Chapter 5

# Degradation Induced by Sintering of Ni–YSZ Anode in Solid Oxide Fuel Cells

## 5.1 Introduction

Solid oxide fuel cells (SOFCs) are the attractive power generation systems due to the low emission, high efficiency, and fuel flexibility at high temperatures [1, 2]. The Ni–yttria–stabilized zirconia (Ni–YSZ) cermet is most common material of anode for the practical SOFC systems. The electrochemical reaction between the oxide ions, the hydrogen, and electrons only occurs at the triple-phase boundary (TPB) in Ni–YSZ anode [3-5]. The performance degradation occurred in Ni–YSZ anode cermet due to long-term operation by supply of humidity hydrogen [6-10].

Many studies have been devoted to clarify the degradation reasons for Ni–YSZ anode under long-term operation. Simwonis *et al*. reported that electrical conductivity decreased in the Ni–YSZ cermet at 1000 ºC after supply of 4% $H_2$–3% $H_2O$–93% Ar for 4000 h [9]. The YSZ particles showed no changes before and after treatments. On the other hand, the sintering behavior of Ni particles could be observed. Tanasini *et al.* have demonstrated the polarization resistance increased after operation at a constant current density of 0.6 A $cm^{-2}$ at 850 ºC for 1000 h by flowing 97% $H_2$–3% $H_2O$, resulting from Ni coarsening [10]. It was suggested that the growth of Ni induced reduction of TPB length [10].

In addition, the sintering of Ni particles appeared to strongly enhance with increasing temperature and humidity [11-13]. The mechanism of Ni migration can be considered: (1) surface diffusion and (2) transportation in the gas phase. The surface

diffusion is affected by temperature primarily. In the case of transportation in the gas phase, according to thermodynamic data, the $Ni(OH)_2(g)$ become volatile compound than Ni(g) at 1000 ºC over *ca.* 20% $H_2O$ concentration [14]. It also displayed that $Ni(OH)_2(g)$ is more sensitive to the change of the $H_2O$ concentration. Therefore, the coarsening of Ni particles with increasing humidity may be associated with the partial pressure of $Ni(OH)_2(g)$. However, the quantitative relationship between the sintering of Ni particles and performance deterioration has not been elucidated sufficiently.

In this chapter, the Ni–YSZ anode were treated at 1000 ºC, 1100 ºC, and 1200 ºC for 50 h under highly humidified hydrogen atmospheres to accelerate the microstructural change. After the treatments, the samples were analyzed by focused ion beam–scanning electron microscopy (FIB–SEM) [15-18], and their microstructural change was quantified to clarify the degradation factors.

## 5.2 Experimental

The NiO–YSZ powder with a volumetric ratio of Ni:YSZ = 50:50 and a perovskite-type oxide of $(La_{0.8}Sr_{0.2})_{0.97}MnO_3$ (LSM) powder were used for the anode and cathode, respectively. The Ni–YSZ cermet was prepared from NiO (Wako Pure Chemical Industries) and YSZ powders (8 mol% $Y_2O_3$–$ZrO_2$, Tohoh). The mixture of NiO and YSZ was heat-treated at 1200 ºC for 5 h. A LSM was synthesized from corresponding metal acetates, and calcined at 900 ºC for 5 h. The resulting powder of each electrode material was mixed with polyethylene glycol (Wako Pure Chemical Industries) to form slurry. The NiO–YSZ cermet slurry was screen-printed on one face of the YSZ disk (Tosoh, thickness: 500 μm, diameter: 24 mm) at the center, followed by the calcination at 1400 ºC for 5 h (anode thickness: *ca.* 40 μm). The cathode slurry was

coated in the same way on the other face of the disk and subsequently heated at 1150 ºC for 5 h. Platinum paste was painted on the side edge of YSZ electrolyte to sever as a reference electrode. The fabricated cell was sandwiched by alumina tubes with Pyrex glass seals.

The change in anodic performance was investigated by holding under the open-circuit condition at 1000 ºC, 1100 ºC, and 1200 ºC for 50 h. A gaseous mixture of 90% $H_2$–10% $H_2O$ or 60% $H_2$–40% $H_2O$ was supplied to the anode with a flow rate of 100 ml $min^{-1}$. During these operations, pure oxygen was introduced to the cathode as an oxidant with a flow rate of 100 ml $min^{-1}$. The CellTest system (Solarton Analytical, potentiostat/galvanostat 1470E and frequency response analyzer 1455A) was used for the electrochemical impedance measurement.

After the evaluation of cell performance, the structural change in Ni–YSZ anodes was observed by a dual-beam focused ion beam-scanning electron microscope (FIB–SEM, Nvision 40, Carl Zeiss–SIINT) equipped with an energy dispersive X-ray spectrometer (EDX, Oxford). The cell sample was infiltrated with epoxy resin, and then cut and observed anode cross-section (*x*-*y* plane as Fig. 5.1). The two dimensional SEM images were collected along the *z*-direction by milling-and-see operation as reported by Iwai *et al.* [19]. The 3D microstructure of anode was reconstructed in a computational field (Fig. 5.1). In this study, the microstructural parameters were quantitatively analyzed: volume fraction, size distribution of particles, ratio of isolated-Ni phase, and TPB length.

## 5.3 Results and discussion

The cell performance was examined by impedance measurement with a supply of

10% $H_2O$–90% $H_2$ or 40% $H_2O$–60% $H_2$ to the anode at 1000 ºC, 1100 ºC, and 1200 ºC. The ohmic and polarization resistances of Ni–YSZ at open-circuit condition before and after heat-treatments are summarized in Fig. 5.2. No significant changes in both resistive components were observed in 10% $H_2O$ even at 1100 ºC and 1200 ºC. On the other hand, the resistances increased dramatically during the heat-treatment with 40% $H_2O$ at 1100 ºC and 1200 ºC, although the anode performance was scarcely deteriorated at 1000 ºC in 40% $H_2O$. The deterioration was more remarkable at 1200 ºC. These results indicated that performance degradation of Ni–YSZ was accelerated in higher humidity and temperature. Hereafter, the anode microstructure was quantitatively analyzed by FIB–SEM.

Table 5.1 show the volume fraction of each phase evaluated from the reconstructed Ni–YSZ anodes. Because the volume ratio of Ni to YSZ for all samples was comparable to the nominal composition of Ni:YSZ = 50:50, the series of anode reconstruction and computational analysis were reliable.

The Fig. 5.3 displays the size distributions of YSZ particles, Ni particles, and pore in the Ni–YSZ anodes before and after the heat-treatments with a supply of 10% $H_2O$–90% $H_2$ and 40% $H_2O$–60% $H_2$ at 1000 ºC–1200 ºC. No size change in YSZ particles by the treatment indicated that the degradation of cell performance was not affected by YSZ particles. In contrast, the size distribution of Ni particles shifted to the direction of large size under higher humidity and temperature conditions, suggesting that the sintering of Ni particles should contribute to the degradation of anode performance. In addition, the increment of pore sizes accompanied with the sintering of Ni particles. Such phenomenon has been observed with a supply of 4% $H_2$–3% $H_2O$–93% Ar atmosphere at 1000 ºC for 1000 h–4000 h [9].

The 3D reconstructed images of isolated-Ni phase after holding under 40% $H_2O$–60% $H_2$ atmosphere at 1000 ºC, 1100 ºC, and 1200 ºC for 50 h are displayed in Fig. 5.4. The size of samples and the ratio of isolated-Ni phase to whole Ni phase are listed in Table 5.2. The rectangular specimen corresponds to a whole anode sample. The red regions correspond to the isolated-Ni phase. The isolated-Ni phase is defined as the phase which is unconnected to the any surfaces of anode samples. The isolated Ni phase apparently became quite larger at 1200 ºC. The rate of isolated-Ni phase increased with a rise in treatment temperature, which corresponds to the decrease in effective electronic conduction path. Because this tendency was related to the performance of heat-treated Ni–YSZ anodes, the interruption of electronic conduction path and the concomitant reduction in electrochemical reaction sites should be one of the performance deterioration of Ni–YSZ anodes.

The triple-phase boundary (TPB) length could be also calculated from the 3D microstructure of anodes. The active TPB length was estimated after removing the isolated parts of Ni, YSZ and pore from the whole reconstructed model. Table 5.3 shows total TPB and active TPB lengths for Ni–YSZ anodes subject to heat-treatments. In Table 5.3, both TPB lengths reduced with a rise in humidity and temperature, which originated from the sintering of Ni particles shown in Fig. 5.3(b). Note that the high humidity only slightly decreased the TPB length of anodes at 1100 ºC. In contrary, the deterioration rate of anode performance (see in Fig. 5.2) was strongly affected by the humidity in the treatment atmospheres. Accordingly, the decrease in active TPB length is not the critical factor to cause the degradation of cell performance.

The surface and cross-section of Ni–YSZ anodes were observed at low magnification by SEM. Fig. 5.5(a) and (b) show the surfaces of anode subject to holding

at 1100 ºC in 10% $H_2O$–90% $H_2$ and 40% $H_2O$–60% $H_2$, respectively. Some fine cracks were confirmed on the surface of anode heat-treated at lower humidity, while the higher humidity resulted in the specific crack over the anode surface. The sintering of Ni particles and the concomitant lack of component homogeneity should provide the strain in the anode, leading to the crack formation. Thus the active migration of Ni species would result in apparent cracks at the high humidity atmosphere. Figure 5.6(a) and (b) show the surface and cross section of Ni–YSZ anode exposed to 40% $H_2O$–60% $H_2$ at 1200 ºC for 50 h. Compared with the sample held at 1100 ºC, more obvious cracks could be observed on the surface. From the cross-sectional image, the generation of crack extended from the anode surface to the interface with YSZ electrolyte, with implies that the Ni–YSZ anode seemed to be separated in to several island-like parts. This phenomenon should interrupt the ionic and electronic conductions in the in-plane direction of anode layer. Therefore, the reduction of reaction sites and conduction path induced the severe degradation of anode performance at 1200 ºC under the highly-humidified condition. Throughout this study, it could be concluded that the deterioration of anode performance under high humidity and temperature conditions would be attributable to the progress in the crack formation in the layer rather than the reduction in TPB length.

## 5.4 Conclusions

In this chapter, the Ni–YSZ anodes was held at OCV with supply of humidified hydrogen at 1000 ºC, 1100 ºC, and 1200 ºC, and microstructural change was quantitatively evaluated by FIB–SEM analysis. It was clarified that the growth of Ni particles was accelerated with increasing temperature and humidity. However, the

increasing in isolated-Ni phase and reducing of active TPB length were relatively small considering, the severe degradation of anode performance at high temperature and humidity. It was observed that the Ni–YSZ anode separated into several island-like parts under 40% $H_2O$ atmosphere at 1200 ºC. Consequently, the ionic and electronic conductions in the in-plane direction of anode layer were restricted. This should be dominantly responsible for the degradation of anode performance.

**References**


1. S. M. Haile, *Acta Materialia*, **51,** 5981 (2003).
2. B. C. H. Steele and A. Heinzel, *Nature*, 414, 345 (2001).
3. S. Mclntosh, R. J. Gorte, *Chem. Rev*. **104**, 4845 (2004).
4. Q.-A. Huang, R. Hui, B. Wang, and J. Zhang, Electrochimica. Acta, 52, 8144 (2007).
5. X. Wang, N. Nakagawa, and K. Kato, *J. Electrochem. Soc.*, **148,** A565 (2001).
6. S. P. Jiang, *J. Mater. Sci.*, **38**, 3775 (2003).
7. A. Hauch, M. Mogensen, and A. Hagen, *Solid State Ionics*, **192**, 547 (2011).
8. J. S. Cronin, J. R. Wilson, and S. A. Barnett, *J. Power Sources*, **196**, 2640 (2011).
9. D. Simwonis, F. Tietz, and D. Stöver, *Solid State Ionics*, **132**, 241 (2000).
10. P. Tanasini, M. Cannarozzo, P. Costamagna, A. Faes, J. V. Herle, A. Hessler-Wyser, and C. Comninellis, *Fuel Cells*, 09, 740 (2009).
11. J. Sehested, J. A. P. Gelten, I. N. Remediakis, H. Bengaard, and J. K. Nørskov, *J. Catal.*, **223**, 432 (2004).
12. J. Sehested, *J. Catal*., **217** (2003).
13. L. Holzer, B. Iwanschitz, Th. Hocker, B. Munch, M. Prestat, D. Wiedenmann, U.

Vogt, P. Holtappels, J. Sfeir, A. Mai, and Th. Graule, *J. Power Sources*, **196**, 1279 (2011).

14. T. Matsui, R. Kishida, J. Kim, H. Muroyama, and K. Eguchi, *J. Electrochem. Soc*., **157**, B776 (2010).
15. M. Kishimoto, H. I wai, M. Saito, and H. Yoshida, *J. Power Sources*, **196,** 4555 (2011)**.**
16. N. Vivet, S. Chupin, E. Estrade, T. Piquero, P.L. Pommier, D. Rochais, and E. Bruneton, *J. Power Sources*, **196**, 7541 (2011).
17. J. R. Wilson, M. Gameiro, K. Mischaikow, W. Kalies, P. W. Voorhees, and S. A. Barnett, *Microsc. Microanal.*, **15**, 71 (2009).
18. T. Matsui, J.-Y. Kim, H. Muroyama, M. Shimazu, T. Abe, M. Miyao, and K. Eguchi, *Solid State Ionics*, **225**, 50 (2012).
19. H. Iwai, N. Shikazono, T. Matsui, H. Teshima, M. Kishimoto, R. Kishida, D. Hayashi, K. Matsuzaki, D. Kanno, M. Saito, H. Muroyama, K. Eguchi, N. Kasagi, H. Yoshida, *J. Power Sources*, **195**, 955 (2010).
20. T. Matsui, R. Kishida, H. Muroyama, and K. Eguchi, *J. Electrochem. Soc.*, **159**(8), F456 (2012).

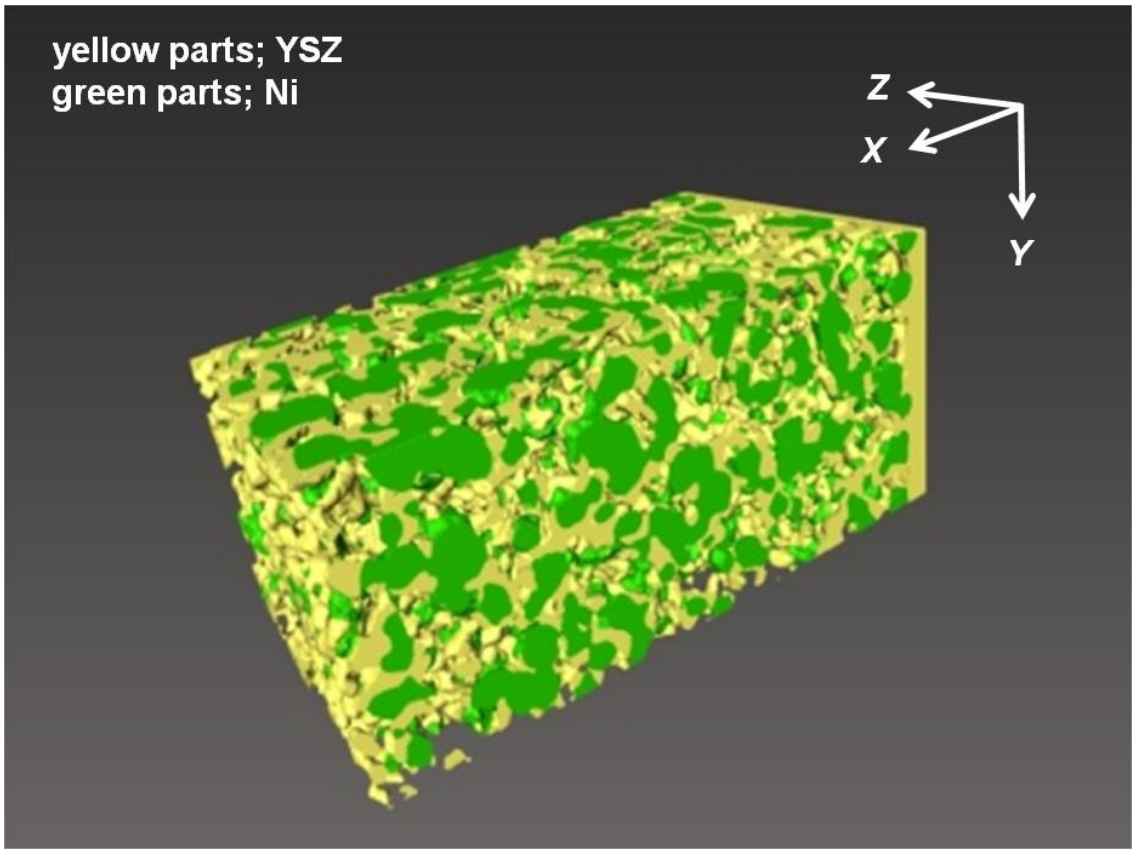


**Figure 5.1. 3D reconstructed Ni (green) and YSZ (yellow) phase in anode.**

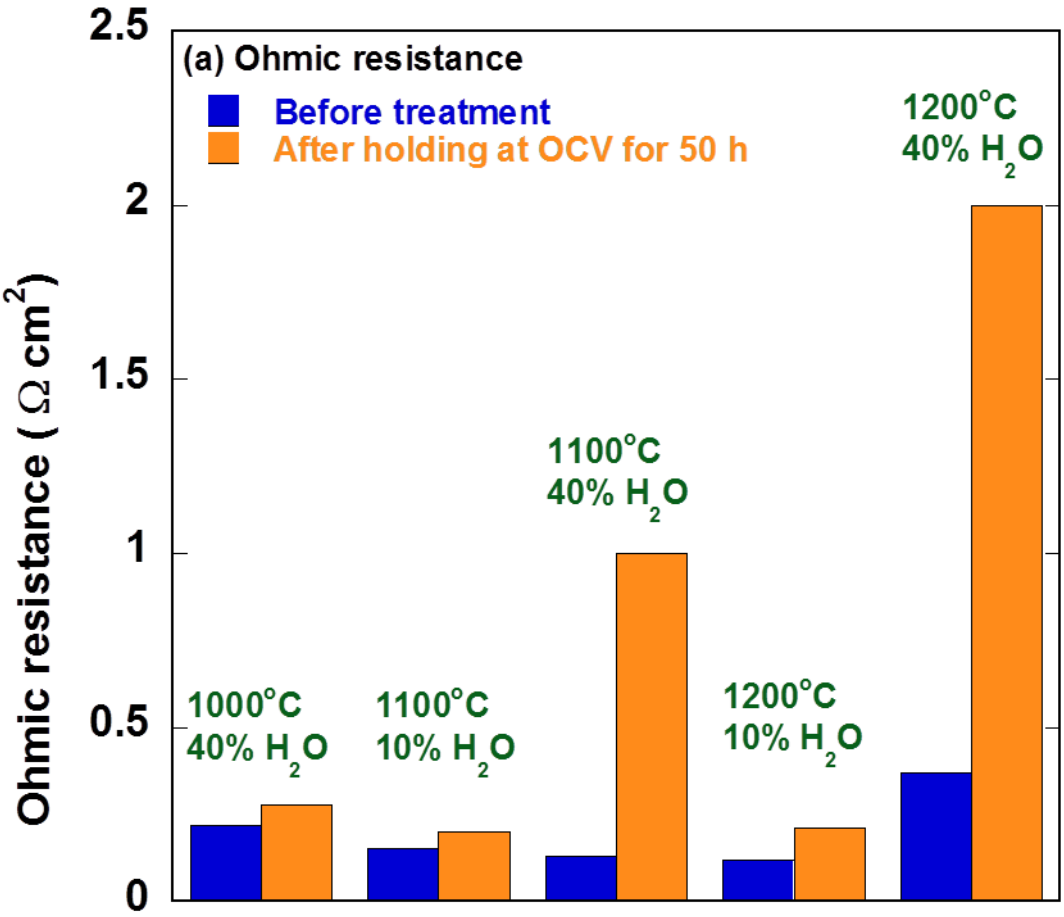


**Figure 5.2. (a) Ohmic resistances of anode before and after holding under the OCV for 50 h at 1000 ºC–1200 ºC with a supply of 10% $H_2O$– 90% $H_2$ and 40% $H_2O$– 60% $H_2$.**

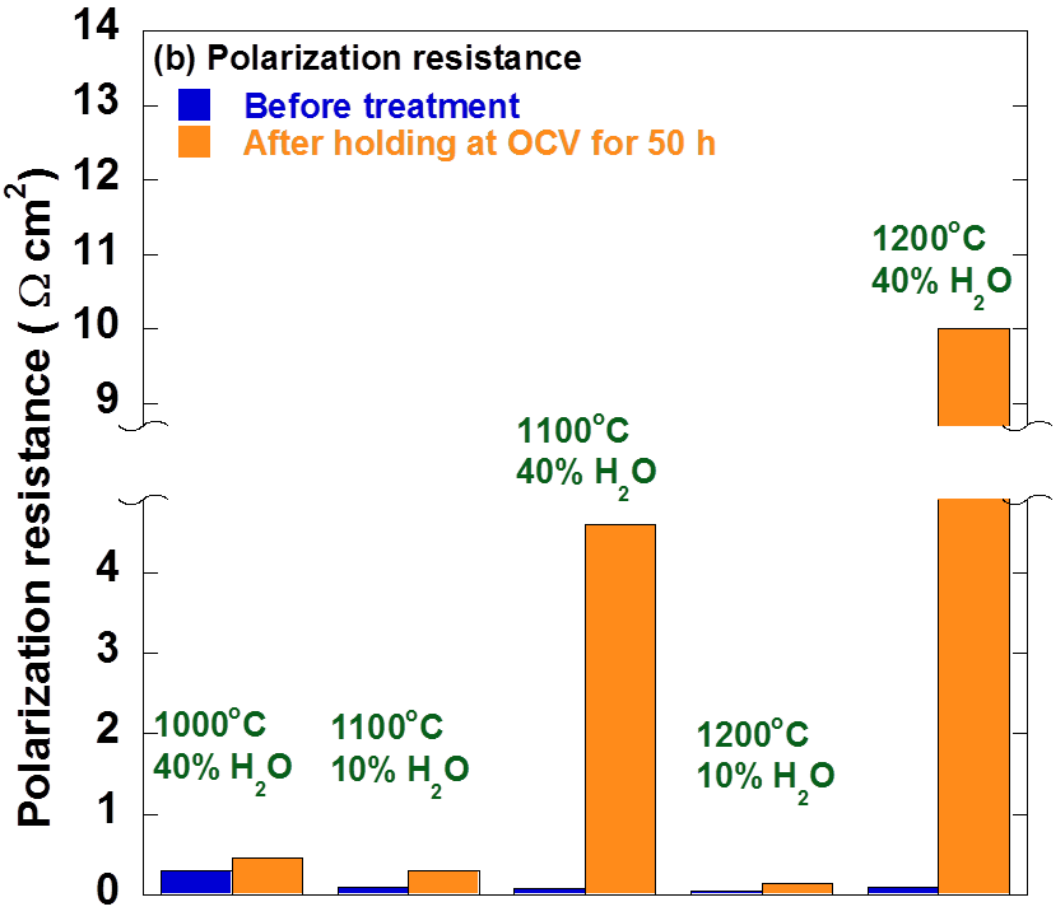


**Figure 5.2 (b) polarization resistances of anode before and after holding under the OCV for 50 h at 1000 ºC–1200 ºC with a supply of 10% $H_2O$–90% $H_2$ and 40% $H_2O$– 60% $H_2$.**

**.**

**Table 5.1.**
**Volume fraction evaluated from the reconstructed anode microstructures of Ni-YSZ.**

| | Phase | Initial* [20] | 1000 °C 40% $H_2O$ | 1100 °C 10% $H_2O$ | 1100 °C 40% $H_2O$ | 1200 °C 40% $H_2O$ |
|---|---|---|---|---|---|---|
| Volume Fraction % | Ni | 25.3 | 28.6 | 26.4 | 26.9 | 23.9 |
| | YSZ | 25.1 | 20.5 | 22.7 | 22.6 | 22.8 |
| | pore | 49.6 | 50.9 | 50.9 | 50.2 | 53.3 |

* The data sets of Ni–YSZ before heat-treatment was referred from Refs. 20.

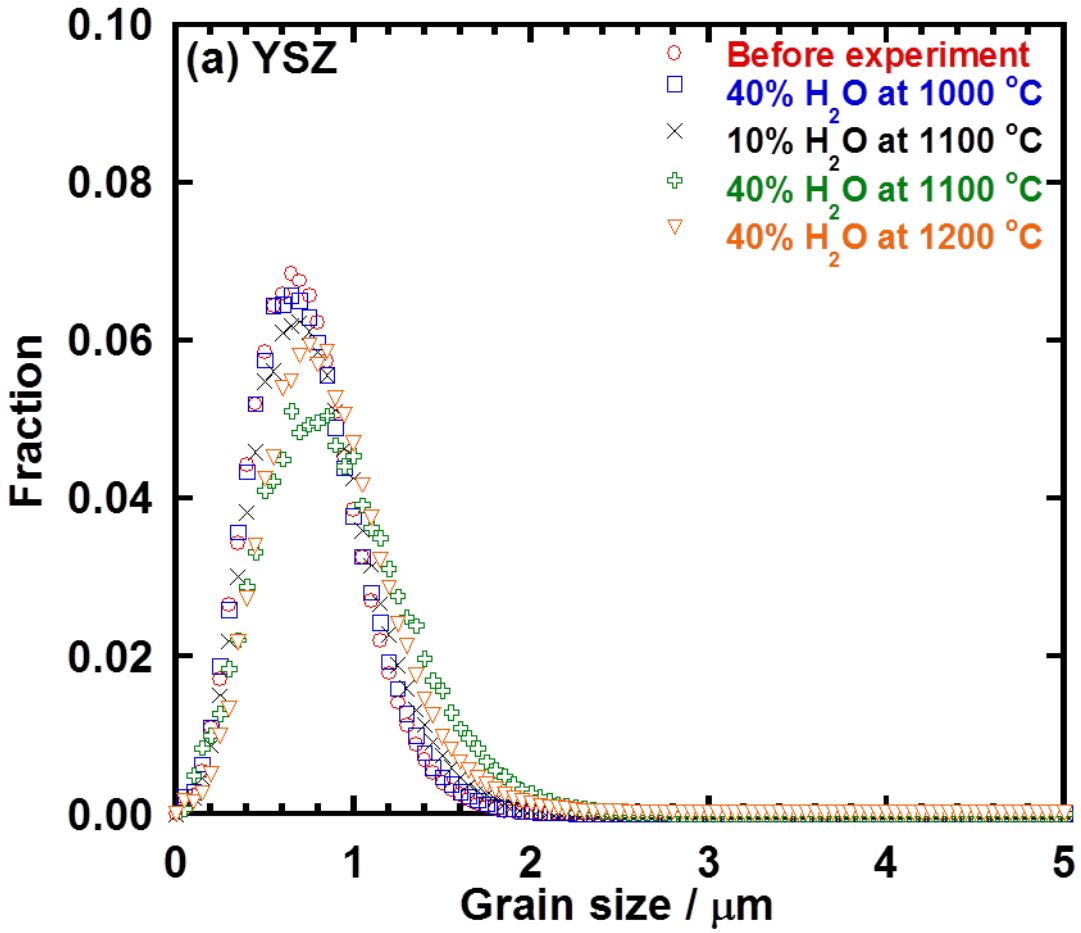


**Figure 5.3. Size distribution of (a) YSZ particles in the Ni-YSZ anode cermet before and after holding at OCV with a supply of 10% $H_2O$– 90 % $H_2$ and 40% $H_2O$– 60 % $H_2$ at 1000 ºC, 1100 ºC, and 1200 ºC for 50 h .**

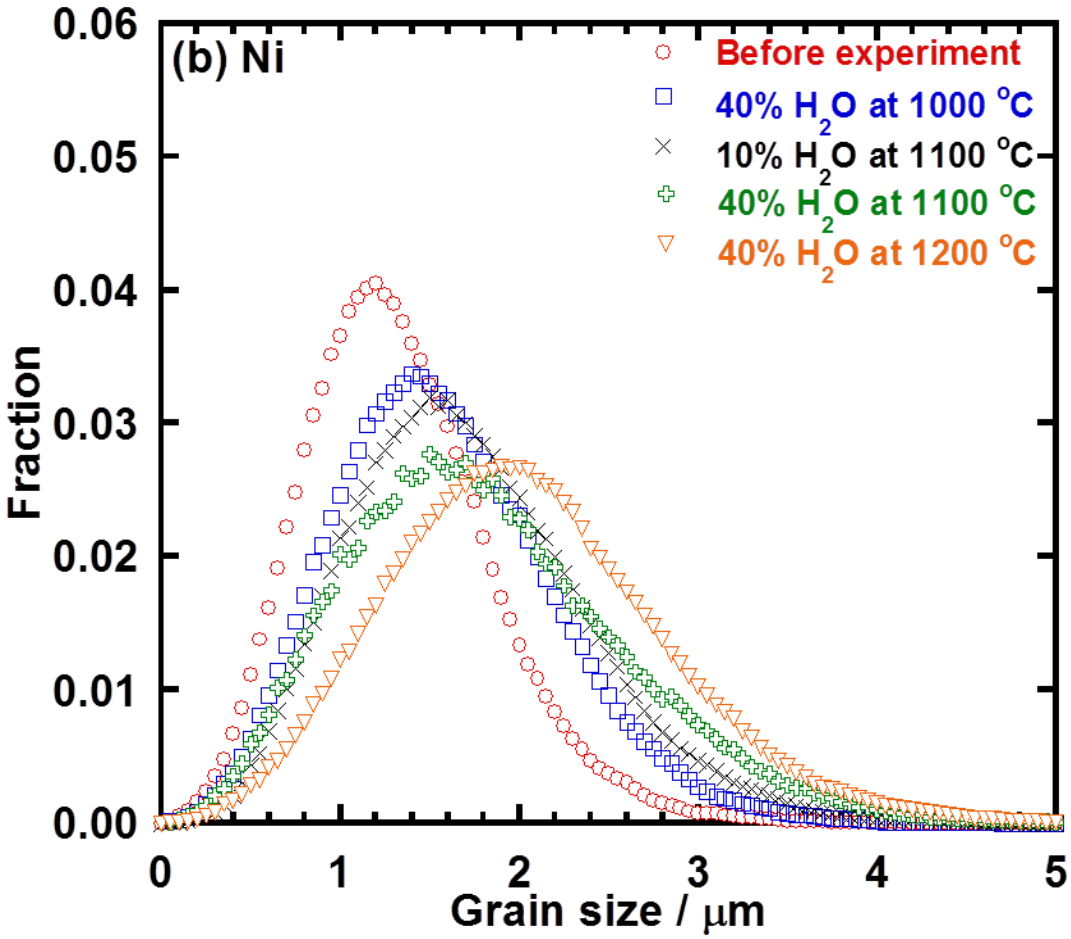


**Figure 5.3. Size distribution of (b) Ni particles in the Ni-YSZ anode cermet before and after holding at OCV with a supply of 10% $H_2O$– 90 % $H_2$ and 40% $H_2O$– 60 % $H_2$ at 1000 °C, 1100 °C, and 1200 °C for 50 h .**

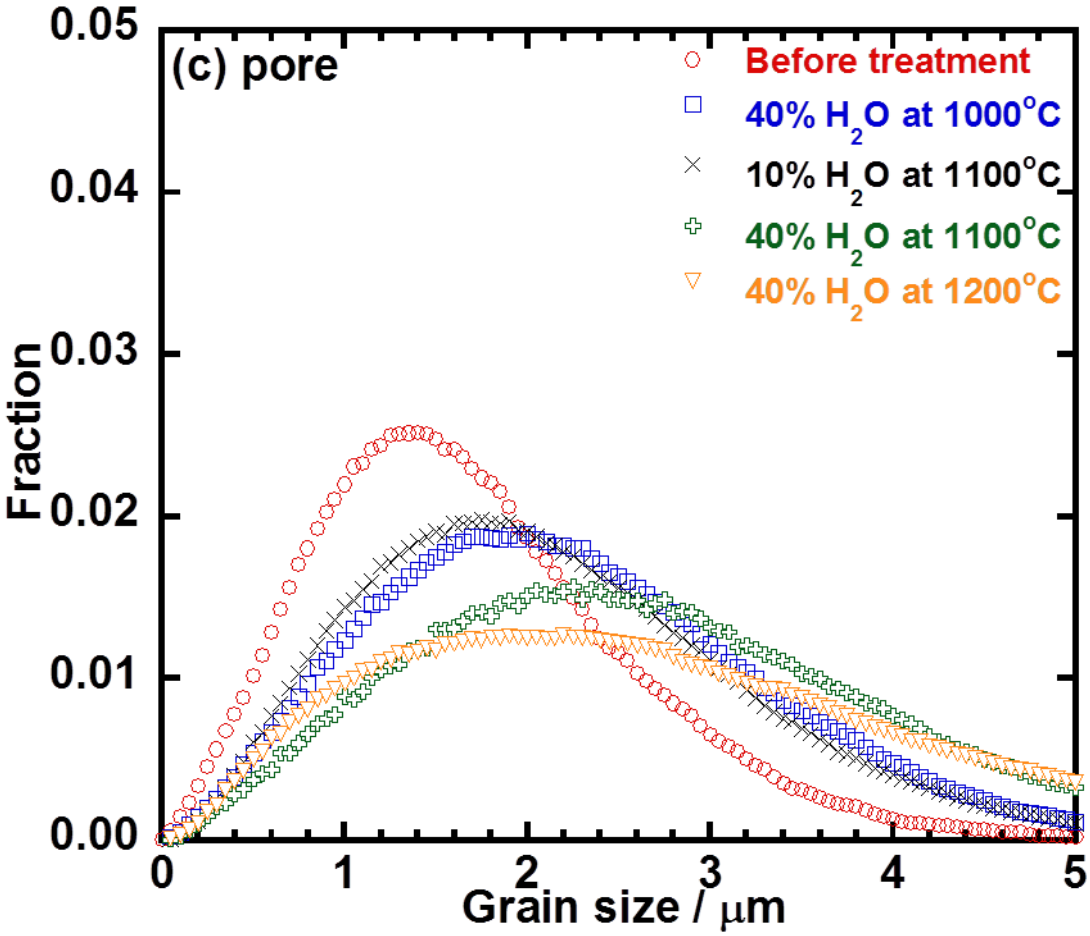


**Figure 5.3. Size distribution of (c) pore in the Ni-YSZ anode cermet before and after holding at OCV with a supply of 10% $H_2O$– 90 % $H_2$ and 40% $H_2O$– 60 % $H_2$ at 1000 ºC, 1100 ºC, and 1200 ºC for 50 h.**

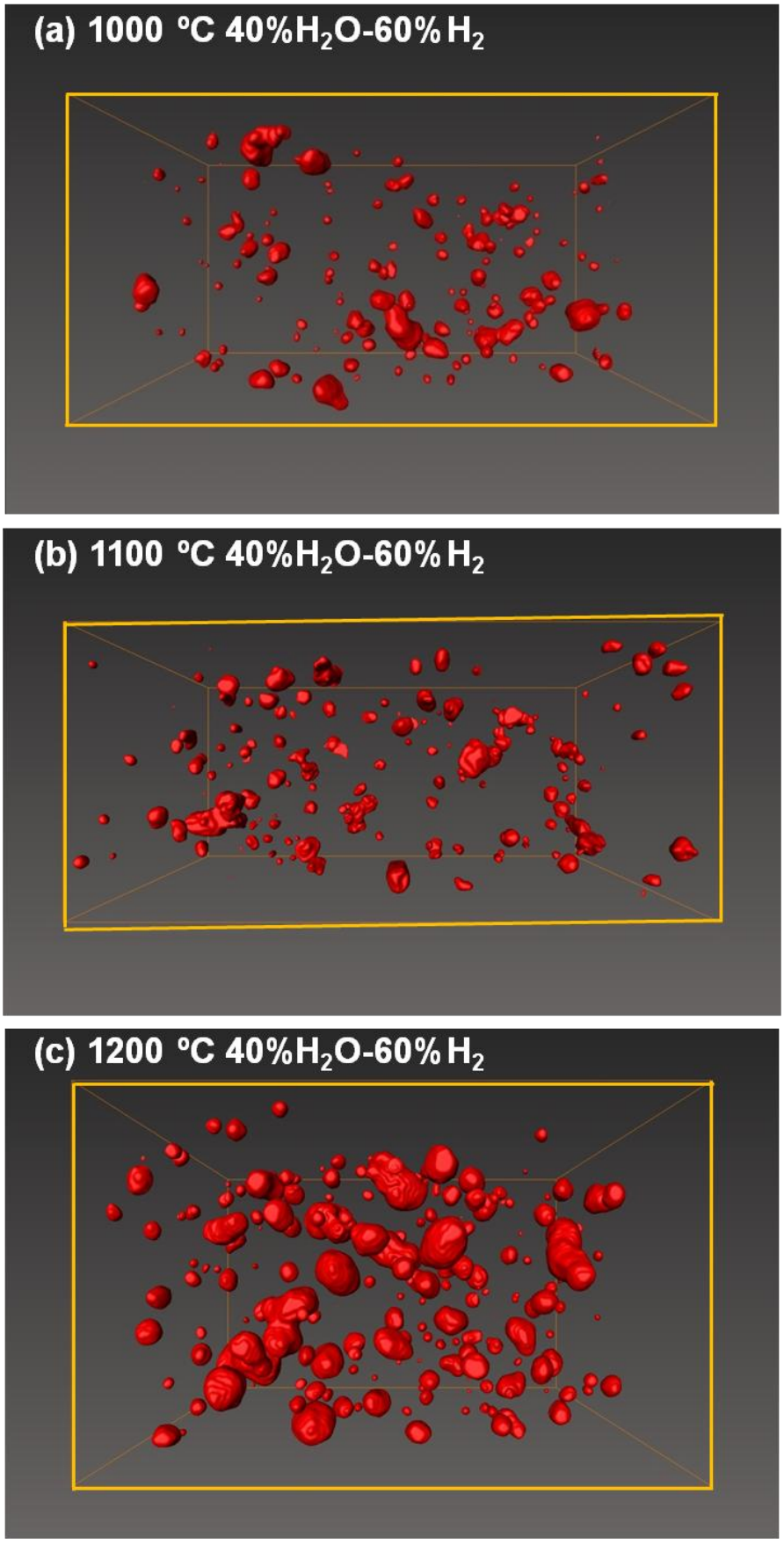


**Figure 5.4. 3D reconstructed isolated Ni phases for Ni–YSZ anode after flowing 40% $H_2O$– 60% $H_2$ for 50 h at (a) 1000 °C, (b) 1100 °C, and (c) 1200 °C.**

**Table 5.2. Sizes and isolated-Ni phase ratio of anode**

| | Direction | Initial*[20] | 1000 °C 40% $H_2O$ | 1100 °C 40% $H_2O$ | 1200 °C 40% $H_2O$ |
|---|---|---|---|---|---|
| Dimension / μm | *x* | 25.77 | 29.01 | 29.03 | 24.22 |
| | *y* | 9.38 | 12.01 | 14.04 | 15.30 |
| | *z* | 13.00 | 17.67 | 20.71 | 22.63 |
| Isolated-Ni phase ratio | | 3.80% | 3.98% | 6.60 % | 9.04% |

* The data sets of Ni–YSZ before heat-treatment was referred from Refs. 20.

**Table 5.3. Triple phase boundary (TPB) and active TPB for Ni-YSZ anode.**

| Ni-YSZ anode | Initial*[20] | 1000 °C 40% $H_2O$ | 1100 °C 10% $H_2O$ | 1100 °C 40% $H_2O$ | 1200 °C 40% $H_2O$ |
|---|---|---|---|---|---|
| Total TPB length (μm / $μm^3$) | 2.49 | 1.76 | 1.47 | 1.30 | 1.11 |
| Active TPB length (μm / $μm^3$) | 2.02 | 1.51 | 1.24 | 1.17 | 0.87 |

* The data sets of Ni–YSZ before heat-treatment was referred from Refs. 20.

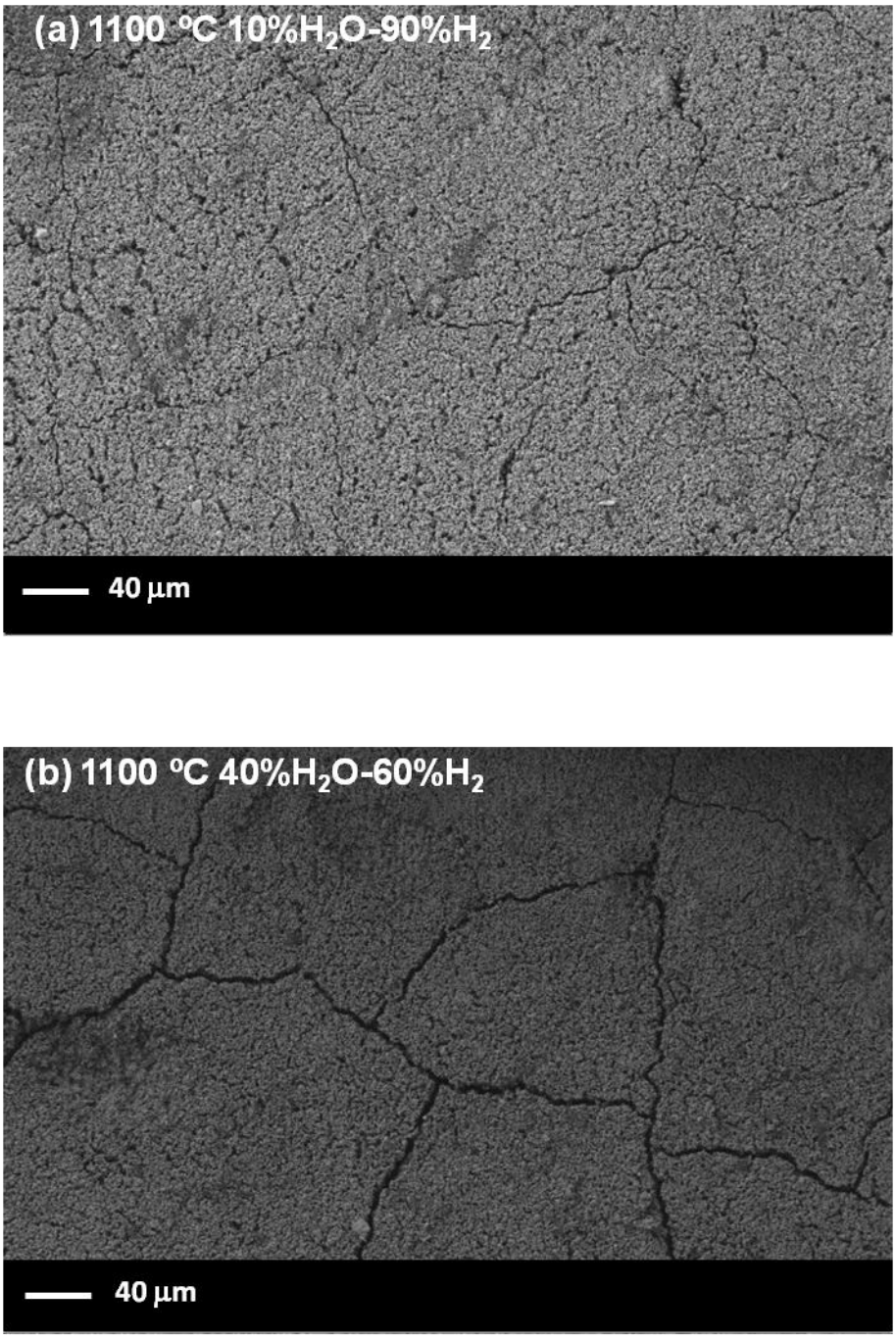


**Figure 5.5. Secondary electron images for Ni–YSZ surface after holding at OCV for 50 h with a supply of (a) 10% $H_2O$– 90% $H_2$ at 1100 °C, and (b) 40% $H_2O$– 60% $H_2$ at 1100 °C.**

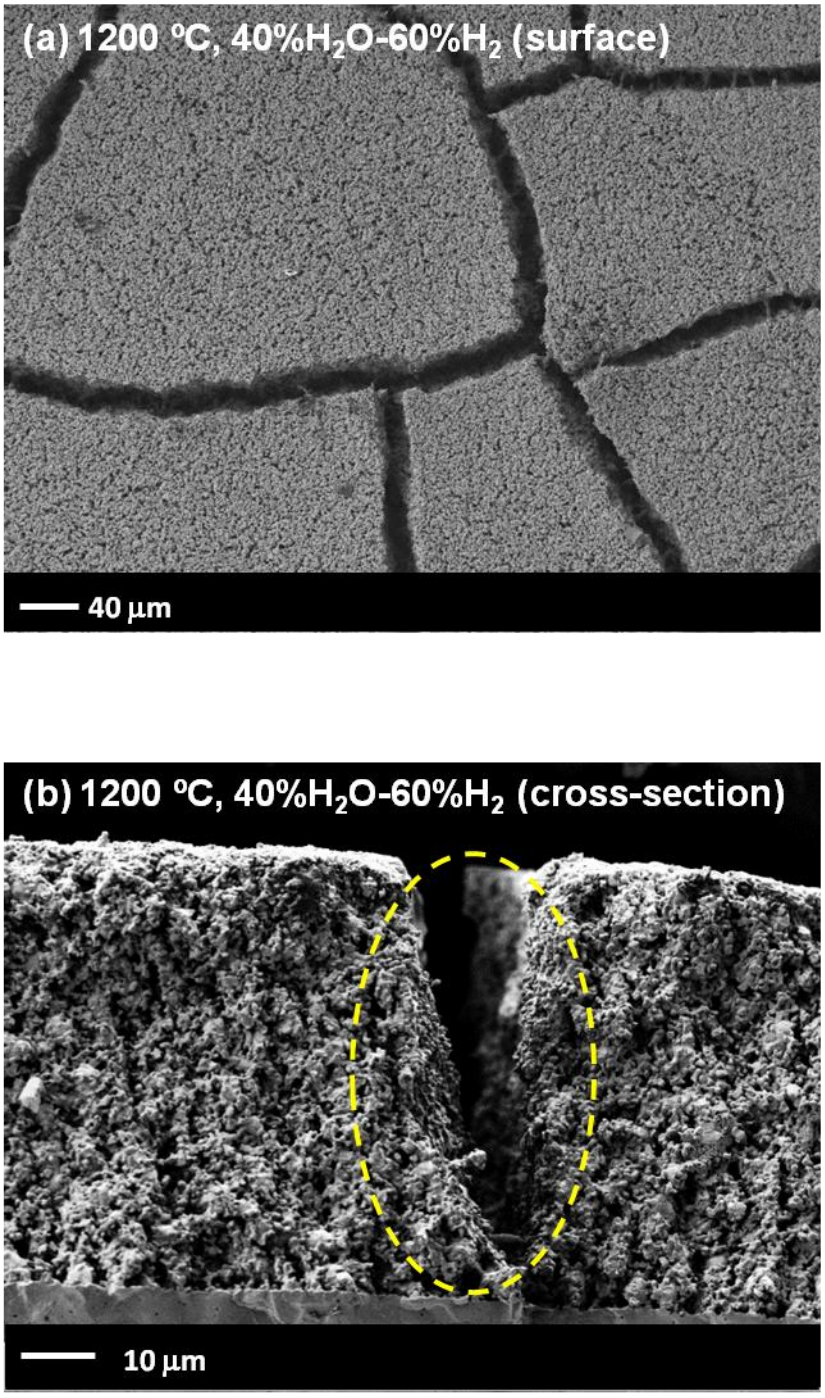


**Figure 5.6. Secondary electron images for Ni–YSZ (a) surface and (b) cross section after holding at OCV for 50 h with a supply of 40% $H_2O$–60% $H_2$ at 1200 °C.**

## General conclusions

In this thesis, the change in electrochemical performance of Ni-based anode was investigated with internal reforming of methane and supply of humidified hydrogen. The main part of the thesis is organized in five chapters associated with degradation of anode performance due to carbon deposition (chapter 1 to chapter 4) and Ni sintering (chapter 5).

In chapter 1, the influence of the anode thickness on the performance stability under a humidified methane (S/C = 0.1) at 1000 ºC was studied. The cell with Ni–SDC anode showed gradual improvement in performance during discharge regardless of anode thickness. These improvements upon discharge were related to the expansion of electrochemical active area as well as an increase in the electronic conductivity of SDC. The stable performance displyed in 30 μm-thick Ni–YSZ anode because the top surface of Ni–YSZ anode served as the buffer layer to suppress the damage in reaction sites near the anode/electrolyte interface and supported the effective removal of deposited carbon by the steam electrochemically-generated. However, the deterioration in performance was observed with 10 μm-thick Ni–YSZ anode within 18 h of discharge. For this anode, a large amount of carbon obstructed the pores in the whole anode layer. The carbonaceous species possess relatively low electric conductivity than that deposited in Ni–SDC. Accordingly, the cell performance was related to the deposited area and carbonaceous species, which was determined by the operating conditions and constituent materials.

In chapter 2, the cell performance and ac impedance of the Ni–YSZ and Ni–ScSZ anodes were evaluated in simulated gases with various ratios of $H_2$, CO, and $CO_2$. The

polarization resistance increased with a rise in CO concentration at low temperatures because of the difficulty of electrochemical oxidation of carbon monoxide. Carbon was deposited by the disproportionation of carbon monoxide in the $CO–CO_2$ mixture ($CO:CO_2$ = 95:5) at 750 ºC, which led to degraded performance. The durability for the Ni–YSZ and Ni–ScSZ anodes was also examined in comparison with internal steam and $CO_2$ reforming of methane. The amount of deposited carbon at 1000 ºC was larger than that at 850 ºC because the cracking of methane was facilitated at high temperatures. The descending order of degradation rate was Ni–YSZ ($CO_2$) > Ni–YSZ (steam) > Ni–ScSZ ($CO_2$) > Ni–ScSZ (steam) at 1000 ºC. Amorphous carbon was observed only on the Ni–YSZ anode, which was likely to cause deterioration by the decrease in nickel catalytic activity and the inhibition of gas diffusion. In contrast, the crystalline rod-shaped graphite was observed only on the Ni–ScSZ anode. The cell voltage and anodic overpotential were stable for the Ni–ScSZ anode.

In chapter 3, the cell performance and ac impedance for Ni–YSZ cermet were evaluated at 650 ºC and as a function of $H_2$/CO ratios in $H_2–CO–H_2O$ and $H_2–CO–CO_2$ mixtures, and the behavior of carbon deposition by carbon monoxide disproportionation and methane cracking was compared. The polarization resistance was enlarged with increasing CO concentration for the electrolyte-supported cells. This result suggests that electrochemical oxidation of carbon monoxide is more difficult than that of hydrogen at low temperatures. The polarization resistance in $H_2–CO–H_2O$ mixture was smaller than that in $H_2–CO–CO_2$ mixture because of the decrease in CO concentration by water gas shift reaction. While the polarization resistance was unchanged in $CO_2–CO$ mixture for the anode-supported cells, the resistance increased in $H_2O–CH_4$ mixture for both of the cells in the carbon deposition condition. The graphite was deposited as coated layer on

the nickel particles only near the anode surface facing to the flowing gas after durability test in $CO_2$–CO mixture for the anode-supported cells. On the other hand, a large amount of agglomerated amorphous carbon was deposited from the anode surface to the interface between the anode and the electrolyte after power generation in $H_2O$–$CH_4$ mixture. These results suggest that the rate of methane cracking at 800 ºC was slower than that of CO disproportionation at 650 ºC. It was concluded that the increase in polarization resistance was strongly correlated with the carbon deposition near the anode/electrolyte interface.

In chapter 4, it was attempted to remove carbon from the anode by two methods. Carbon was removed homogenously in the whole Ni–YSZ anode layer by flowing $H_2$, $H_2O$, and $CO_2$. The other method was supplying $O^{2-}$ to anode via current passage. In this case, carbon near the anode/electrolyte interface was removed preferentially. The ease of carbon removal in different atmospheres as followed the order: $O^{2-}$ > $H_2O$ > $CO_2$ > $H_2$. However, Ni in the anode cermet tended to be oxidized by $H_2O$ and $CO_2$, which gave rise to the performance degradation of the anode. On the other hand, in the 10% $H_2$–5% $H_2O$ atmosphere ($P(O_2) < 10^{-13}$ atm), carbon could be removed without the significant performance degradation. In the case of carbon removal through electrochemical reaction, carbon could be removed the most effectively without appreciable performance degradation.

In chapter 5, the Ni–YSZ anodes was held at OCV with supply of humidified hydrogen at 1000 ºC, 1100 ºC, and 1200 ºC, and microstructural change was quantitatively evaluated by FIB–SEM analysis. It was clarified that the growth of Ni particles was accelerated with increasing temperature and humidity. However, the increasing in isolated-Ni phase and reducing of active TPB length were relatively small

considering, the severe degradation of anode performance at high temperature and humidity. It was observed that the Ni–YSZ anode separated into several island-like parts under 40% $H_2O$ atmosphere at 1200 ºC. Consequently, the ionic and electronic conductions in the in-plane direction of anode layer were restricted. This should be dominantly responsible for the degradation of anode performance.

Finally, the author hopes this thesis contributes to the advances in the development of anode for solid oxide fuel cells.

## Publication list

**Chapter 1**

**Influence of Ni–oxide Anode Thickness on Performance Stability in Internal Steam Reforming of Methane for Solid Oxide Fuel Cells**

Yi-Hsuan Lee, Hirofumi Sumi, Hiroki Muroyama, Toshiaki Matsui, and Koichi Eguchi

Journal of the Electrochemical Society, 160 (6), F1-F6 (2013).

**Chapter 2**

**Comparison between Internal Steam and $CO_2$ Reforming of Methane for Ni–YSZ and Ni–ScSZ anodes of Solid Oxide Fuel Cells**

Hirofumi Sumi, Yi-Hsuan Lee, Hiroki Muroyama, Toshiaki Matsui, and Koichi Eguchi

Journal of the Electrochemical Society, 157 (8), B1118-B1125 (2010).

**Chapter 3**

**Effect of Carbon Deposition by Carbon Monoxide Disproportionation on Electrochemical Characteristics at Low Temperature Operation for Solid Oxide Fuel Cells**

Hirofumi Sumi, Yi-Hsuan Lee, Hiroki Muroyama, Toshiaki Matsui, and Koichi Eguchi

Journal of Power Sources, 196, 4451-4457 (2011).

**Chapter 4**

**Influence of Carbon Deposition and Removal on Performance of Ni–YSZ Anode in Internal Methane Steam Reforming for Solid Oxide Fuel Cells**

Yi-Hsuan Lee, Hiroki Muroyama, Toshiaki Matsui, and Koichi Eguchi

Journal of Power Sources, to be submitted.

**Chapter 5**

**Degradation Induced by Sintering of Ni–YSZ Anode in Solid Oxide Fuel Cells**

Yi-Hsuan Lee, Hiroki Muroyama, Toshiaki Matsui, and Koichi Eguchi

Journal of Power Sources, to be submitted.

## Acknowledgments

This thesis is a summary of author's studies during 2008-2013 at Department of Energy and Hydrocarbon Chemistry, Graduate School of Engineering, Kyoto University.

The author greatly appreciates *Professor Koichi Eguchi*, Department of Energy and Hydrocarbon Chemistry, Graduate School of Engineering, Kyoto University, for excellent guidance and precious suggestions throughout this work. The author would like to express his gratitude to *Professor Takeshi Abe* and *Professor Ryu Abe*, Department of Energy and Hydrocarbon Chemistry, Graduate School of Engineering, Kyoto University, for their fruitful discussion and hopeful comments.

The author is indebted to *Associate Professor Toshiaki Matsui* and *Assistant Professor Hiroki Muroyama*, Department of Energy and Hydrocarbon Chemistry, Graduate School of Engineering, Kyoto University, for valuable remarks and precise guidance.

The author would like to state his gratitude to *Dr. Hirofumi Sumi*, Advanced Manufacturing Research Institute National Institute of Advanced Industrial Science and Technology, and *Dr. Jun Yang*, Department of Energy and Hydrocarbon Chemistry, Graduate School of Engineering, Kyoto University, for constructive suggestions and hearty encouragements. The author thanks to all the members of Professor Eguchi's laboratory for their devoted contributions to this work.

Finally, the author wishes to thank his parents, sister, and friends for their understanding and continuous supports.

*Yi-Hsuan Lee*